UNIVERSITÀ DEGLI STUDI DI PADOVA

DIPARTIMENTO DI INGENGERIA INDUSTRIALE

SCUOLA DI DOTTORATO DI RICERCA IN INGEGNERIA INDUSTRIALE

INDIRIZZO INGEGNERIA CHIMICA DEI MATERIALI E DELLA PRODUZIONE

CICLO XXVII

ADVANCED CELLULAR CERAMICS PROCESSED USING DIRECT FOAMING METHODS

Direttore della Scuola : Ch.mo Prof. Paolo Colombo

Coordinatore d'indirizzo: Ch.mo Prof. Enrico Savio

Supervisore :Ch.mo Prof. Paolo Colombo

Dottorando : Elisangela Guzi de Moraes

To my daughter Ana Carolina

ACKNOWLEDGEMENTS

In first place, I would like to express my deepest gratitude to Prof. Paolo Colombo, my supervisor, for the opportunity of developing this work and for his constant support and endless positive and encouraging attitude, for the extremely constructive and motivating scientific discussions, and most important for the freedom of following own ideas. This work would not have been possible without him.

A sincere and special thanks to Lisa Biasetto, Mauro, Inès, Carlo Dengo, Prof. Enrico Bernardo, Mauro Gobbin, Sirio e Roberta for the extremely valuable help during these 3 years at UNIPD. Also, I would like to thank Caterina Ciscato and all her group at "Polo bibliotecario di Ingegneria".

I would like to thank all the colleagues, specially Laura Brigo, Erika e Michela, for the good working atmosphere, receptiveness, and the support when needed; was as a great experience for me to know and learn with all of them.

I express my gratitude for the chance and financial support of the Marie Curie ITN 7th Framework Programme, FUNEA. I greatly owe my professional and personal growth to this opportunity. Also, I would like to express my sincere appreciation and thanks for all FUNEA's friends who have shared good times and help me out in all time, specially Duan Li, Van Lam, Monika, Wenjie and Cristina.

Last but not least, I would like to thank my family, specially my husband and daughter, for their constant love, support and help not only during the time of this thesis, but during all my live.

ABSTRACT

The research work presented in this thesis concerns the development of silicon nitride based ceramics with a cellular structure and containing designed interconnected porosity (> 80 vol%) and cell size distribution (10 up to 800 μm) by direct foaming processing routes. Concentrated emulsions (O/W oil-in-water) stabilized by surfactants and gelcasting using environmentally friendly biopolymers as gelling agents, were developed as intermediates in the production of highly porous inorganic materials. Differently from conventional direct foaming methods the evaporation (and expansion) of the alkane droplets affords the foaming during drying of emulsions.

Sintering is a critical step in the case of silicon nitride, since high temperatures and increased dwelling time are necessary for sufficient densification to occur, due to a low diffusion in the solid state. In order to overcome this difficulty, we report in this thesis two different strategies by liquid phase sintering with sintering additives:

1) Conventional sintering at 1600 °C and 1700 °C, using N_2 flow in order to suppress the dissociation reactions and permit sintering with little weight loss.

2) Sintering by intense thermal radiation, inside a modified SPS set-up, shows to be effective in promote densification of the foam struts and develop of SiC nanowires (increase the fracture toughness of Si_3N_4 foams) on the cell walls and struts at short times and lower sintering temperatures.

Further, the influence of the sintering additives, Y_2O_3 and MgO, and the effect of the sintering temperature on the formation of rod-like β–Si_3N_4 grains were also investigated.

Highly porous Si_3N_4 ceramics are promising candidate for various engineering applications such as: gas filtering application (high temperature and harsh environment), heat insulators, catalyst carriers, bioreactors, medical implants, since recent results confirmed the non-cytotoxicity and biocompatibility, owing to remarkable properties as high strength, high stiffness, good toughness, high temperature resistance, high corrosion resistance, good wear resistance and high permeability.

During the present research work, the characterization of highly interconnected Si_3N_4 foams in terms of microstructure (cell size distribution and porosity), mechanical properties and permeability was performed.

High compressive strengths (up to 33 MPa) were reported with the increasing of sintering temperature up to 1700 °C (conventional sintering), owing to the development of elongated β–grains, as well a strong packing of particles on cell walls and struts.

Permeability evaluation shows that Si_3N_4 foams are in the range of gelcasting foams (on permeability map) and are suitable for filtering application.

The successful combination of colloidal processing, foaming and fast consolidation of foams, and also pressureless sintering at relatively low temperatures applied to produce cellular ceramics based on Si_3N_4 was also extended to other advanced materials e.g. max-phases belonging to Ti-Al-C system.

RIASSUNTO

Materiali ceramici a base di Si_3N_4 altamente porosi sono potenziali candidati per varie applicazioni di ingegneria: filtraggio di gas ad alta temperature ed in condizioni critiche, isoltaori termici, trasporto di catalizzatori, bioreattori e impianti biomedici (recenti risultati di letteratura hanno confermato la non citotossicità e la biocompatibilità del Si_3N_4).

L'attività di ricerca della presente tesi riguarda lo sviluppo di materiali ceramici a base di nitruro di silicio caratterizzati da una struttura cellulare, contenenti porosità interconnessa (> 80 vol%) e celle con una distribuzione dimensionale che varia dai 10 μm fino agli 800 μm. La tecnica utilizzata per la produzione dei materiali ceramici cellulari consiste nella schiumatura diretta; sono state sviluppate emulsioni concentrate (O/W olio-in-acqua) stabilizzate da tensioattivi e gelcasting di biopolimeri ecocompatibili, come step intermedi nella produzione di materiali inorganici altamente porosi. Diversamente dai tradizionali metodi di schiumatura diretta, la schiumatura è fornita dall' evaporazione (ed espansione) delle gocce di alcani durante l'essiccazione delle emulsioni. Mentre nel caso di gelcasting, la capacità dei tensioattivi schiumogeni combinata con la gelificazione termica fornisce la schiumattura.

Nel caso della produzione di componenti a base di nitruro di silicio la sinterizzazione rappresenta un punto critico, poiché sono necessarie temperature elevate e prolungato tempo di mantenimento alla T di sinterizzazione al fine di garantire sufficiente densificazione a causa delle basse velocità di diffusione allo stato solido. Al fine di superare queste difficoltà, nella presente tesi sono state sviluppate due strategie:

1) Sinterizzazione convenzionale a 1600 °C e 1700 °C in flusso di N_2, al fine di inibire le reazioni di dissociazione e sinterizzare con basse perdite di peso.

2) Sinterizzazione con intensa radiazione termica, attraverso la tecnica dello Spark Plasma Sintering (SPS), la quale si è dimostrata efficace al fine di densificare gli struts della schiuma e sviluppare nanofili di SiC sulle pareti di cella e sugli struts, a temperature più basse e per tempi più brevi rispetto alla sinterizzazione convenzionale. Nanofili di SiC contribuiscono ad aumentare la resistenza alla frattura delle schiume.

Inoltre, l'influenza di addittivi di sinterizzazione, Y_2O_3 e MgO, sulla temperatura di sinterizzazione e sulla formazione di β–Si_3N_4 grains, sono stati investigati.

Le strutture cellulari a base di Si_3N_4 prodotte con le tecniche sopra descritte sono state caratterizzate in termini di microstruttura (distribuzione della dimensione di celle e porosità), proprietà meccaniche (test di compressione) e permeabilità ai gas.

Porosità totale che varia dai ~74 fino agli 89 vol%, e le dimensioni delle celle variano in un ampio range ~20 fino agli 850 μm, in funzione della velocità di emulsione, tipici di biopolimeri.

E' stato trovato che le schiume sinterizzate a 1700 °C (sinterizzazione convenzionale) sono caratterizzate da elevati valori di resistenza a compressione up to 33MPa per effetto dello sviluppo di grani allungati di fase β–Si_3N_4 e per effetto della notevole densificazione delle particelle in corrispondenza delle pareti di cella e degli struts.

Le misure di permeabilità hanno dato valori di costanti di permeabilità nel range delle schiume ottenute con la tecnica del gelcasting e sono pertanto utili per applicazioni di filtraggio.

La combinazione di processi colloidali, schiumatura, rapida consolidazione delle schiume e sinterizzazione in assenza di pressione a temperature moderate applicate ai ceramici porosi a base di Si_3N_4, sono state applicate anche ad altri sistemi come ad esempio al sistema Ti-Al-C (Max-Phases).

TABLE OF CONTENTS

Part I

INTRODUCTION

I INTRODUCTION

Ceramics with a cellular structure and containing designed interconnected porosity above 60 vol% find applications particularly where the transport of fluids is required, e.g. molten metal and exhaust particulate filters at high temperature, gas-burner systems, catalyst support, and in energy-related industries [1–6]. Cellular ceramics are materials tailored to possess exceptional combination of properties such as lightweight, high temperature stability and permeability to fluids among other special functionalities that cannot normally be reached by conventional dense counterparts [7,8].

High technological applications take advantage of specific features exhibit by ceramics but with improved performance by the replacement of solid material by voids in the component, for instance, low thermal conductivity, high surface area, high specific strength, and low dielectric constant [2].

Silicon nitride (Si_3N_4) is one of the most widely used ceramics in many engineering applications due to its outstanding thermo-mechanical properties, such as flexural strength and Young's modulus around 900 MPa and 310 GPa, respectively, fracture toughness between 3 to 12 $MPa \cdot m^{1/2}$ [9], and strain-to-failure around 3×10^{-3} [10,11]. Its excellent thermal properties, such as, high strength at temperatures above 1000 °C [12], thermal shock resistance can be attributed to the combination of a low thermal expansion coefficient, medium elastic constants, and moderate thermal conductivity [9,13,14], combined with the low density of Si_3N_4 (3.2 $g \cdot cm^{-3}$) and consists an important advantage.

Highly porous Si_3N_4-based ceramics are promising candidate for engineering applications, such as hot gas filter, heat insulators, catalyst carriers, bioreactors, medical implants, since recent results confirmed the non-cytotoxicity and biocompatibility [15]. Remarkable properties as high strength, high stiffness, good toughness, high temperature resistance, high corrosion resistance, and good wear resistance, special thermal properties, and high permeability [16].

However, the high cost of production (sintering is generally assisted by pressure), due to the highly covalent bonding between silicon and nitrogen atoms and very slow solid-state diffusion [17], limits significantly the use of silicon nitride-based ceramics. The additions of sintering additives, which are usually metal oxides that form a low-melting-point eutectic liquid with the oxide surface layers of the silicon nitride powder, improve sintering activity considerably and promote high densities without the use of pressure during sintering [18,19].

Various processing methods for the production of highly porous Si_3N_4, such as partial sintering [20,21], reaction sintering [12,22], the use of sacrificial templates using starch

consolidation [23], direct foaming [24], gelcasting [25] and preceramic polymers [26], have been proposed. But they fail on the development of interconnected structures with high level of open porosity (≥75%).

In order to develop more economical processes for the production of porous silicon nitride with proper process control increasing reliability and uniformity in the properties of final component, the objective of the current work is concerned with the fabrication of silicon nitride foams with tailored microstructure in terms of porosity (> 80vol%) and cell size distribution ranging from (10 to 500 μm) using direct foaming processing routes, such as emulsification and gelcasting using environmentally friendly biopolymers as gelling agents by cost-effective pressureless sintering envisaging gas filtering application (High temperature and harsh environment). Additionally, the characterization of Si_3N_4 foams in terms of microstructure (cell size distribution and porosity), mechanical properties and permeability was performed. Further, the influence of the sintering additives, Y_2O_3 and MgO, and the effect of the temperature on the formation of rod-like β–grains were also investigated.

In the light of these achievements, the foaming strategies were extended to other advanced ceramic materials, as ternary Ti-Al-C max phases.

1.1 Cellular Ceramics

Cellular ceramics are materials tailored to possess exceptional combination of properties as high porosity and lightweight, as well special functional properties, such as low thermal conductivity, high-temperature stability, excellent thermal shock resistance, and low dielectric constant, good resistance against crack propagation, high permeability and high surface area. These materials are used for a wide range of technological applications, such as filters, membranes, catalytic substrate, thermal insulation, gas burner media, and refractory materials [1,2,8].

The structure of cellular ceramics consists of polyhedral cells that are arranged three-dimensionally to efficiently fill the space and depending on the overall morphology a structure typical of a honeycomb (possessing parallel prismatic cells) or of a foam (for which cell walls are randomly oriented in space) can be identified. The porosity in these materials usually exceeds 70% of the total volume. These materials may have a potential in structural applications owing to their design allows for the efficient optimization of important engineering characteristics, such as high-modulus-to-weight ratio. In addition, they offer durability in severe environments coupled with

surface or bulk characteristics that permit them to satisfy specific functional purposes, for instance filtration at high temperature [6,8].

Cellular ceramics are divided in two classes: open cell or interconnected and closed cells. As highlighted by Colombo and Bernardo, the current terminology developed by IUPAC to classify the porosity of materials, which classified the pores sizes into three different dimensional ranges: micropores (< 2nm), mesopores (2-50 nm), and macropores (> 50 nm), is not useful to describe or characterize the porosity of cellular materials [27].

The terms macrocellular and microcellular (cell with a size smaller than 30 to 50 μm) are more accurate to differentiate the structure of the foams, as for example cells and windows. Furthermore, is important also consider the composition and the processing conditions that will define the overall properties of the component. For example, microporosity (often present in the ceramic struts and cell walls), composition of the grain boundaries and the amount, size and morphology of the defects need also to be taken into account, once they can influence mechanical reliability, for example [27].

Cellular ceramics can be produced with a variety of microstructures with controlled properties through several versatile and simple methods (see Figure 1.1), such as replica, sacrificial template, and direct foaming techniques, and recent reviews are available on this subject [2,6,28].

The replica technique, Figure 1.1 a), is the most widespread processing approach for open-cell ceramic foams, so-called reticulated ceramics, and consists on the impregnation of porous or a cellular structure (generally PU sponge) with a ceramic suspension or precursor solution in order to produce a macroporous ceramic exhibiting the same morphology as the original porous material, but with a particularity, the cell struts are hollow after pyrolysis, affecting their mechanical strength. Alternatively, recoating the reticulated ceramic with slurry can reduce the number of defects inside the struts increasing their reliability [2,6,8].

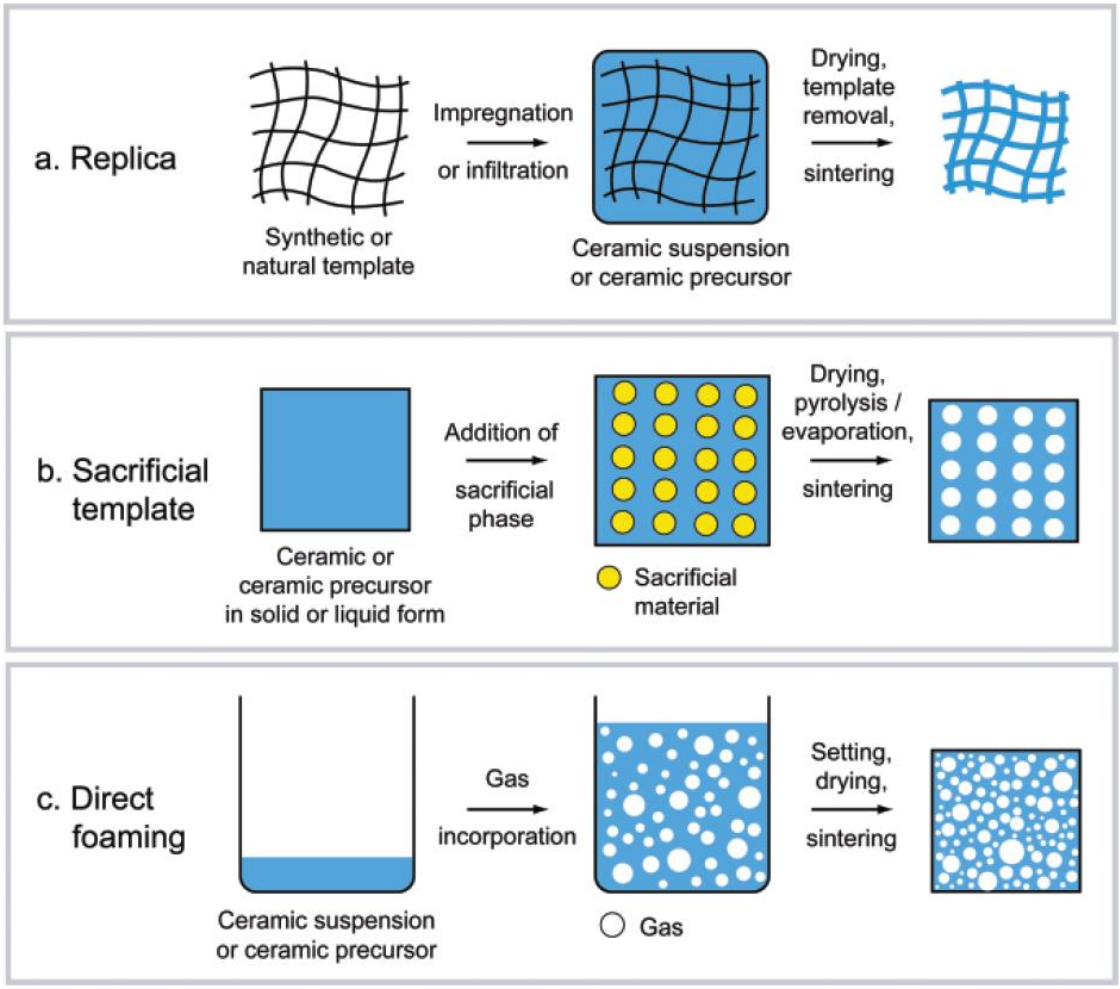

Fig 1.1. Scheme of the fundamental processing routes for the production of cellular ceramics [2].

The sacrificial template technique (Figure 1.1 b) consists in the incorporation of a sacrificial phase that is homogeneously distributed throughout the ceramic matrix. Afterwards, a heating treatment is performed and hollow cells are produced when the solid material that occupies the space within the volume of the component disappears [2,6].

Direct foaming (Figure 1.1 c) consists in the incorporation of gas (bubbles) inside a liquid slurry containing ceramic powders (or ceramic precursor solution) to create a foam by mechanical stirring, by bubbling a gas through the liquid, or by the in situ generation of gas within the liquid. Subsequently, the liquid foam is stabilised in order to preserve its porous morphology [2,6,8].

The aim of this work is the development of advanced cellular ceramics based on Si_3N_4 using direct foaming processing route for the fabrication of tailored microstructure in terms of cell size

distribution and porosity, mechanical properties and permeability. In the follow section the direct foaming method is described in more detail.

1.2 Direct foaming process

In direct foaming techniques, ceramic foams are produced by incorporating air into a suspension by mechanical frothing (mixing or agitation to introduce air bubbles), by the evolution of a dissolved gas, by bubbling a gas through the liquid, or by the in situ generation of gas within the liquid. In the final case, the gas-evolution process is usually initiated by heat or by a chemical reaction [6,8].

The total porosity of liquid foams is proportional to the amount of gas incorporated into the ceramics suspension during foaming process; while pore size is determined by the stability of the liquid foam before setting takes place [2]. Gas bubbles initially nucleate as spheres and then grow as polyhedral cells, Figure 1.2 [29]. The foam morphology (bubble size and shape) depends on concurrent processes controlling the development and stability of liquid foams, such as, drainage (the liquid will drain through the cell edges until an equilibrium state is reached); coarsening (gas diffuses between bubbles, allowing some to grow while others shrink and disappear, leading to an increased dispersion of cell sizes), and film rupture when a film (cell wall) becomes too thin and weak leading finally to collapse of liquid foam [6,8]. These destabilization processes takes place in order to reduce the total Gibbs free energy, resulting in large pores in the final cellular microstructure [2,28].

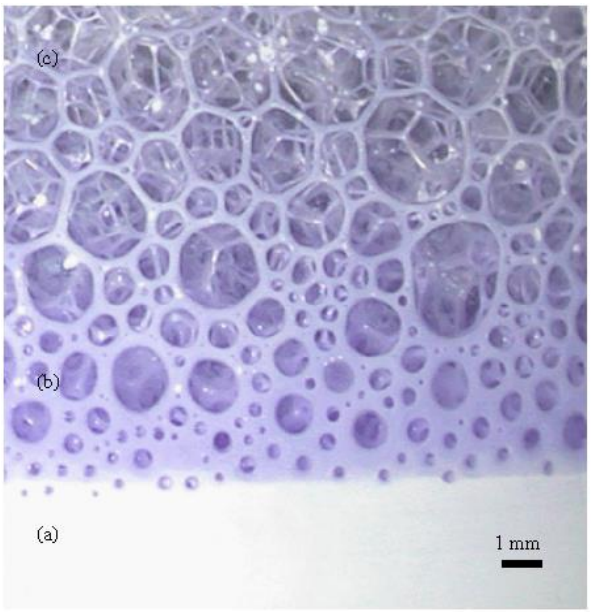

Fig 1.2. Three stages of foaming process of emulsified ceramic powder suspension [29].

In order to prevent the foam collapse, special additives as long-chain amphiphilic molecules and biomolecules as lipids and proteins can be used as surface-active agents to stabilize liquid foams by adsorbing at the air bubble surface reducing the interfacial energy of the gas-liquid boundaries [2,28]. Since it is stabilized, another strategy to keep the liquid foam morphology is setting it by means of gelling or cross-linking of organic compounds.

Direct foaming methods offer some advantages with respect to other processing routes because they permit obtain foams with open or closed cells within a broad range of cell sizes and bulk densities, possessing dense struts containing fewer defects, and with tailored permeability and flow path tortuosity. The choice of suitable surfactants or proteins, that control surface tension provides a further degree of control of the foam structure. The ceramic foams obtained by direct foaming are sintered by conventional means with an initial slow pyrolysis step for carefully eliminating the organic setting agents [6].

In this thesis, a novel processing route developed by Barg et al. [29], which consists in emulsifying a homogeneously dispersed high-alkane phase in a stabilized ceramic suspension was used. In contrast to the conventional direct foaming methods, foaming is driven by the autonomous evaporation of the alkane phase, and the emulsified suspensions are consolidated by the expansion of the alkane droplets and drying of the aqueous medium, leading to a time dependent expansion of the emerging foam in a mould [28,29,30].

Suspensions, emulsions and foams are intermediates in the production of porous inorganic materials of high technological interest. While the inorganic particles in the suspensions act as fillers and define the crystallographic structure, droplets and bubbles are intermediates for the porosity formation in the resulting inorganic foams.

Thus, it is of great importance for this study to give a background on the main factors influencing stability and formation of surfactant stabilized emulsions and gelcasting foams as well as colloidal suspensions.

1.2.1 Emulsions

Emulsions are metastable colloidal dispersions in which two immiscible fluids such as oil (hydrocarbon) and water, with one being dispersed into the other by shearing in presence of surface-active agents, which leads to the fragmentation of one phase into the other [31,32]. The dispersed phase is sometimes referred to as the internal phase and the continuous phase as the external phase. Three important aspects are essential for the classification of emulsions: the type of dispersed phase, droplets size and the volume fraction of dispersed phase, ϕ_{dp}. Two types of emulsion are readily distinguished in principle, depending upon which kind of liquid forms the continuous phase as: oil-in-water – O/W, for oil droplets dispersed in water; and water-in-oil – W/O, for water droplets dispersed in oil [33].

Emulsions are widely used materials for many industrial applications such as cosmetics, foods, pharmaceutics, paintings, coatings, etc [32,33]. But recently, emulsions have been used as efficient intermediates in the production of porous materials via direct foaming process [34].

Emulsification involves the sudden creation of a large amount of new liquid interface. Thermodynamically, in order to increase the oil–water surface area by an amount ΔA, the required work (free energy change) is $\Delta G = \gamma \Delta A$, where γ is the interfacial tension. In order to disrupt a droplet of radius a into a smaller one requires an external pressure gradient of magnitude $\Delta p/a = 2\gamma/a^2$, where Δp is the Laplace pressure.

During homogenization, the fluctuating stress differences needed to produce such a high local pressure gradient are generated from the intense laminar flow (shear and extensional deformations) and/or inertial effects (turbulence and cavitation) [35]. The mean droplet diameter, which determines most of the emulsion properties (stability, rheology, optical properties, etc), is strongly dependent upon the fragmentation procedure. According to the pioneering work of Taylor, in quasi-static conditions, an isolated and spherical droplet of radius R_0 (relatively low viscosity, η_d)

is dispersed in a fluid of viscosity η_c, the droplets will deform into an ellipsoid or elongated cylinder [30,36]. The rupture of these elongated cylinders in smaller droplets is achieved by the so-called Rayleigh instability reducing the high interfacial energy due to the elongated droplets. Deformation of the dispersed phase occurs when the shear stress $\eta_c \cdot \dot{\gamma}$ surpasses the interfacial stress σ/R_0, where $\dot{\gamma}$ is the shear rate and σ is the interfacial tension. The ratio between these two stresses is defined as the capillary number (Ca). When the capillary number exceeds a critical value, C_{acrit}, the elongated droplet will rupture into smaller droplets of average radius R according to Eq. (1.1). C_{acrit} depends on the viscosity ratio between dispersed and continuous phase (η_d / η_c) and the type of flow:

$$R \propto Ca_{crit} \frac{\sigma}{\eta_c \dot{\gamma}} \tag{1.1}$$

The fragmentation process involves two distinct regimes: the first one at short time (shorter than one second), the droplet diameter decreases abruptly and the obtained diameter is determined by the applied stress (weakly depends on the viscosity ratio η_d / η_c). While the second mechanism is slower of the order of hundred seconds is less efficient for fragmentation [32].

Surfactants molecules adsorb spontaneously at the oil/water interface of the freshly formed fine droplets, reducing the interfacial tension and preventing them from coalescence. The final droplet-size distribution is determined by the time taken for the interface to be covered with emulsifier, as compared with the average time interval between droplet collisions (considering a fixed rate of energy dissipation during emulsification) [31,35]. One should consider the deformability of the droplets in concentrated emulsions (volume fraction > ϕ *=0.64, for randomly packed monodisperse spheres), corresponding to a close packing of hard spheres, where the emulsion become remarkably rigid and resemble an elastic solid. Indeed, two droplets forced together will begin to deform before their interfaces actually touch, because of the intrinsic repulsive interactions between them [37].

In this work, we mainly will focus on concentrated emulsions (HAPES) stabilized by surfactants, envisaging the development of advanced cellular ceramics based on Si_3N_4 by direct foaming processing route.

1.2.2 Gelcasting

Gelcasting is a well-established colloidal processing method for making high-quality, complex-shaped dense or porous ceramic parts by means of in situ formation of a percolating network of ceramic particles. Is a near-net-shape (NNS) technology, based on the fast consolidation of a homogeneous suspension into a stiff solid-like sample (gel), allows to produce green parts with the final shape (or most similar as possible) [38,39]. The versatility of this processing route enables the production of porous ceramics with high shape complexity and good mechanical properties.

According to Sepulveda, this technique originally developed to produce dense bodies, and has been adapted by Smith for the manufacture of porous ceramics using foamed suspensions [40]. The process combines the gelcasting of ceramics with foaming, and consists is preparing suspensions of high solid loading with reasonably low viscosity. Afterwards, the bubble incorporation proceeds usually by mechanical frothing and then solidifying the foamed slurries. Control of pore size and connectivity is possible through density variation and expansion of the foams before setting. Pores are typically spherical and can be either closed or opened exhibiting interconnecting windows (bubble disproportionation) [2]. Cell interconnectivity is most likely formed by a local differential shrinkage of the particle layer around the air bubbles during the gelation process, which, favors the rupture of the particle coating around the bubbles, leading to interconnecting cells after drying and sintering [41].

Disadvantages are the amount of liquid and the levels of shrinkage involved during drying of the bodies, and also the toxicity of the monomers originally used and the necessity to atmosphere control avoiding contact with oxygen environments to accomplish the polymerization reaction are the main disadvantages of this method [2,40]. As pointed out by Studart et al., several alternative methods that apply environmental-friendly setting agents from the food industry have been developed to overcome the disadvantages of the original gelcasting technique. The temperature or pH-induced gel formation of various biopolymers as gelatin, ovalbumin, and bovine serum albumin (BSA), for instance, have been successfully used for setting the foam wet structure. A similar approach relying on the temperature-induced gelling of polysaccharides such as sucrose, agar, carrageenan, starch and wheat particles has been recently applied as non-toxic processing route for the fabrication of porous ceramics. The speed of the setting reaction is another important criterion when selecting direct foaming methods for fabrication of porous ceramics, since many of these alternative-setting methods are considerably slower than the original polymerization reaction [2]. The main difficulty of using biopolymer solutions in processing of cellular ceramics by foaming

method is concerned to their high viscosity, which prevents the foaming capacity of the ceramic suspension. Another important feature concern to the gel that must be sufficiently strong to withstand the body weight, even at the typically low solids loading used in these suspensions [42].

Protein chemistry – Thermal gelling

The fundamental property of globular proteins: their gelling (coagulation) ability in water when heated to a certain temperature is the key for the manufacture porous silicon nitride foams by gelcasting.

Globular proteins such as albumen (egg white) are characterized by regular structural elements of aminoacid sequences mixed with randomly extended chain segments. In the initial state the protein molecules are folded into spherical configurations (few nanometers), similarly to small particles with specific surface chemistry. Under certain conditions (thermal, chemical, etc.), globular protein molecules can gel in water depending on the pH. Prior to the gel formation a denaturation process occurs and consists of loss of native structure and biological activity of a protein through a breakdown of the structure i.e., hydrogen bonds, are broken and random coil or metastable forms are formed, which makes the globular protein more disordered exposing more hydrophobic residues [43]. Irreversible denaturation of albumen occurs when the unfolded peptide chain is stabilised by interactions with other chains. The polypeptide chains become tangled to form a three-dimensional and thermo-irreversible gel network (coagulation) through the formation of new hydrogen bonds between the chains, which transforms the suspension into a rigid body (Figure 1.3) [44].

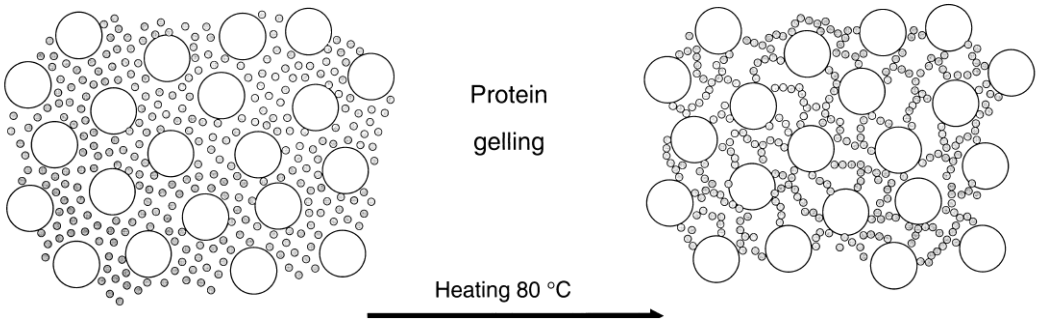

Fig 1.3. Schematic illustration of the gel formation with a globular protein in a ceramic powder suspension.

Globular proteins also show surface-active properties, for example by attraction to air/water interfaces, which gives a tendency to foam formation in water; a disadvantage if the purpose is to produce fully densified ceramic materials using this method. When adding a globular protein to a ceramic slip through a mixing operation, air bubbles are introduced, and the protein molecules are adsorbed at the interface between air and water via hydrophobic areas, and a partial unfolding (surface denaturation) occurs. The decrease in the surface tension caused by protein adsorption facilitates the formation of new interfaces and more bubbles are created. The ability of protein molecules to form and stabilise foam depends on the diffusion rate and denaturation i.e., to form a strong, viscoelastic surface layer, so as to reduce gas permeability and inhibit coalescence [43,44].

Polysaccharides chemistry – Thermal gelling

Polysaccharides refers to long carbohydrates molecules with a general formula $C_n(CH_2O)_{n-1}$, where $n \geq 3$. The applications of the polysaccharides depend on their multiple properties, e.g. solubility, viscosity referred to the concentration and their capacity to form gels as a consequence of a temperature change. The most important drawback of thermoreversible gelcasting with polysaccharides is that the as-cast body has a relatively low gel consistency, which is not enough to allow a proper handling and can lead to deformation and some cracking before it becomes stiff. In this case a complementary consolidation stage, as a fast drying process, is necessary in order to make the process competitive in industry. However, the use of these polysaccharides in ceramic forming has also important advantages e.g., use of aqueous concentrated suspensions, low biopolymer amount is required (<1wt% referred to powder content), is a simple process, which provide high homogeneity, microstructural uniformity, and suitable mechanical strength [39].

Agaroids (agar and agarose) and carrageenan are polysaccharides extensively used to promote the formation of a physical gel on cooling by cross-linking of the double helical through hydrogen bonding. The gelling mechanism of agars and carrageenans, referred to as syneresis (Figure 1.4), which consists in aggregation of molecules of different chains, the water access is blocked and the polysaccharide becomes insoluble, so that there is a water exclusion phenomenon at the junction zones [39].

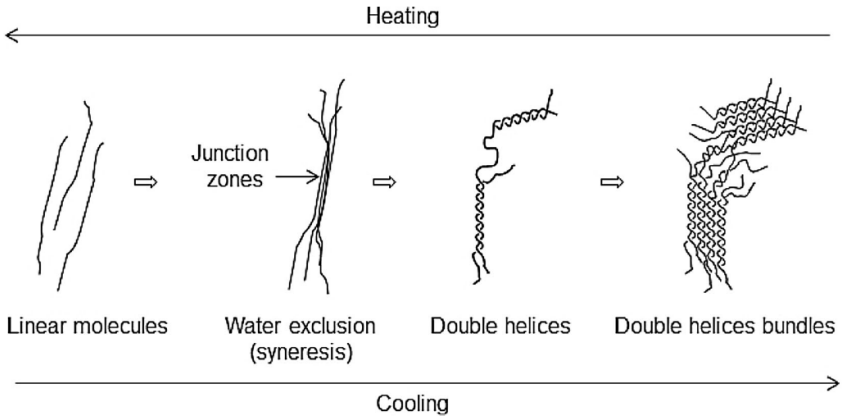

Fig 1.4. Schematic representation of the gelling mechanism of agars and carrageenans.

Methylcellulose (MC) and hydroxypropyl-methylcellulose (HPMC) are a group of polysaccharides that gel on heating, as a result of hydrophobic interaction between molecules containing methoxyl substitution. At low temperature, the molecules are hydrated and there is a little polymer–polymer interaction; but when the temperature increases, the molecules lose their water of hydration, and a polymer–polymer association takes place, allowing a network structure with a sharp rise in viscosity. The gelling temperature is a function of the concentration of the methylcellulose solution, and can be modified by some additives as glycerol or ethanol, which decreases and increases the gelling temperature, respectively. Additionally, the gel strength depends on the concentration of methyl groups and the methyl/hydroxypropyl ratio [39].

In addition, the hydrophobically modified cellulose derivates (MC and HPMC) are amphiphilic biopolymers that can be used as emulsifiers, since they are surface-active hydrocolloids. However, the droplets produced are coarser than those stabilized by low-molecular-mass surfactants or proteins under similar conditions, as a consequence of the high molecular weight of these cellulose polymers [45].

1.3 Si_3N_4 based ceramics

1.3.1 Colloidal processing: Si_3N_4 suspensions

The colloidal processing is an attractive route to process Si_3N_4, which provides high reliability and good homogeneity of final properties by cost-effective pressureless sintering.

However the preparation of a well dispersed, uniform and concentrated slip of a submicrometric Si_3N_4 powder with the corresponding sintering additives is considered a critical step, which depends of the powder fabrication and characteristics, such as, oxygen content, and the amount of impurities in the powder [46]. The oxygen distribution in the nitride powders strongly influences the stability and rheology of suspensions for colloidal powder processing and casting techniques [47]. The formation of undesired hard agglomerates is detrimental to slip and sintered properties and must be prevented during the wet-processing stage, since they lead to non-uniform sintering rates that result in structural flaws and incomplete densification [48].

Stabilizing forces that result from electrical double-layer repulsion or steric interactions, if sufficiently large in magnitude, can provide an energy barrier against aggregation. In the absence of such forces, particles are subject to attractive van der Waals forces at short interaction distances during collisions. Polyelectrolytes dispersants provide enhanced stability via electrosteric forces [48].

Hackley investigate the Si_3N_4-water-poly(acrylic acid) system in alkaline conditions, pH ≥ 9, and show that the carboxylic acid groups present on PAA completely dissociate (producing a negatively ionized polymer) above pH 10. As a consequence of a ionization PAA polymer change configuration from a compact random-coil at low pH to a fully extended and rigid molecule at high pH, owing to depletion stabilization [48,49].

The surface composition of Si_3N_4 particles often is an intermediate state between silica (SiO_2) and silicon oxynitride, and additionally, two kind of different groups are present: silanol groups and silylamine (secondary and/or primary) groups. The ionization of silanol and amine groups depends mainly on the pH value of the aqueous slips. The silanol groups show acidic behavior and consequently low pH_{IEP}, while the amine groups show basic behavior and high pH_{IEP} [50].

The principles involved in stabilization of suspensions, emulsions and foams have many similarities, and destabilization mechanisms like sedimentation, aggregation and coalescence normally take place [33].

1.3.2 Si_3N_4 crystal structures

Silicon nitride crystal structure exists in two major crystalline forms: α– and β–phase. α–Si_3N_4 is a low temperature modification and β–Si_3N_4 is the high temperature modification. Both phases have a hexagonal crystal structure and $P6_3/m$ is the space group of β–phase and *P31c* for

α–phase. The lattice parameters of β–Si_3N_4 are a = 7.6044 Å and c = 2.9075 Å, possessing an atomic layer sequence of ABAB and forming long continuous channels in c direction, while the corresponding parameters for α–Si_3N_4 are a = 7.7541 Å and c = 5.6217 Å, with an atomic layer sequence of ABCD [51,52]. Both structures are built up from a SiN_4 tetrahedron and can be transformed into each other by a 180° rotation around an axis normal to the c direction (Figure 1.5) [51,53].

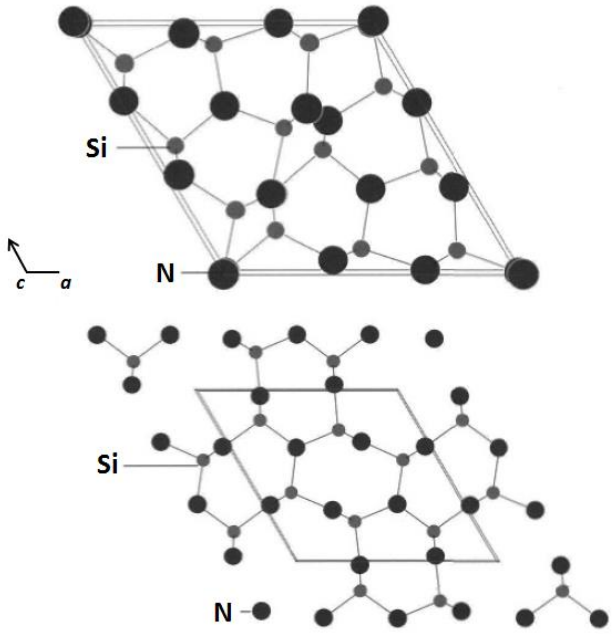

Fig 1.5. Projection of the crystal structures α–Si_3N_4 (on the top), and β–Si_3N_4 (on the bottom) [54].

The α→β transformation requires a lattice reconstruction [52], which involves breaking and reforming six Si–N bonds in each unit cell. This reconstruction of the crystal structure requires short-range diffusion rather than simple translation, and diffusion occurs as a result of the concentration gradient of α–Si_3N_4 rich powders [9]. The diffusion of silicon and nitrogen takes place through the liquid phase at temperatures in excess of 1400 ºC [52], through a dissolution of the fine α particles in the liquid phase formed between sintering aids and subsequent precipitation of the β nuclei by solution re-precipitation mechanism [51].

According to Krstic et al., if the amount of liquid phase during sintering is sufficient, the final structure consists of only elongated β–Si_3N_4 phase. The growth of elongated β–grains can be

controlled either by the diffusion of the atoms through the liquid or by reaction at the grain/liquid interface. Due to the prismatic configuration of β–Si_3N_4 grains, the growth of length in the c direction [0001] is controlled mainly by the solute diffusion through multigrain junctions, while the growth of width in the [2100] direction is controlled by the diffusion along grain boundaries [51].

1.3.3 Liquid phase sintering

The basic problem in sintering silicon nitride is due to the high degree of covalent bonding (Si-N) and a low diffusion in the solid state the compound dissociates at temperatures high enough to achieve the necessary atomic mobility for sintering to occur. Under conventional pressureless sintering conditions the rates of dissociation versus sintering (densification) are such that high weight losses caused by thermal decomposition of both Si_3N_4 and the SiO_2-rich liquid phase responsible for the densification process and low theoretical densities result [55,56]. Greskovich et al., discovered that a N_2 overpressure would help to suppress the dissociation reactions and permit sintering to near full density, with little weight loss. In order to suppress the dissociation of Si_3N_4 some conditions are necessary: (1) Use ultrafine powders (increases the thermodynamic driving force for sintering and reduces diffusion distances). (2) Use sufficiently high nitrogen pressure, to keep the system to the right of the solid-liquid coexistence boundary [56]. (3) Prevent silicon vapor loss from the system. (4) Have some oxygen present in the system by adding sintering aids (metal oxides or non-oxides additives) [55].

The role of nitrogen pressure in thermal decomposition of Si_3N_4 is illustrated in Figure 1.6, which shows the stability diagram for Si_3N_4 in equilibrium with Si and N_2. From a practical point of view, safe sintering processes require a nitrogen pressure that is higher than the equilibrium pressure of N_2 according to Eq. (1.2), since silicon nitride decomposes at high temperatures, above ~1500°C, into silicon and nitrogen [18,56].

$$Si_3N_4\,(s) \rightarrow 3Si\,(l) + 2N_2\,(g) \qquad (1.2)$$

The set of lines from lower right to upper left are isotherms and the solid curve from lower left to upper right is the condensed silicon/silicon nitride/gas coexistence boundary that depicts nitrogen pressures above which silicon nitride exists as a solid if silicon vapor is not removed from the system.

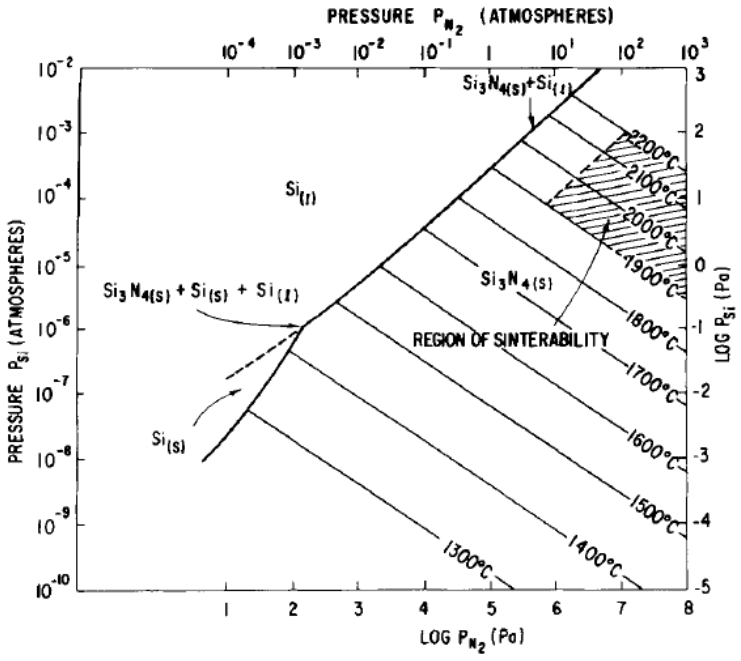

Fig 1.6. Stability diagram for Si_3N_4 in equilibrium with Si and N_2. The cross-hatched area exhibit the region of sinterability determined experimentally [56].

According to Ziegler et al., the addition of sintering aids that forming a suitable liquid, is the most important step in the densification of Si_3N_4. Moreover, if the liquid phase promotes good wettability and solubility of Si_3N_4, densification can be described according to the mechanisms of liquid phase sintering formulated by Kingery: rearrangement, solution-diffusion-precipitation, and coalescence [12,57].

As point out for Kingery, the driving force leading to densification during sintering in the presence of a liquid phase is the over-all surface energy, which markedly accelerates the sintering rate and the material transport phenomena [57].

The sintering additive reacts with the phases containing oxygen, SiO_2 or oxynitride, which are always present on the particle surfaces of commercially available Si_3N_4 powders, to form the liquid phase. Impurities in the starting powder are often also incorporated in this silicate melt. Depending on the amount and viscosity of liquid phase at sintering temperature, rearrangement processes will occur induced by capillary forces. The degree of densification in this first stage is mainly dependent on the particle size, shape and distribution, as well as solid contacts formed by neck formation during heating, and the amount and viscosity of the secondary phase [58].

With increasing temperature, the rearrangement efficiency decreases and the solution-diffusion-precipitation process becomes dominant. The driving force in this second stage is the higher solubility at the contact points of the particles caused by capillary forces as well as the differences in the chemical potentials between small and large particles, which lead to an enhanced solution of small particles. As a result of the accelerated diffusion of the dissolved species in the silicate liquid compared to that of self-diffusion in Si_3N_4 (the diffusion rate is increased by about ten orders of magnitude), the densification rate is essentially increased. In addition, these processes can be accelerated by the simultaneous application of external pressure, as in the case of hot-pressing and hot isostatic pressing [12].

High α–amount (≥ 95%) is usually employed because it becomes thermodynamically unstable at temperatures ≥ 1400 °C causes an enhancement of the solution and exhibits the tendency to transform into the stable β–phase.

Moreover, precipitation of the dissolved material from the liquid phase is affected by the phase composition of the starting material, for example, if the starting powder contains a large number of β–particles, the fine particles start to dissolve due to their higher chemical potential. The dissolved species continuously precipitate on the coarser original β–particles under nearly equilibrium conditions in such a way that their surface energy is minimized leading to large spherical or equiaxed grains. If, however, the starting powder contains only a low concentration of β–grains, high supersaturation in the liquid phase (with respect to β–Si_3N_4) is created locally due to the lack of sufficient β–nuclei, resulting in a spontaneous nucleation and crystallization of idiomorphic rod-like β–grains, far from the thermodynamic equilibrium. This type of elongated β–morphology prepared from α–Si_3N_4–rich starting powders, and is very important for the mechanical properties [12].

The third stage of the liquid-phase sintering process is coalescence, which gives nearly no contribution to further densification. In this stage, however, grain coarsening takes place which - due to the effort to minimize the surface energy - is in many cases accompanied by an unfavorable change in morphology from the idiomorphic rod-like to a more equiaxed grain structure.

The liquid silicates solidify during cooling mostly to amorphous or partially crystalline phases, which are arranged at the grain boundaries in thin layers or at the grain-boundary triple junctions, and this strongly affects the high-temperature properties of ceramic components. The resulting microstructure is schematically shown in Figure 1.7 [12].

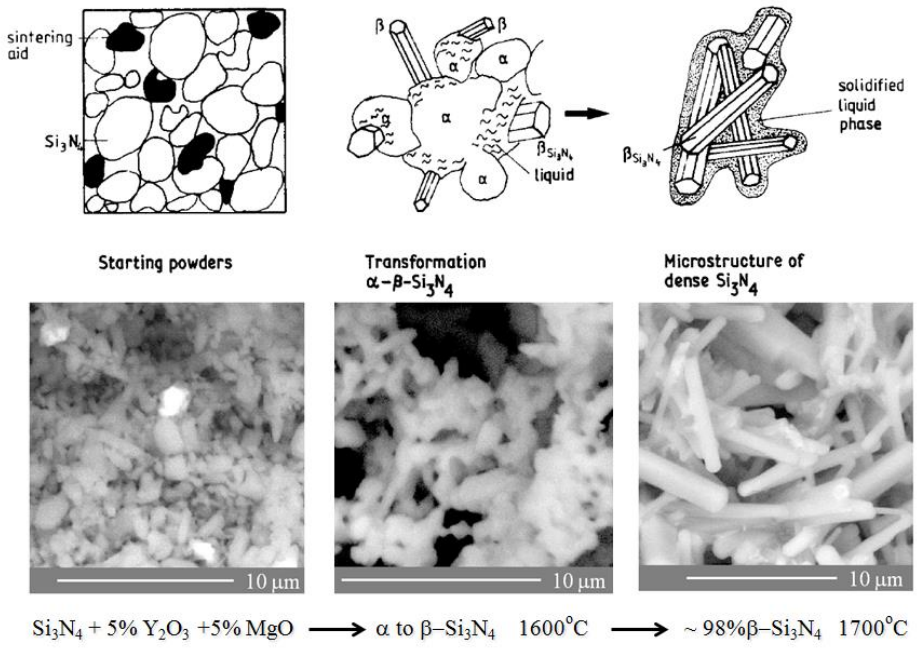

Fig 1.7. Microstructure of Si_3N_4 components resulting of the increasing in the temperature: schematic representation (on the top); original SEM images resulting of this study.

Si_3N_4–Y_2O_3–MgO System

Although the transformation of α → β–Si_3N_4 is a widely known phenomenon the formation of a specific grain size and aspect ratio is not an easy controlled process.

The chemistry and quantity of the liquid phase, along with the characteristics of the starting powders and processing conditions, are the key factors in determining the microstructure and properties of silicon nitride parts [59].

According to Pyzik and Beaman, self-reinforced silicon nitrides has been developed based on the Si_3N_4–Y_2O_3–MgO–CaO system where the yttria acts as a conversion aid, magnesia as a densification aid, and calcium oxide as a whisker growth-enhancing agent [18]. The mixture of these components can alter the glass chemistry enable the formation of microstructures with grains having varying size, aspect ratio, and quantity. The microstructure evolution as a function of glass chemistry is schematically illustrated in Figure 1.8 [59].

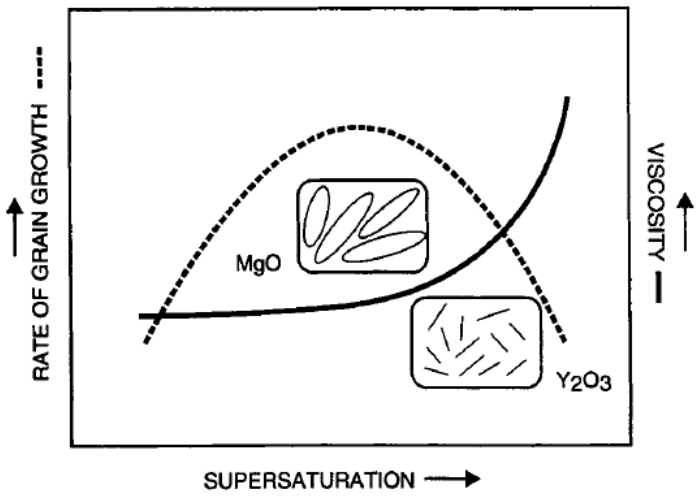

Fig 1.8. Schematic illustration of microstructure evolution as a function of glass chemistry.

The microstructure of Si_3N_4 ceramics produced from low viscosity glass (MgO) are characterized by large grains, owing to the low viscosity glass provides rapid mass transport and supersaturation. Additionally, the number of grains is low, since the small grains dissolve in the glass by Ostwald-rippening mechanism. In high-viscosity systems (Y_2O_3), slow mass transport in the glass causes a reduction in the rate of grain growth, leading to higher number of grains, smaller size and broader distribution, due to reduced solution-reprecipitation process.

The presence of elongated grains in Si_3N_4 is a necessary, but not sufficient condition for improved properties [59].

1.4 Max phases materials

Ternary compounds, commonly referred to as MAX phases, with the general formula Mn+1AXn; where n = 1, 2, or 3, M is an early transition metal, A is an A-group element (mostly IIIA and IVA), and X is carbon and/or nitrogen, see the hexagonal structure with space group P63/mmc illustrated in Figure 1.9, which present a combination of metallic, covalent, and ionic bonding [60,61,62].

They are sometimes termed metallic ceramics [63], since they combine several important properties of metals and ceramics, such as high mechanical strength, good plasticity and high

thermal expansion and electrical conductivity, which can be connected with the metallic nature of the bonding, as well, their layered structure [64].

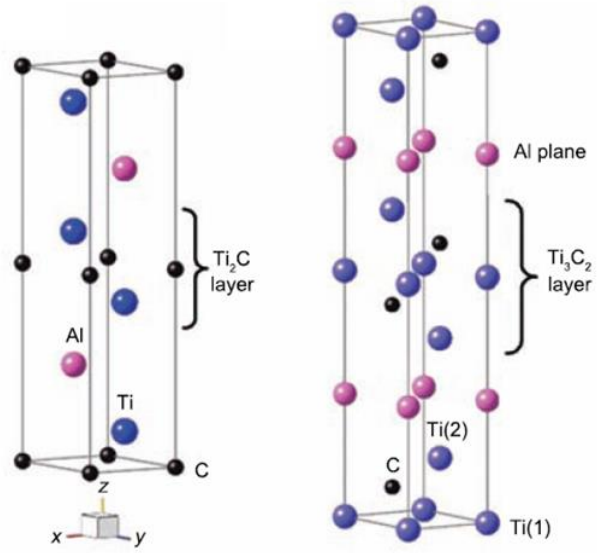

Fig 1.9. Crystal structures of Ti_2AlC (on the left) and Ti_3AlC_2 (on the right) [65].

The Al–Ti–C ternary system, Figure 1.10, comprises three complex carbides: Ti_2AlC, Ti_3AlC and Ti_3AlC_2. Ti_2AlC is the most stable ternary phase (homogeneous composition $Ti_2AlC_{0.69}$ at ~1300^{o}C, but melts incongruently at ~1625 + 10 ^{o}C) [66]. It is readily machinable, thermal-shock resistant, thermally and electrically conductive, anomalously soft (Vickers hardness of 4.5 GPa) and damage tolerant as metals. On the other hand, like ceramics, Ti_2AlC has a relatively low coefficient of thermal expansion (8.2 x10^{-6} $^{o}C^{-1}$), and it is refractory, elastically stiff (Young's modulus of 277 GPa) and exceptionally oxidation-resistant, combined with the highest melting point ~1625 ^{o}C, lightweight and oxidation resistant, one can expect its use as high-temperature structural material [64,65,67].

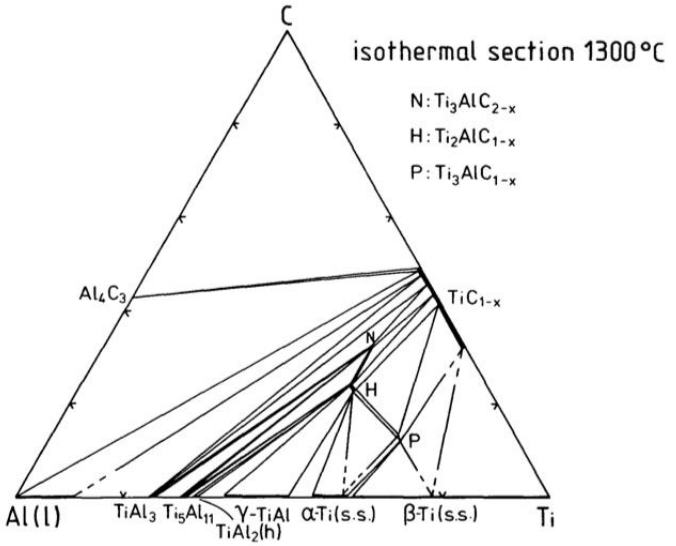

Fig 1.10. Isothermal section for the entire composition range of Ti-Al-C ternary system [66].

According to Radovic and Barsoum, Ti_2AlC is the most oxidation-resistant MAX phase because it forms a stable and protective Al_2O_3 layer in oxidizing environments that can withstand thermal cycling up to 1350 °C for 10.000 cycles without cracking (Figure 1.11) [60]. This very well adhered oxide layer exhibits a high density and that will slow down diffusion of more oxygen and therefore prevent further oxidation [68].

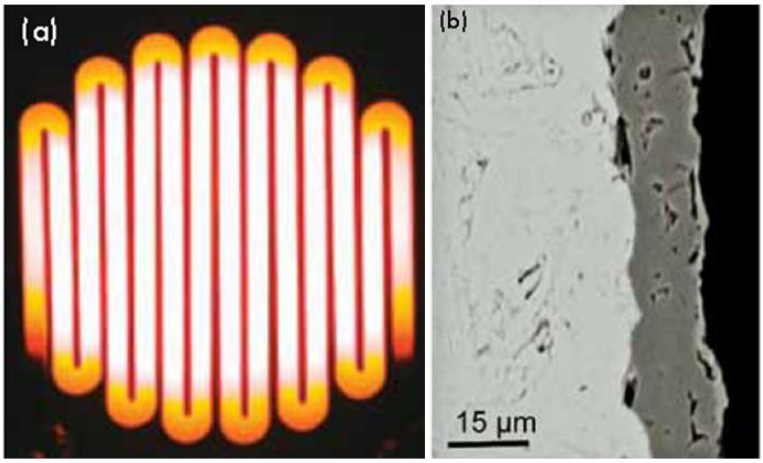

Fig 1.11. Application of max-phases: (a) Ti_2AlC-based heating element resistively heated to 1450 °C in air. (b) Micrograph of the Al_2O_3 oxide layer after 10.000 thermal cycles up to 1350 °C

showing no spallation or cracking of the oxide layer) [60].

An intriguing aspect of the MAX phases is that when a cyclic loading in compression or tension is applied results in spontaneously reversible hysteretic loops whose shape and size are strong functions of grain size [69]. This nonlinear elastic behavior can be related to the basal plane dislocations (BPD), which are mobile, abundant, and able to multiply in the MAX phases at ambient temperatures. However, they are constrained to the basal planes, which results in an important micromechanism based on the formation, growth, and annihilation of incipient kink bands (IKBs), i.e., plastic instability, or buckling during cyclic loading.

A simplified version of the actual model is presented herein in; a more detailed exposition can be found elsewhere [70].

When the MAX phases are loaded, initially the "soft" grains deform - those with basal planes favorably oriented for easy slip - causing the "hard" grains (red grains in Figure 1.12 d,e,f) to develop incipient kink bands (IKB, Figure 1.12 d). The latter are coaxial dislocation loops that, as long as their ends are not sundered, are spontaneously and fully reversible. With further increase in applied load, if the polycrystal does not fail by shear band formation or fracture, the IKBs result in mobile dislocation walls (MDW, Figure 1.12 e) and ultimately permanent kink bands that lead to delamination (Figure 1.12 f, g) at the individual grain level and considerable plasticity [60].

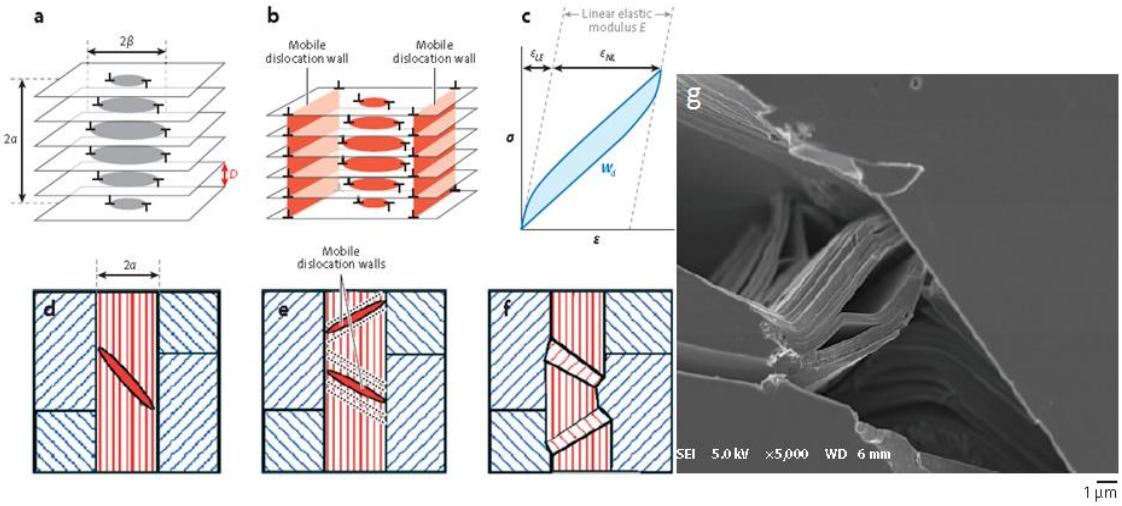

Fig 1.12. Application Schematic representation of kink band formation: (a) elliptic subcritical kink band (KB); (b) Formation of incipient kink band (IKB) in hard grains; (c) Schematic of the stress-strain hysteresis loop due to formation and growth of IKBs during loading and their annihilation during unloading; (d) IKBs in hard grains (fully reversible at this stage); (e) Multiple mobile dislocation walls in a large grain; (f) Permanente kink bands (KBs); and (g) Field-emission

scanning electron microscope image of a bridged crack in a coarse-grained Ti_3SiC_2 microstructure showing a significant amount of delamination [69].

Given the remarkable set of properties that the MAX phases exhibit, especially their high-temperature stability, thermal shock resistance, damage tolerance, good machinability, and the exceptional oxidation resistance makes Ti_2AlC promising for high temperature applications, as gas burner nozzles in corrosive environments, high temperature bearings, cladding materials in lead-cooled fast-breeder nuclear reactors, high temperature electrodes, among others [60,64].

In this work, we development of Ti_2AlC foams by gelcasting method using an environmentally friendly biopolymer (agarose) as gelling agent, in order to explore the potentiality of cellular Ti_2AlC in several industrial applications such as hot gas filters, solid/liquid separation devices, catalyst supports and thermal insulators.

References

[1] Scheffler M, Colombo P. Cellular ceramics: structure, manufacturing, properties and application. Weinheim: Wiley-VCH; 2005.

[2] Studart AR, Gonzenbach UT, Tervoort E, Gauckler LJ. Processing routes to macroporous ceramics - A review. *J Am Ceram Soc* 2006;**89**(6):1771–89.

[3] Gauckler LJ, Waeber MM, Conti C, Jacobduliere M. Ceramic foam for molten-metal filtration. *J Met* 1985;**37**(9):47–50.

[4] Chen QZ, Rezwan K, Armitage D, Nazhat SN, Boccaccini AR. The surface functionalization of 45S5 Bioglass-based glass-ceramic scaffolds and its impact on bioactivity. *J Mater Sci Mater Med* 2006;**17**(11):979–87.

[5] Chen QZ, Thompson ID, Boccaccini AR. 45S5 Bioglasss - derived glass–ceramic scaffolds for bone tissue engineering. *Biomater* 2006;**27**(11):2414–25.

[6] Colombo P. Conventional and novel processing methods for cellular ceramics. *Phil Trans R Soc A* 2006;**364**(1838):109–24.

[7] Greil P. Advanced engineering ceramics. *Adv Mater* 2002;**14**(10): 709–16.

[8] Green DJ, Colombo P. Cellular ceramics: intriguing structures, novel properties, and innovative applications. *Mrs Bull* 2003;**28**(4):296–300.

[9] Riley FL. Silicon nitride and related materials. *J Am Ceram Soc* 2000;**83**(2):245–65.

[10] Moreno R, Salomoni A, Stamenkovic I, Castanho SM. Colloidal filtration of silicon nitride aqueous slips, part II: slip casting and pressure casting performance. *J Eur Ceram Soc* 1999;**19**(1):49–59.

[11] Yang JF, Beppu Y, Zhang GJ, Ohji T, Kanzaki S. Synthesis and properties of porous single-phase β'-SiAlON ceramics. *J Am Ceram Soc* 2002;**85**(7):1879–81.

[12] Ziegler G, Heinrich J, Wötting G. Relationships between processing, microstructure and properties of dense and reaction-bonded silicon nitride. *J Mater Sci* 1987;**22**(9):3041–86.

[13] Petzow G, Hermann M. Silicon nitride ceramics. In: Jansen M, editor. High performance non-oxide ceramics II. Berlin: Springer Berlin Heidelberg; 2002. p. 47–167.

[14] Yang JF, Deng ZY, Ohji T. Fabrication and characterisation of porous silicon nitride ceramics using Yb_2O_3 as sintering additive. *J Eur Ceram Soc* 2003;**23**(2):371–78.

[15] Hnatko M, Lenčéš Z, Čopan P, Birošová L, Matejov P, Jantová S. Synthesis, characterizations and *in vitro* assessment of the cytotoxicity and genotoxicity of novel silicon nitride-based porous ceramics. *Mater Sci Appl* 2013;**4**(7):407–18.

[16] Yang JF, Zhang GJ, Kondo N, Ohji T, Kanzaki S. Synthesis of porous Si_3N_4 ceramics with rod-shaped pore structure. *J Am Ceram Soc* 2005;**88**(4):1030–32.

[17] Ling G, Yang H. Pressureless sintering of silicon nitride with magnesia and yttria. *Mater Chem Phys* 2005;**90**(1):31–34.

[18] Alper AM. Phase diagrams in advanced ceramics. London: Acad Press Ltd; 1995.

[19] Lange H, Wötting G, Winter G. Silicon nitride-from powder synthesis to ceramic materials. *Angew Chem Int Engl* 1991;**30**(12):1579–97.

[20] Kondo N, Inagaki Y, Suzuki Y, Ohji T. Fabrication of porous anisotropic silicon nitride by using partial sinter-forging technique. *Mater Sci Eng A* 2002;**335**(1-2):26–31.

[21] Inagaki Y, Kondo N, Ohji T. High performance porous silicon nitrides. *J Eur Ceram Soc* 2002;**22**(14-15):2489–94.

[22] Moulson AJ. Reaction-bonded silicon nitride: its formation and properties. *J Mater Sci* 1979;**14**(5):1017–51.

[23] Díaz A, Hampshire S. Characterisation of porous silicon nitride materials produced with starch. *J Eur Ceram Soc* 2004;**24**(2):413–19.

[24] Peng HX, Fan Z, Evans JRG, Busfield JJC. Microstructure of ceramic foams. *J Eur Ceram Soc* 2000;**20**(7):807–13.

[25] Huang Y, Ma L, Tang Q, Yang J, Xie Z, Xu X. Surface oxidation to improve water-based gelcasting of silicon nitride. *J Mater Sci* 2000;**35**(14):3519–24.

[26] Nangrejo MR, Bao X, Edirisinghe MJ. Preparation of silicon carbide-silicon nitride composite foams from pre-ceramic polymers. *J Eur Ceram Soc* 2000;**20**(11):1777–85.

[27] Colombo P, Bernardo E. Cellular structures. In: Riedel R, Chen IW, editors. Ceramics science and technology, structures. Weinheim: Wiley-VCH; 2005. p. 407–42.

[28] Ohji T, Fukushima M. Macro-porous ceramics: processing and properties. *Int Mater Rev* 2012;**57**(2):115–31.

[29] Barg S, Soltmann C, Andrade M, Koch D, Grathwohl G. Cellular ceramics by direct foaming of emulsified ceramic powder suspensions. *J Am Ceram Soc* 2008;**91**(9):2823–29.

[30] Barg S, Moraes EG, Koch D, Grathwohl G. New cellular ceramics from high alkane phase emulsified suspensions (HAPES). *J Eur Ceram Soc* 2009;**29**(12):2439–46.

[31] Georgieva D, Schmitt V, Leal-Calderon F, Langevin D. On the possible role of surface elasticity in emulsion stability. *Langmuir* 2009;**25**(10):5565–73.

[32] Schmitt V, Leal-Calderon F, Bibette J. Preparation of monodisperse particles and emulsions by controlled shear. In: Antonietti M, editor. Colloid chemistry II. Berlin: Springer Berlin Heidelberg; 2003. p. 195–215.

[33] Schramm, Laurier L. Emulsions, foams, and suspensions: fundamentals and applications. Weinheim: Wiley-VCH; 2005.

[34] Moraes EG, Colombo P. Silicon nitride foams from emulsions. *Mater Lett* 2014;**128**:128–31.

[35] Dickinson E. Hydrocolloids as emulsifiers and emulsion stabilizers. *Food Hydrocoll* 2009;**23**(6):1473–82.

[36] Mabille C, Leal-Calderon F, Bibette J, Schmitt V. Monodisperse fragmentation in emulsions: mechanisms and kinetics. *Europhys Lett* 2003;**61**(5):708–14.

[37] Leal-Calderon F, Thivilliers F, SchmittV. Structured emulsions. *Curr Opin Colloid Interface Sci* 2007;**12**(4), 206–12.

[38] Yang J, Yu J, Huang Y. Recent developments in gelcasting of ceramics. *J Eur Ceram Soc* 2011;**31**(14):2569–91.

[39] Nieto MI, Santacruz I, Moreno R. Shaping of dense advanced ceramics and coatings by gelation of polysaccharides. *Adv Eng Mater* 2014;**16**(6):637–54.

[40] Sepulveda P. Gelcasting foams for porous ceramics. *Am Ceram Soc Bull* 1997;**76**(10):61–65.

[41] Gonzenbach UT, Studart AR, Tervoort E, Gauckler LJ. Tailoring the microstructure of particle-stabilized wet foams. *Langmuir* 2007;**23**(3):1025–32.

[42] Potoczek M. Gelcasting of alumina foams using agarose solutions. *Ceram Int* 2008;**34**(3), 661–67.

[43] Dickinson E. Protein adsorption at liquid interfaces and the relationship to foam stability. In: Wilson AJ, editor. Foams: physics, chemistry and structure. Heidelberg: Springer-Verlag;1989. p. 39–53.

[44] Lyckfeldt O, Brandt J, Lesca S. Protein forming—a novel shaping technique for ceramics. *J Eur Ceram Soc* 2000;**20**(14), 2551–59.

[45] Dickinson E. Hydrocolloids at interfaces and the influence on the properties of dispersed systems. *Food Hydrocoll* 2003;**17**(1):25–39.

[46] Moreno R, Salomoni A, Castanho SM. Colloidal filtration of silicon nitride aqueous slips, part I: optimization of the slip parameters. *J Eur Ceram Soc* 1998;**18**(4):405–16.

[47] Greil P. Processing of silicon nitride ceramics. *Mater Sci Eng A* 1989;**109**:27–35.

[48] Hackley V.A. Colloidal processing of silicon nitride with poly (acrylic acid): I, adsorption and electrostatic interactions. *J Am Ceram Soc* 1997;**80**(9):2315–25.

[49] Hackley VA. Colloidal processing of silicon nitride with poly (acrylic acid): II, rheological properties. *J Am Ceram Soc* 1998;**81**(9):2421–28.

[50] Zhang J, Ye F, Jiang D, Iwasa M. Dispersion of Si_3N_4 powders in aqueous media. *Colloid Surf A: Physicochem Eng Asp* 2005;**259**(1):117–23.

[51] Krstic Z, Krstic VD. Silicon nitride: the engineering material of the future. *J Mater Sci* 2012;**47**(2):535–52.

[52] Hampshire S. Silicon nitride ceramics–review of structure, processing and properties. *J Achiev Mater Manuf* Eng 2007;**24**(1):43–50.

[53] Wang CM, Pan X, Rühle M, Riley FL, Mitomo M. Silicon nitride crystal structure and observations of lattice defects. *J Mater Sci* 1996;**31**(20):5281–98.

[54] Petzow G, Hermann M. Silicon nitride ceramics. In: Jansen M, editor. High performance non-oxide ceramics II. Berlin: Springer Berlin Heidelberg; 2002. p. 47–167.

[55] Katz RN. Nitrogen Ceramics 1976–1981. In: Riley FL, editor. Progress in nitrogen ceramics. The Hague: Martinus Nijhoff publ;1983. p. 3–20.

[56] Greskovich C, Prochazka S. Stability of Si_3N_4 and liquid phase(s) during sintering. *J Am Ceram Soc* 1981;**64**(7):C-96-C-97.

[57] Kingery WD. Densification during sintering in the presence of a liquid phase. I. Theory. *J Appl Phys* 1959;**30**(3):301-306.

[58] Weiss J, Kaysser WA. Liquid phase sintering. In: Riley FL, editor. Progress in nitrogen ceramics. The Hague: Martinus Nijhoff publ;1983. p. 169–86.

[59] Pyzik A, Beaman D. Microstructure and properties of self-reinforced silicon nitride. *J Am Ceram Soc* 1993;**76**(11):2737–44.

[60] Radovic M, Barsoum MW. MAX phases: bridging the gap between metals and ceramics. *Am Ceram Soc Bull* 2013;**92**(3):20–27.

[61] Barsoum MW, Radovic M. Elastic and mechanical properties of the MAX phases. *Annu Rev Mater Res* 2011;**41**:195–227.

[62] Zhou Y, Sun Z. Electronic structure and bonding properties of layered machinable Ti_2AlC and Ti_2AlN ceramics. *Phys Rev B* 2000;**61**(19):12570.

[63] Sun ZM, Hashimoto H, Zhang ZF, Yang SL, Tada S. Synthesis and characterization of a metallic ceramic material–Ti_3SiC_2. *Mater Trans* 2006;**47**(1):170–74.

[64] Hu L, Benitez R, Basu S, Karaman I, Radovic M. Processing and characterization of porous Ti_2AlC with controlled porosity and pore size. *Acta Mater* 2012;**60**(18):6266–77.

[65] Wang XH, Zhou YC. Layered machinable and electrically conductive Ti_2AlC and Ti_3AlC_2 ceramics: a review. *J Mater Sci Technol* 2010;**26**(5):385–416.

[66] Pietzka MA, Schuster JC. Summary of constitutional data on the aluminum-carbon-titanium system. *J Ph Equilib* 1994;**15**(4):392–400.

[67] Hashimoto S, Takeuchi M, Inoue K, Honda S, Awaji H, Fukuda K, Zhang S. Pressureless sintering and mechanical properties of titanium aluminum carbide. *Mater Lett* 2008;**62**(10):1480–83.

[68] Wang XH, Zhou YC. Oxidation behavior of Ti_3AlC_2 at 1000–1400 °C in air. *Corros Sci* 2003;**45**(5):891–907.

[69] Barsoum MW, Radovic M. Elastic and mechanical properties of the MAX phases. *Annu Rev Mater Res* 2011;**41**:195–227.

[70] Zhou AG, Basu S, Barsoum MW. Kinking nonlinear elasticity, damping and microyielding of hexagonal close-packed metals. *Acta Mater* 2008;**56**(1):60–67.

Part II

EXPERIMENTAL

II EXPERIMENTAL

2. Silicon nitride foams from emulsions

E. G. de Moraes and P. Colombo, "Silicon nitride foams from emulsions", manuscript partially published in: Mater. Lett., 128 (2014) 128–131.

2.1 Introduction

High performance ceramics, with cellular structure and containing more than 60 vol% of interconnected porosity, find application particularly where the transport of fluids is required, e.g. molten metal and gas filtration at high temperature, gas-burner media, catalyst support, pollutant removal from gaseous or liquid streams [1–6]. Among non-oxide ceramics, Si_3N_4 is one of the most widely used structural ceramic materials because of its outstanding properties, such as high strength and Young modulus, fracture toughness, hardness, wear resistance, refractoriness, corrosion and oxidation resistance [7–9], and low density and expansion coefficient, reasonably high thermal conductivity and good resistance to thermal shock [7,10,11]. However, the high cost of production (generally requiring pressure sintering) is a significant problem limiting the use of Si_3N_4–based ceramics to specialized, high value applications. Concerning porous Si_3N_4, various methods of processing, such as partial sintering [12,13] and reaction sintering [14,15], sacrificial templating using starch consolidation [16], direct foaming [17], gelcasting [18] and preceramic polymers [19] have been used to obtain components to be used in various applications. In particular, porous Si_3N_4 is good a candidate for Diesel Particulate Filters [20,21], membrane/catalysts supports, and reactor beds [22].

Recently, emulsions have been used as efficient intermediates in the production of porous materials via direct foaming processes [2,23,24]. They consist of two immiscible fluids, one being dispersed in the other, in the presence of surface active agents [25], and are thermodynamically unstable because of their large oil-water interfacial area and thus high overall free energy. Therefore surface active agents (e.g. surfactants or proteins) are used to reduce the free energy of the system [26–28]. The objective of the present work was the development of porous Si_3N_4 ceramics employing an emulsion approach that would lead to foams with highly interconnected pores by conventional pressureless sintering.

2.2 Experimental procedure

Si_3N_4 powder from Yantai Tomley (China), purity > 90%, oxygen content 7.4 ± 0.08 wt%, average particle size 0.6 μm, BET 9.6 m2/g, containing above 91.5% of α– Si_3N_4 phase, was used. The equilibrium pH_{iep} 8.2 ± 0.01 of the powder was measured after 24 h aging in water, following the procedure reported in Ref. [29]. High purity Y_2O_3 (d_{50} = 50 nm, Inframat (USA)), and MgO (d_{50} = 4.6 μm, Bitossi (Italy)), were used as sintering additives (5 wt% for both additives) [30]. The powder mixture was wet-milled in ethanol for 4h at 300 rpm using a planetary mill and silicon nitride cylinders, dried, sieved through a 300 μm screen and then treated in air at 600 °C for 2h to improve the aqueous dispersibility [31,32]. Polyacrylic acid (PAA 1 wt% based on the powder content, Sigma-Aldrich, Italy) was used as dispersing agent. Polysorbate (0.22 vol% with respect to the suspension volume, Tween 80, VWR BHD Prolabo, UK), was used as nonionic surfactant. Water-based Si_3N_4 slurries with 35 vol% of solids concentration and containing PAA were prepared by ball milling for 2 hours at 200 rpm. Afterwards, the emulsification process took place at room temperature by addition of the alkane phase (70 vol% of octane or decane, Sigma-Aldrich, Italy), and the mixture was stirred at 700 rpm for 3 minutes. The emulsions were poured in a Teflon mould and dried at ambient conditions for 24 h. Sintering was conducted in two steps: first the samples were pre-calcinated in vacuum at 800 °C (2h; 0.85 °C/min heating rate), to decompose the organic phase; secondly, the samples were heated to 1600 °C (3h, 2 °C/min heating rate) under 99.99 % N_2 [30]. In order to investigate the influence of the temperature in the α→ β transformation, as well mechanical strength a set of samples were sintered in three steps and heated to 1700 °C (3h, 2 °C/min heating rate) under static N_2, in a graphite furnace.

The crystalline phases were determined on powdered samples by X-ray diffractometry (Philips PW 1710; CuKα, 40 kV, 40 mA, 0.05°, 2s). The data were analyzed utilizing the ICSD database, and the weight fractions of the α– and β–Si_3N_4 crystalline phases were evaluated by the method described in Ref. [33]. The microstructure of the Si_3N_4 based foams was investigated by scanning electron microscopy (FEI Quanta 200, FEI Italia, Milan, Italy). Additionally, in order to investigate the influence of the sintering additives and temperature on the microstructure of the Si_3N_4 foams and rod-like β–grains, a set of samples were characterized by a a Schottky-type field emission transmission electron microscope (TEM, JEM-2100F, JEOL, Tokyo, Japan) operated at 200 kV, equipped with an energy-dispersive X-ray spectroscopy (EDX) detector. Electron diffraction (ED) data were collected using a LaB6 based transmission electron microscope (TEM, JEM-2100, JEOL Ltd, Tokyo, Japan) at 200 kV. For TEM study, the sample was crushed into

powder and dispersed in ethanol. Cell size and cell windows sizes were measured by the linear intercept method (ASTM E112-12), using an image analysis program (Axio Vision LE). The average values were obtained considering stereological relations (ASTM D3576-98). The total porosity were calculated from the weight-to-volume ratio of the samples, while the open porosity and bulk density were measured using a mercury porosimeter (Pascal 140/440 Porosimeter 2000, Germany). The mechanical behavior of the Si_3N_4 based foams was determined by uniaxial compression using a universal testing machine (Instron 1121, Instron Danvers, MA; ASTM C133-94; 1.0 mm/min cross-head speed). Five to ten specimens of 10×10×10 mm3 size, cut from larger 50x12 mm3 disks, were tested for each sample. The permeability of the Si_3N_4 based foams was evaluated using Forchheimer's equation for compressible fluids:

$$\frac{P_i^2 - P_o^2}{2PL} = \left(\frac{\mu}{k_1}\right) v_s + \left(\frac{\rho}{k_2}\right) v_s^2 \tag{2.1}$$

in which P_i and P_o are, respectively, the absolute gas pressures at the entrance and exit of the sample, v_s is the superficial gas velocity, determined by dividing the exiting volumetric flow rate Q, by the sample face area A exposed to flow, L (0.5 - 0.8 cm) is the sample's thickness, μ is the gas viscosity (1.77×10^{-5} Pa·s); and ρ is the gas density (1.15 kg·m^{-3}), evaluated for the pressure P_o = 760 mmHg and T = 24 °C. The parameters k_1 (expressed in square meters) and k_2 (expressed in meters), are respectively known as Darcian and non-Darcian permeability coefficients, in reference to Darcy's law, which establishes a linear dependence between ΔP and v_s. These coefficients weigh the contributions of viscous and inertial losses on the total pressure drop, i.e., the influence of viscous and inertial interactions between fluid and the porous medium [34].The contribution of the porous structure in Eq. (2.1) is quantified by the thickness L and permeability parameters k_1 and k_2, which are complex functions of the morphology, size distribution, connectivity and volume of the void fraction [35]. The terms k_1 and k_2 are usually referred as constants, since they are supposed to be independent of the body dimensions and of both fluid and flow conditions, even though they may vary with temperature.

The first term of Forchheimer's equation, $(\mu/k_1)\cdot v_s$ represents viscous energy losses due to friction between fluid layers and prevails at low fluid velocities. On the other hand, the quadratic term, $(\rho/k_2)\cdot v_s^2$, which is not considered by Darcy's equation, although it becomes increasingly significant at high-speed flow rates, and represents the kinetic energy losses due to changes in the direction of motion and to acceleration or deceleration of the fluid caused by changes in the flow path (contraction or enlargement of the pore section or pore tortuosity along the flow

direction)[34,35]. The knowledge of the predominant relationship (linear or quadratic) for the pressure drop curve is critical for designing the best driving equipment for fluid flow in a given application [36].

The experimental evaluation of permeability parameters was carried out with air/argon flow in temperatures ranging from ~ 25 to ~ 650 °C in a laboratory-made hot gas permeameter described elsewhere (see Appendix B.6, Figure B.1). Two to three disks of ~25 mm of diameter and ~6 mm of height were tested for each sample. The air/gas was forced to flow in stationary regime through the cylindrical samples had their lateral surface previously sealed (with Teflon tape or thermal paste depending on the temperature of permeability test), to allow the air flow to occur only in the top-bottom direction. The air/gas velocity was varied between 0 to 6.5 m/sec, using a valve associated with a rotameter. A digital manometer was used to measure the pressure before and after the sample. Following this procedure, a curve $(P_i^2 - P_o^2)/2PL$ versus air velocity was obtained. This allowed k_1 and k_2 values to be adjusted according to the Forchheimer's equation (2.1) [34,36,37].

2.3 Results and discussion

The X-ray diffraction patterns of the as prepared and sintered Si_3N_4 foams are reported in Figure 2.1. The main phase was α–Si_3N_4 in both as prepared and sintered at 1600 °C, and a slight increase in the β–phase was observed after sintering in this temperature, from 12.9% for the as received powders to 28.6% in the sintered foams. When the temperature is increased up to 1700 °C we observe almost totally β–phase transformation around ~98% as estimated based on the ratio of the intensities of the [210] peak for both phases (located at 35.3 2θ for the alpha phase and at 36.1 2θ for the beta phase), using a normalizing factor, *L*, to correct the peak intensities from errors due to extinction and preferred orientations [33]. The latter can be explained by the α to β phase transformation that starts occurring at temperatures exceeding 1500 °C, in the presence of a liquid Y_2O_3-MgO-containing phase through a solution-reprecipitation mechanism that involves the solution of α– and formation of β–phase, but occurs with little transport of material and hence with little densification due to highly viscous liquid formed [38–40]. The peaks relative to the sintering aids disappeared almost completely after heating, because of their incorporation into an amorphous intergranular phase enhancing the homogeneous distribution of liquid phase at the grain boundary [41].

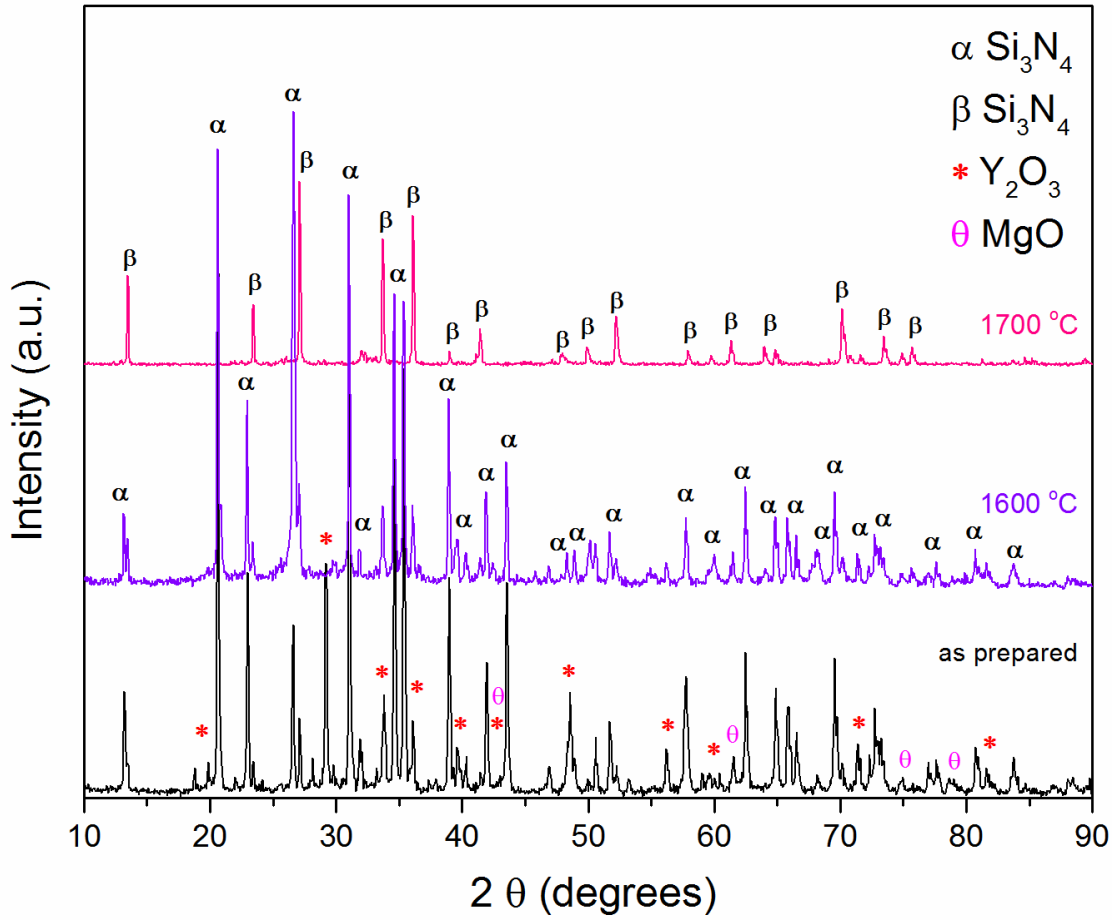

Fig 2.1. XRD patterns for un-sintered and sintered Si_3N_4 foams containing 5 wt% Y_2O_3 and 5 wt% MgO. (ICSD α–Si_3N_4 # 041-0360, β–Si_3N_4 # 033-1160, Y_2O_3 # 043-0661, MgO # 045-0946).

The morphology of the Si_3N_4 foams emulsified with the different alkanes featuring spherical and homogeneously distributed cells and presenting brittle struts is reported in Figure 2.2. The microstructure of these surfactant stabilized foams shows the presence of highly interconnected pores (open cells), that can be related to the aggregation of two or more bubbles that clump together, possibly touching at some points due to Brownian motion. Additionally, stirring cause rupture of thin liquid films between the bubbles enhancing to coalescence and formation of larger bubbles during drying [42] in contrast to particle stabilized Si_3N_4 based foams which possess closed pores [43], because the displacement of powder from the interface is thermodynamically unfavorable, as explained in reference [2]. A weak degree of packing can be observed between the particles in the un-sintered foams, see Fig. 2.2; c for octane and f for decane foams, due to absence

of a binding agent and the fact that no pressure was applied to consolidate the green body. Octane and decane un-sintered foams had different average cell sizes (36 ± 1.4 μm and 58.3 ± 2.3 μm, respectively, see Table 2.1). Occasional larger cells, deriving from trapped air, were also observed in some samples. A distribution in the average cell size values (from 23 to 94 μm) was observed depending on the sample, and in some instances on the region from where the sample was cut, with an associate variation in relative density.

The average cell size and cell window size, the total porosity and the mechanical strength values (see later) of Si_3N_4 un-sintered and sintered foams are summarized in Table 2.1.

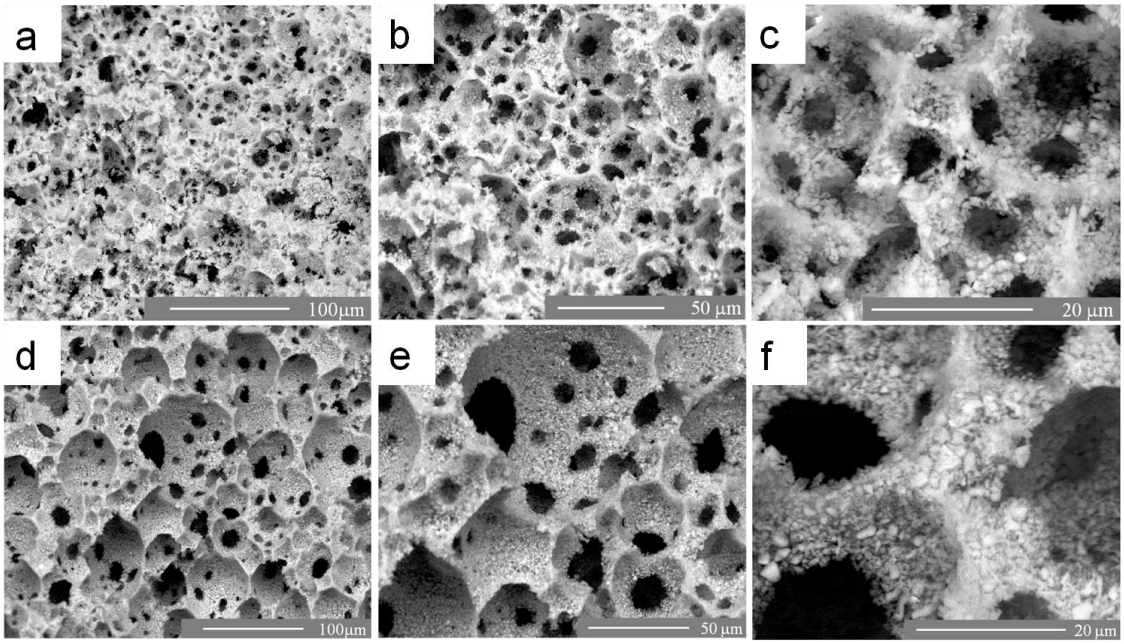

Fig. 2.2. SEM images of the fracture surface of Si_3N_4 un-sintered foams: Octane foam a) and b) general view; c) higher magnification. Decane foam d) and e) general view; f) higher magnification (detail of weak packing of particles on cell walls and struts for both alkanes).

The explanation for the observed differences can be twofold. First of all, as according to Barg [44] the droplet size is independent of the alkane chain length but since decane has a ~10 times lower vapor pressure than octane, we can posit that the slower evaporation can allow for coalescence of the liquid bubbles after foaming, increasing the cell size. The interplay between the setting of the foam by evaporation of the oil phase and the time allowed for the destabilization phenomena of the liquid foam (Ostwald ripening and drainage) controls the cell size and cell size

distribution. Another possible explanation for the variation in cell size is the emulsification process itself, which includes two steps: 1) deformation and disruption of droplets, 2) stabilization of the fresh interface by the emulsifier to prevent re-coalescence. The mean droplet diameter of the emulsions after their production is the result of an equilibrium between droplet break-up and re-coalescence. Emulsion droplets move as a result of Brownian motion and turbulence in the emulsification system, and this leads to collision between droplets and re-coalescence (so called "over-processing") [45,46].

Sintering did not affect the foam morphology, and the spherical and interconnected open cells microstructure was maintained, as showed in Figure 2.3 for Si_3N_4 octane foams sintered at 1600 °C. The average cell size was 31.0 ± 1.1 μm and the cell window size was 6.0 ± 0.8 μm, respectively (see Table 2.1). A linear shrinkage of 13% was measured for the sintered samples, and the amount of total porosity was on the average ~80 vol% the un-sintered and ~75 vol% for the sintered samples, indicating the retention of a large amount of intergranular porosity after sintering, as visible in Fig. 2.3 b. Mercury porosimetry analysis conducted on a selected sample confirmed the presence of cell wall porosity (with a ~0.7 μm size for an octane foam with an open porosity of 70.9 vol% and showed that the amount of closed porosity in that foam was of the order of only ~4 vol%. The size distribution for the microporosity in cell walls and in the struts, as well as for the cell windows obtained by the mercury intrusion method is reported in Table 2.2. According to the literature [14,38], the combination of Y_2O_3 and MgO should enable good sintering at moderate temperatures, such as the ones used in these experiments, but the low compaction of the Si_3N_4 powders in the cell walls of the un-sintered foams most probably contributed to the retention of cell wall porosity after sintering, affecting the mechanical strength. Note the neck formation between particles in Fig. 2.3 c. According to Hampshire et al. [38], solution of α into the oxynitride liquid occurs preferentially at the contact areas between particles for both additives. With MgO, rapid transport of material (low-viscosity glass) allows precipitation of β on the free surfaces, consequently, the distance between particle centres is reduced and densification occurs. While the diffusion through the highly viscous liquid is relatively slow and appreciable precipitation of β– occurs in the contact areas without significant material transport i.e., the transformation takes place without much densification (see Fig.2.3 d, typical rod-like β–Si_3N_4 grains presenting aspect ratio ~4.0 ± 0.6).

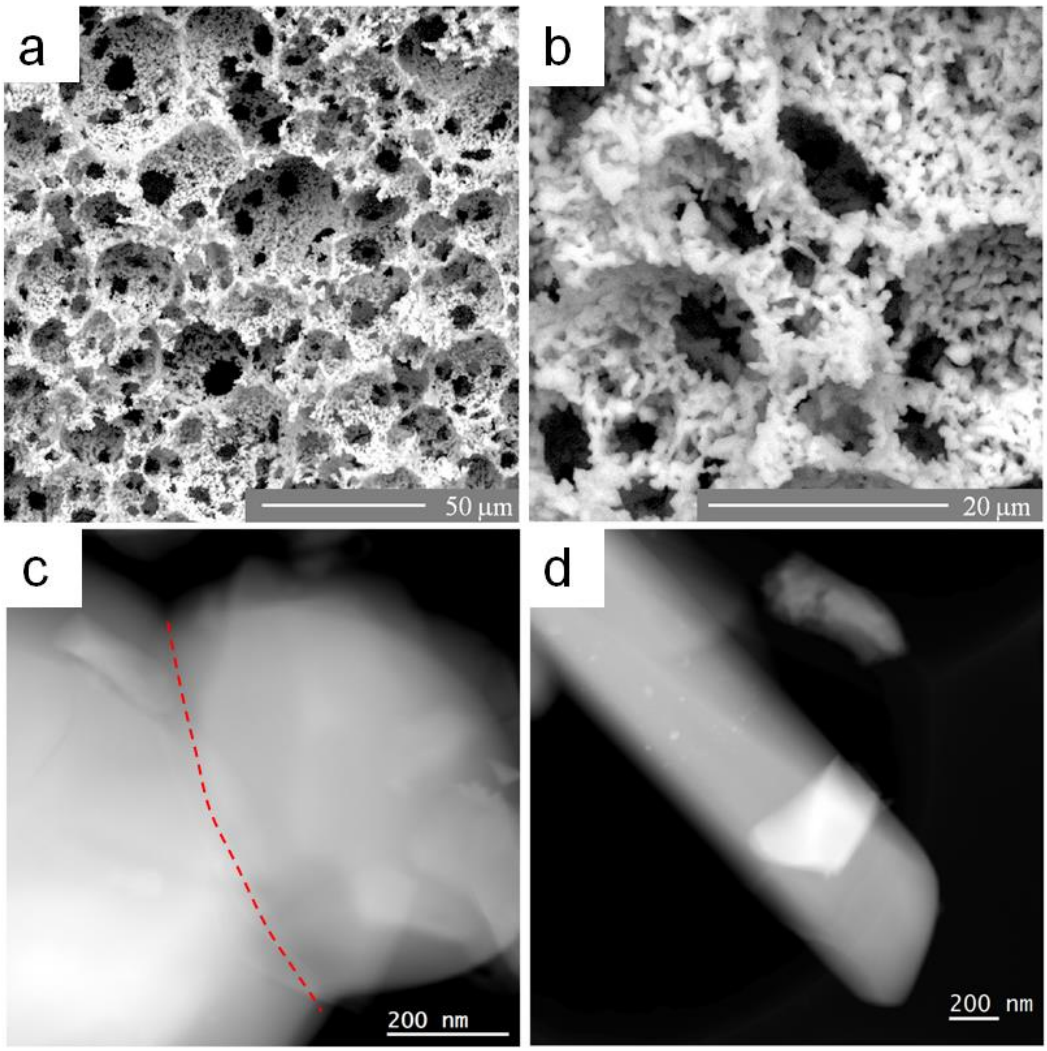

Fig. 2.3. SEM images of the fracture surface of Si_3N_4 sintered octane foams: a) general view; b) higher magnification (detail of cell wall porosity and struts); c) TEM images of the neck formation; and d) detail of typical rod-like β–Si_3N_4 grains.

Figure 2.4 shows the highly interconnected network of spherical cell morphology homogeneously distributed (general view, Fig. 2.4 a), and strut structure presenting residual microporosity (~0.9 μm, see Table 2.2) on the cell walls (see Fig. 2.4 b) of sintered decane foams, since the transformation α→β occurs with little densification [38]. The average cell size was 55.0 ± 2.0 μm and the cell window size was 8.6 ± 1.2 μm (see Table 2.1), respectively. Note that these values are slightly higher than those for octane foams owing to coalescence mechanism. The alkane concentration mainly influenced the amount of total porosity, around 74.0 ± 2.0 vol% (analogous to

octane foams). Fig. 2.4 c shows TEM images of the neck formation between particles during sintering at 1600 °C. HRTEM images (Figure 2.4 d) report high degree of crystallinity into individual α–Si_3N_4 grains. Note the presence of amorphous thin layer on their surface ~1.3 nm thick, as a result of the liquid phase formation during sintering.

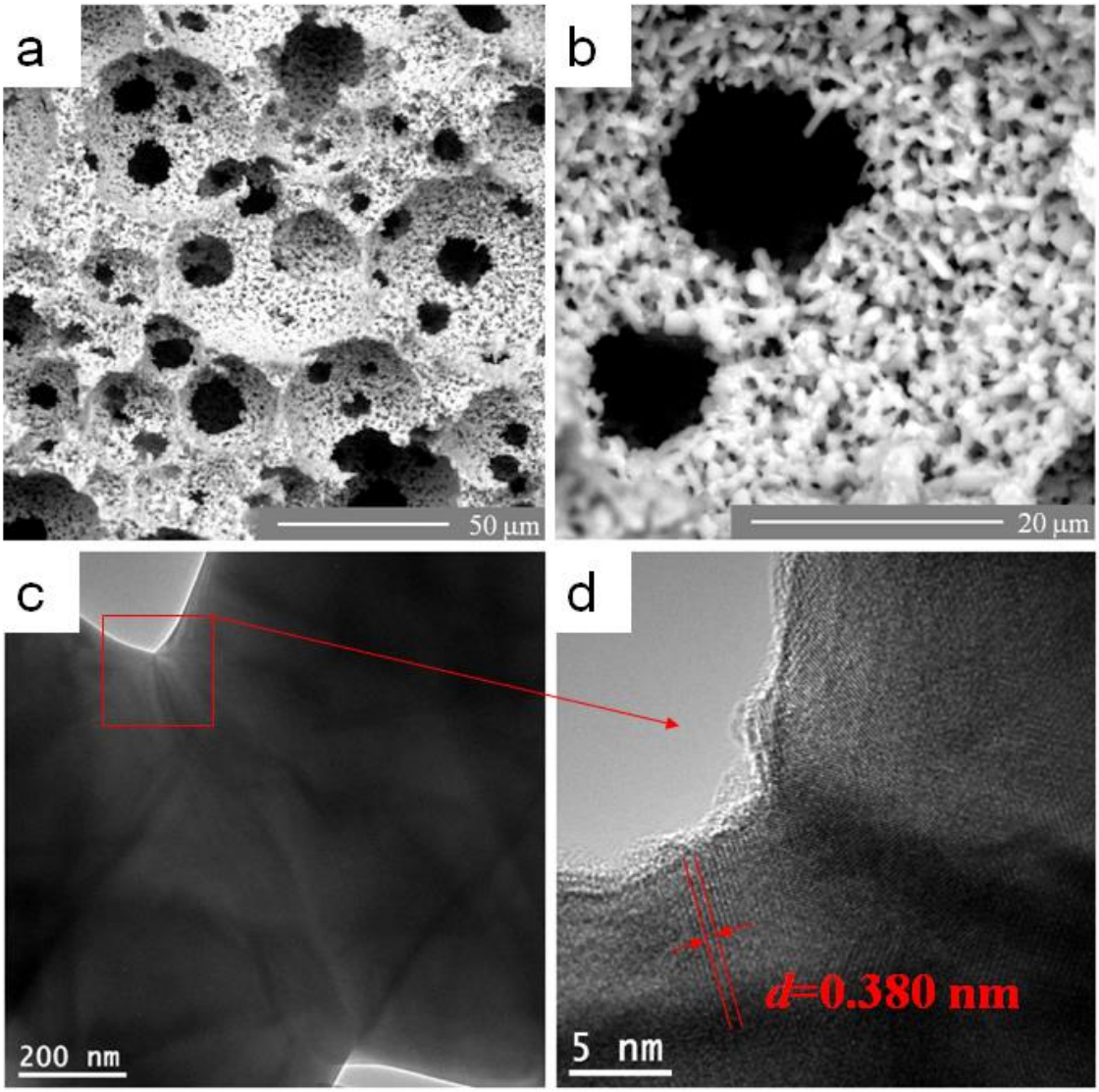

Fig. 2.4. SEM/TEM images of the fracture surface of Si_3N_4 sintered decane foams: a) general view; b) higher magnification (detail of cell wall porosity and struts); c) TEM images of the neck formation; and d) detail of the degree of crystallinity and amorphous thin layer on the α–Si_3N_4 grain surface.

Figure 2.5 presents TEM images of the typical rod-like β–Si_3N_4 grains exhibiting aspect ratio of ~ 5.0 ± 0.7 (on the left) and high degree of crystallinity reported in the HRTEM images (see insets on the right). Note the EDX reporting the presence of yttrium that comes from the initial composition and aluminum as a contamination.

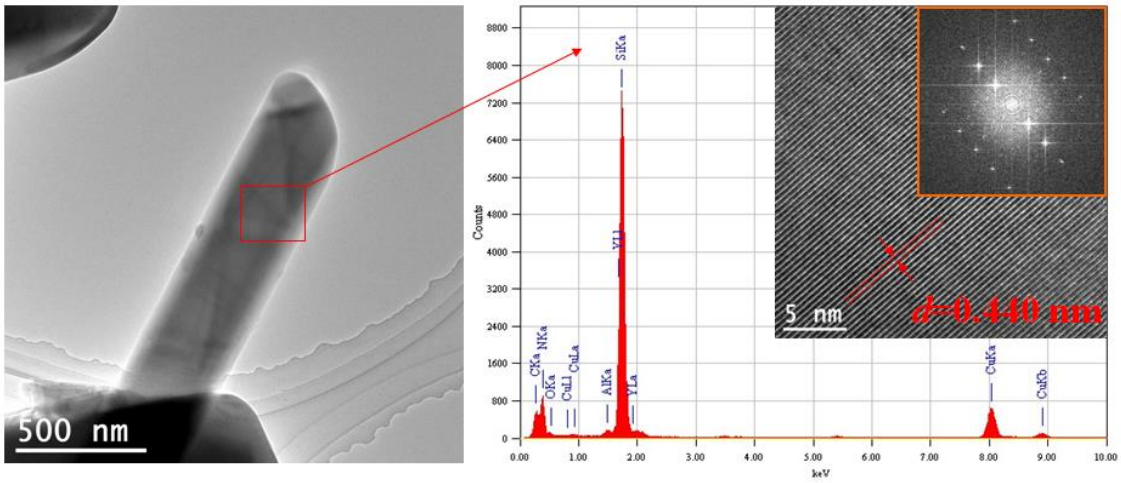

Fig. 2.5. TEM images of the typical rod-like β–Si_3N_4 grains precipitated in the cell walls and struts of decane foams during sintering at 1600 °C: general feature (on the left); HRTEM images showing the degree of crystallinity (inset in detail, on the right); also the EDX result of β–grains illustrated the chemical composition.

Figure 2.6 presents TEM images of the typical rod-like β–Si_3N_4 grains exhibiting tip-body morphology with aspect ratio of ~ 5.7 ± 1.2 (on the left). Moderate degree of crystallinity reported in the HRTEM images (see insets on the right), as evident discontinuance of the stack of planes and presenting of diffuse halo diffraction pattern that indicates poor crystal region characterized by low order [47]. Note the presence of amorphous thin layer on the β–grain surface (~1.28 nm thick for tip, and ~1.07 thick for body). The EDX resulting of β–Si_3N_4 grains shows contamination of aluminum on the tip and zirconium on the body.

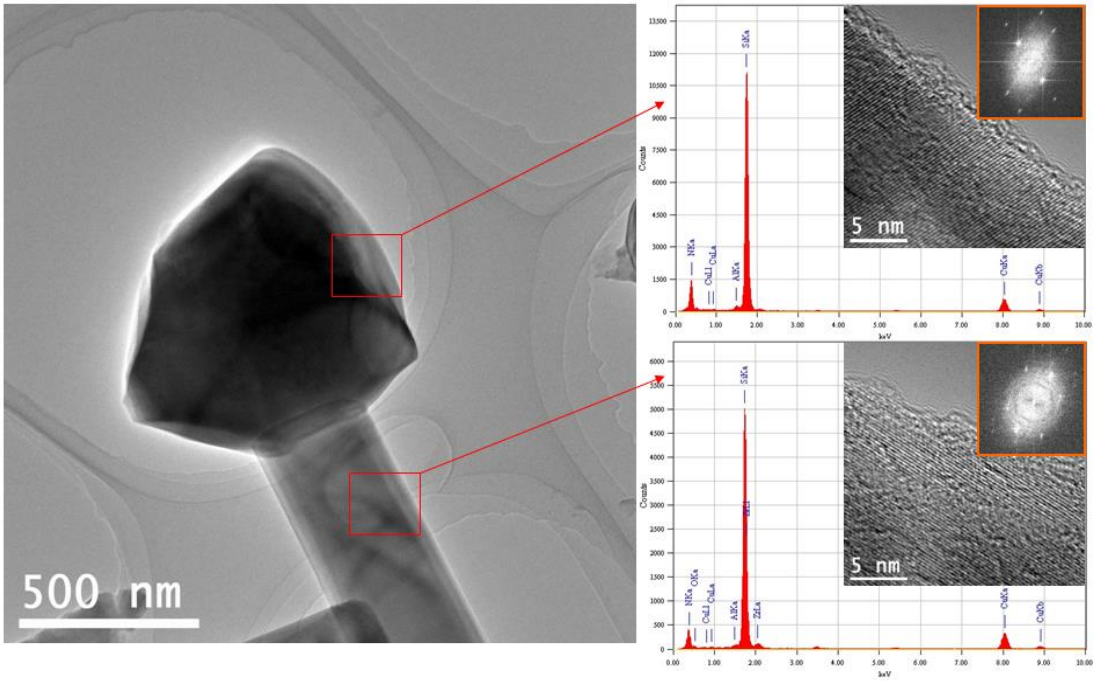

Fig. 2.6. TEM images of the typical rod-like β–Si_3N_4 grains precipitated in the cell walls and struts of decane foams during sintering at 1600 °C: general feature presenting tip-body morphology (on the left); HRTEM images presenting diffuse halo diffraction pattern that indicates scattering from poor crystal region (inset in detail, on the right); also the EDX result of β–grains illustrated the chemical composition.

The influence of the temperature on the morphology of the Si_3N_4 foams emulsified with different alkanes featuring highly interconnected spherical cell morphology is reported in Figure 2.7. Typical rod-like β–Si_3N_4 grains exhibiting aspect ratio between ~9.0 ± 2.0 to ~11.0 ± 5.0 (see Fig 2.7. c and f), and also the presence of residual porosity on cell wall and strut structure (probably due to the interlocking of β–grains), see Table 2.2. Note that when the temperature is increased up to 1700 °C the amount of porosity is maintained almost the same about ~ 74 vol% for octane and 76 vol% for decane foams, respectively. Note that the sintering temperature slightly influences the average cell and window size, around 28.0 ± 5.0 μm and 7.8 ± 1.3 μm, respectively, for octane foams, and around 45.6 ± 4.0 μm and 9.8 ± 1.4 μm, respectively, for decane foams (see Table 2.1).

As reported by Park et al. [48], at higher heat temperature, fine precipitates of β–Si_3N_4 grains and large pores are observed together. The latter formed by the spread of liquid phase

between the surrounding α–Si_3N_4 grains that enable extent of the interfacial area between α–Si_3N_4 particles and the molten resulting in an increased nucleation site of β–Si_3N_4 precipitates.

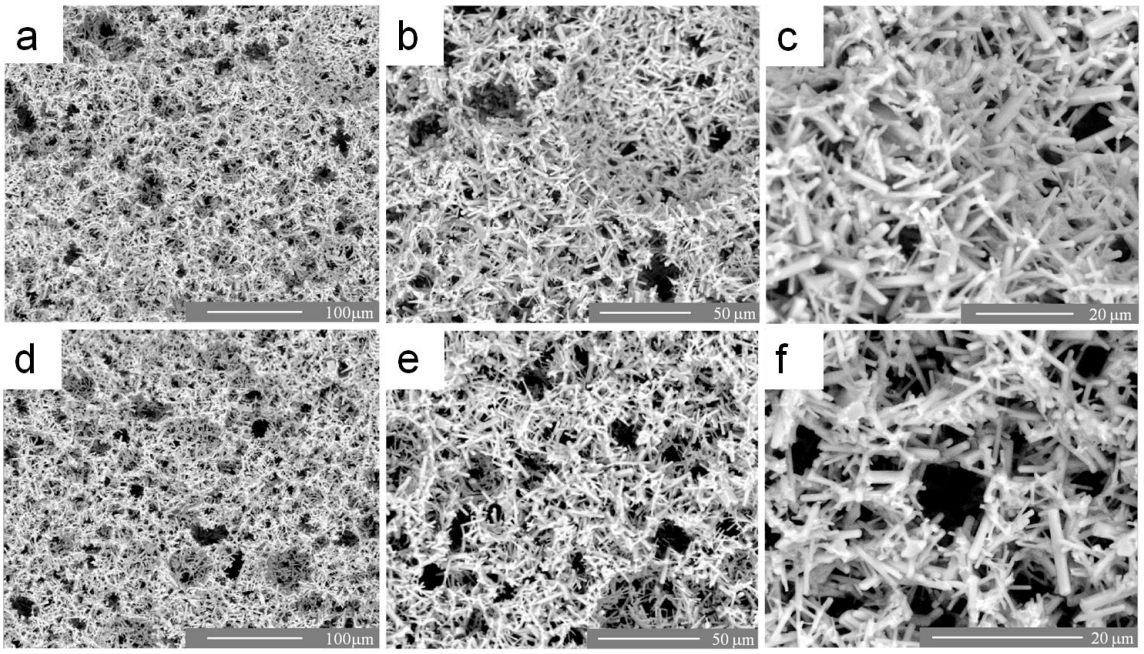

Fig. 2.7. SEM images of the typical rod-like β–Si_3N_4 grains precipitated at cell walls and struts of the foams emulsified with the different alkanes during sintering at 1700 °C: octane foam a) and b) general feature, c) higher magnification; decane foam d) and e) general feature, f) higher magnification (detail of interlocking of the β–grains on cell walls and struts for both alkanes).

Figure 2.8 presents TEM images of the neck formation between α–grains of Si_3N_4 octane foams sintered at 1700 °C. Note that in this system with the increase in the temperature we observed the development of ~98% of β–Si_3N_4 without significant densification. HRTEM images (see inset on the right) reporting high degree of crystallinity into α–Si_3N_4 grains and also presence of amorphous thin layer ~1.0 nm on the α–grain surface. Note the EDX exhibiting yttrium that comes from the initial composition and aluminum as a contamination.

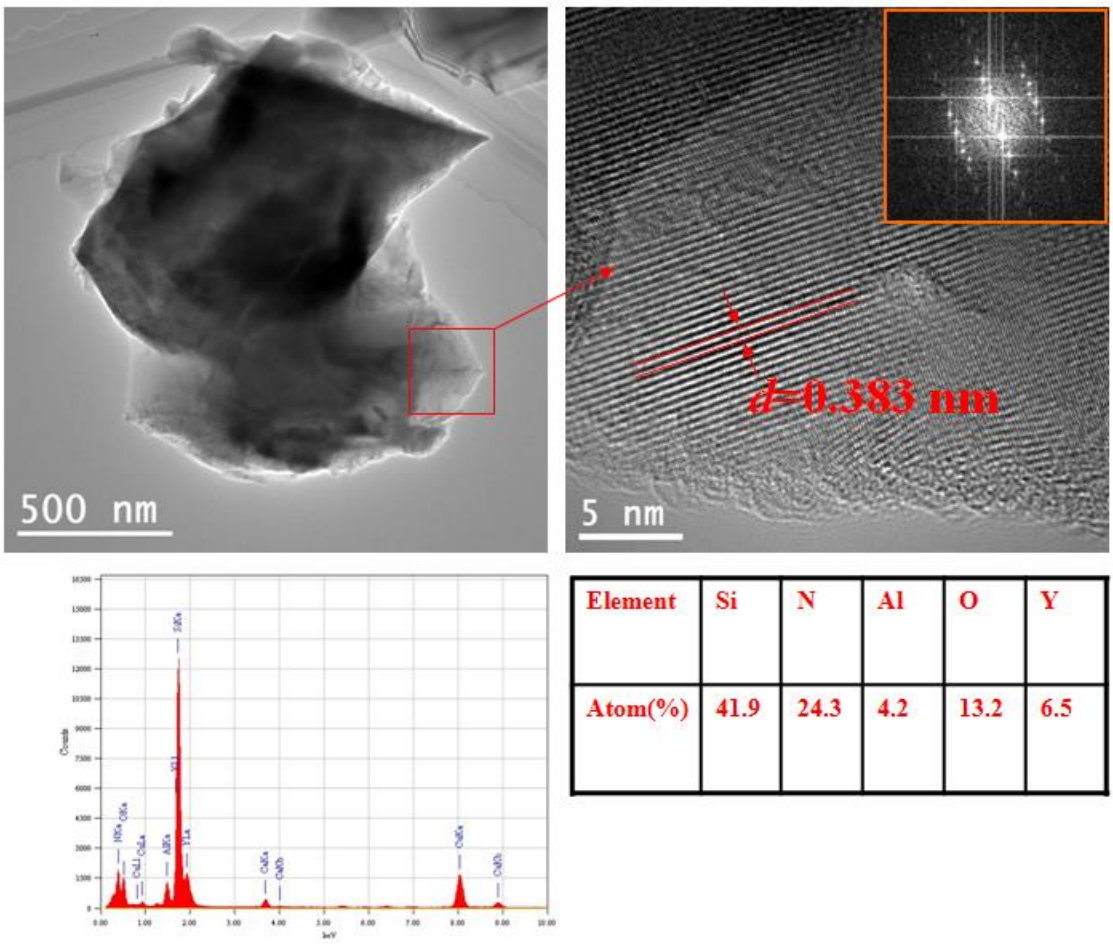

Element	Si	N	Al	O	Y
Atom(%)	41.9	24.3	4.2	13.2	6.5

Fig. 2.8. TEM images of the neck formation between α–Si_3N_4 grains of octane foams sintered at 1700°C: general feature (on the left); HRTEM images reporting detail of degree of crystallinity (on the right), also amorphous thin layer on the grain surface; also the EDX result of α–grains illustrated the chemical composition.

Figure 2.9 presents TEM images of the typical rod-like β–Si_3N_4 grains of Si_3N_4 octane foams sintered at 1700 °C. β–grains exhibiting aspect ratio of ~ 11.0 ± 5.0 (on the left) and high degree of crystallinity reported in the HRTEM images, even if their surface present a thin amorphous coating of less than 1 nm thick (see inset on the right). Note the EDX presenting carbon from the C film and copper from the Cu grid.

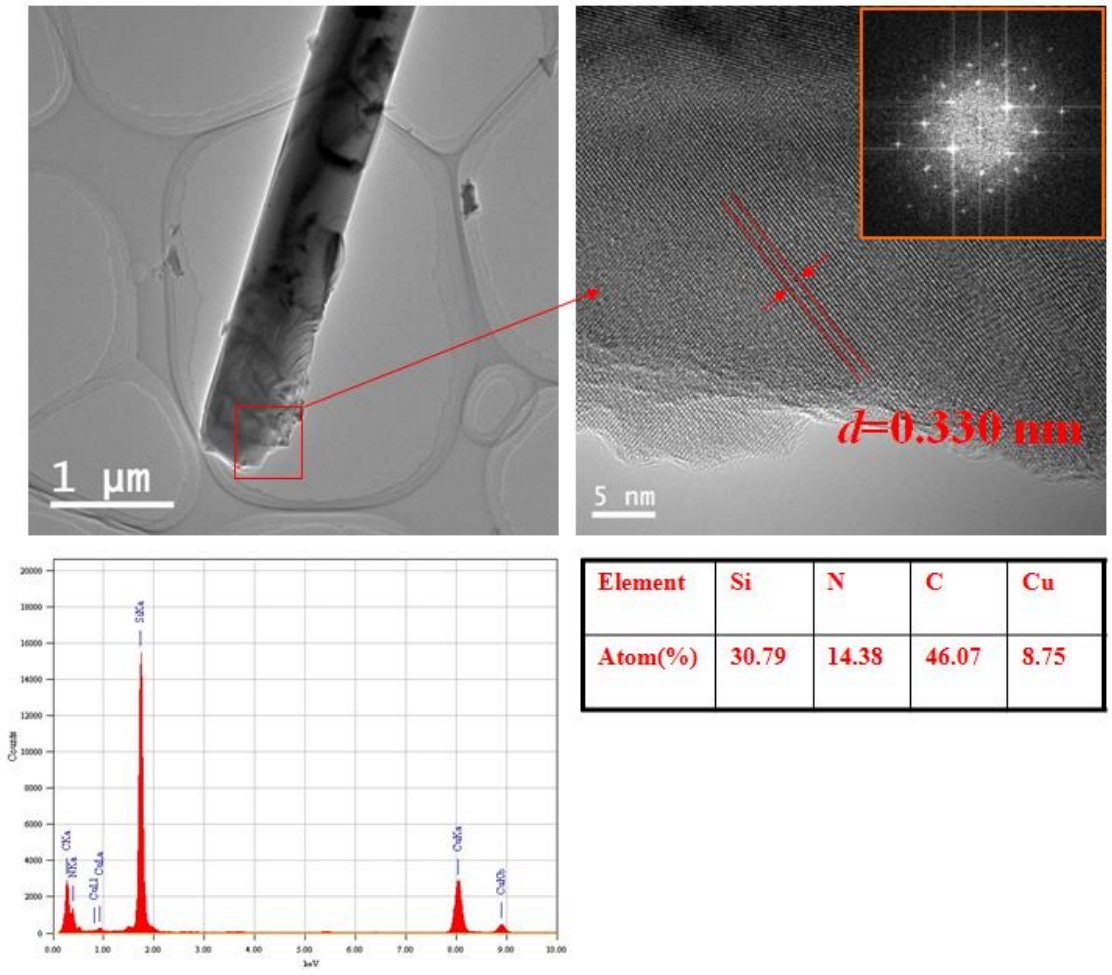

Fig. 2.9. TEM images of the typical rod-like β–Si_3N_4 grains of octane foams sintered at 1700 °C: general feature (on the left); HRTEM images (on the right) reporting detail of degree of crystallinity and presence of amorphous coating on the surface; also the EDX result of β–grains illustrated the chemical composition.

Figure 2.10 presents TEM images of the neck formation between α–grains of Si_3N_4 decane foams during sintering at 1700 °C. Note the development of ~98% of β–Si_3N_4 with little densification. HRTEM images reporting high degree of crystallinity (see inset on the right). Note the presence of amorphous thin layer (~2.3 nm thick) coating the surface of the α–Si_3N_4 grains, as a result of the liquid phase formation during sintering. The EDX shows presence of magnesium that comes from the initial composition and aluminum as a contamination.

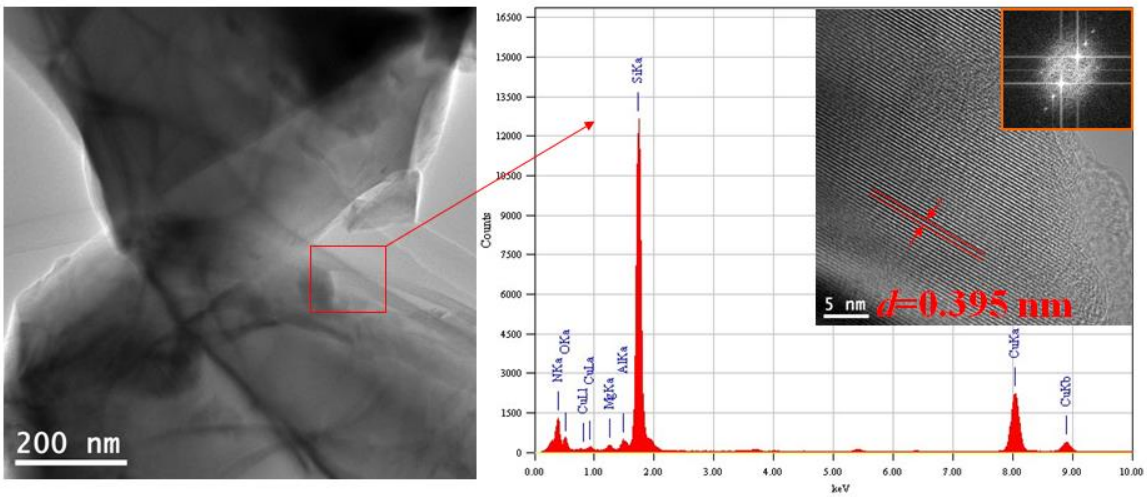

Fig. 2.10. TEM images of the neck formation between α–Si_3N_4 grains of decane foams sintered at 1700 °C: general feature (on the left); HRTEM images reporting detail of degree of crystallinity and presence of amorphous coating on the surface of grains (on the right); also the EDX result of α–grains illustrated the chemical composition.

Figure 2.11 presents TEM images of the typical rod-like β–Si_3N_4 grains of Si_3N_4 decane foams during sintering at 1700 °C. β–grains exhibiting aspect ratio of ~ 9.0 ± 2.0 (on the left) and high degree of crystallinity and presenting an amorphous thin layer (less than ~1.0 nm) on their surface are reported in the HRTEM images (see inset on the right). Note the EDX presenting carbon from the C film and copper from the Cu grid.

According to Park et al., the samples heat treated at temperatures around 1600 °C are more slowly transformed than above 1700 °C. This seems to be resulted from the differences of the dissolution rate of α–Si_3N_4 grains; also the material transport required for the α→β transformation is occurred more easily at elevated temperature. Therefore, the rate of transformation is increased with heat treating temperature which results in elongated β–Si_3N_4 grains [48].

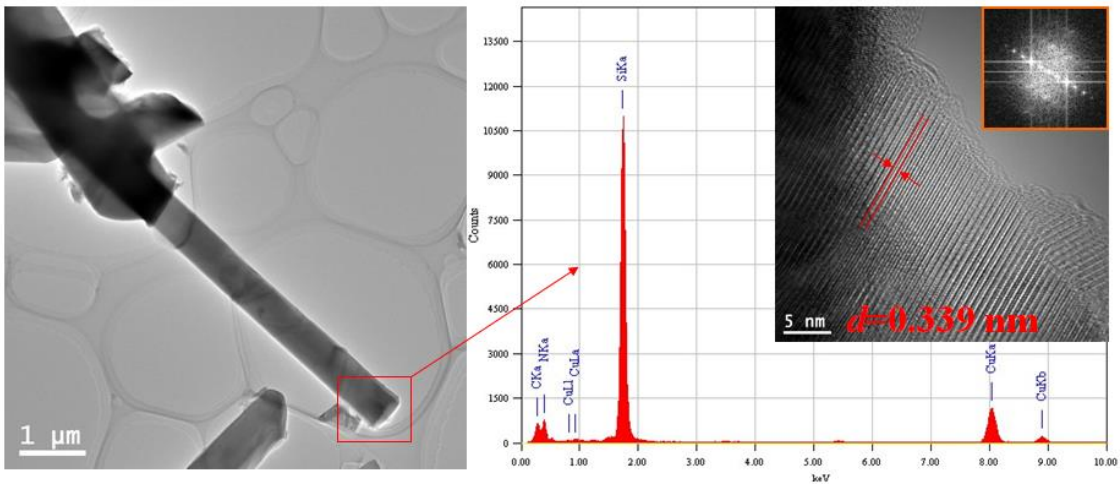

Fig. 2.11. TEM images of the typical rod-like β–Si_3N_4 grains of decane foams sintered at 1700 °C: general feature (on the left); HRTEM images (on the right) reporting detail of degree of crystallinity and presence of amorphous thin layer; also the EDX result of β–grains illustrated the chemical composition.

Compressive strength as a function of total porosity is reported in Figure 2.12 for Si_3N_4 foams emulsified with different alkanes and sintered at 1600 °C. The values increased from ~5 to ~21 MPa for foams produced using octane, when porosity decreased from ~75 to ~71 vol%, and ranged from ~7 to ~20 MPa for foams produced using decane, when porosity decreased from 77 to 71 vol%. The variation in density and strength among samples processed in similar conditions reflects the inhomogeneity deriving from the emulsification process and the effect of an important processing variable such as the evaporation rate of the oil phase, which requires a strict control of the ambient temperature. Nevertheless, the strength values for these samples were higher than those of foams with similar total porosity produced by most other methods, and comparable to those of foams obtained by particle stabilization [43].

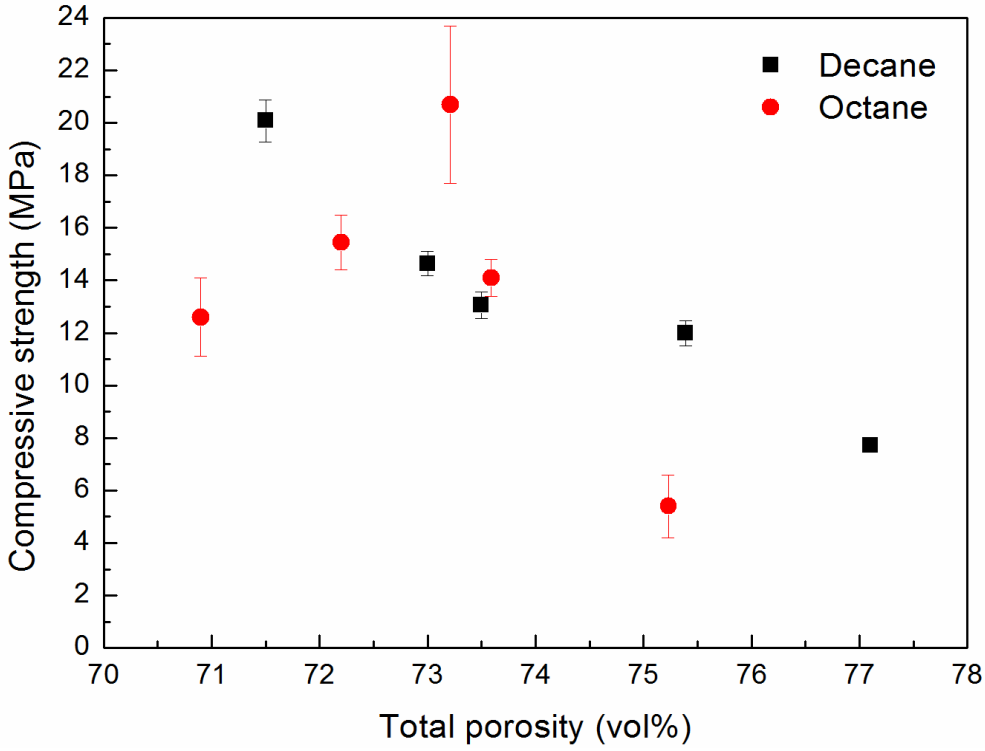

Fig. 2.12. Compression strength of sintered Si_3N_4 foams as function of total porosity.

In order to investigate the influence of temperature on the strength, Figure 2.13 shows a comparison between the compressive strength as a function of total porosity of Si_3N_4 decane foams sintered at different temperatures. It is noteworthy to observe that the Gibson-Asbhy model seems to provide a better fit for most of the data for the produced foams, although the assessment of the specific reason for this behavior would require the analysis of a much larger database, which is outside the scope of this work.

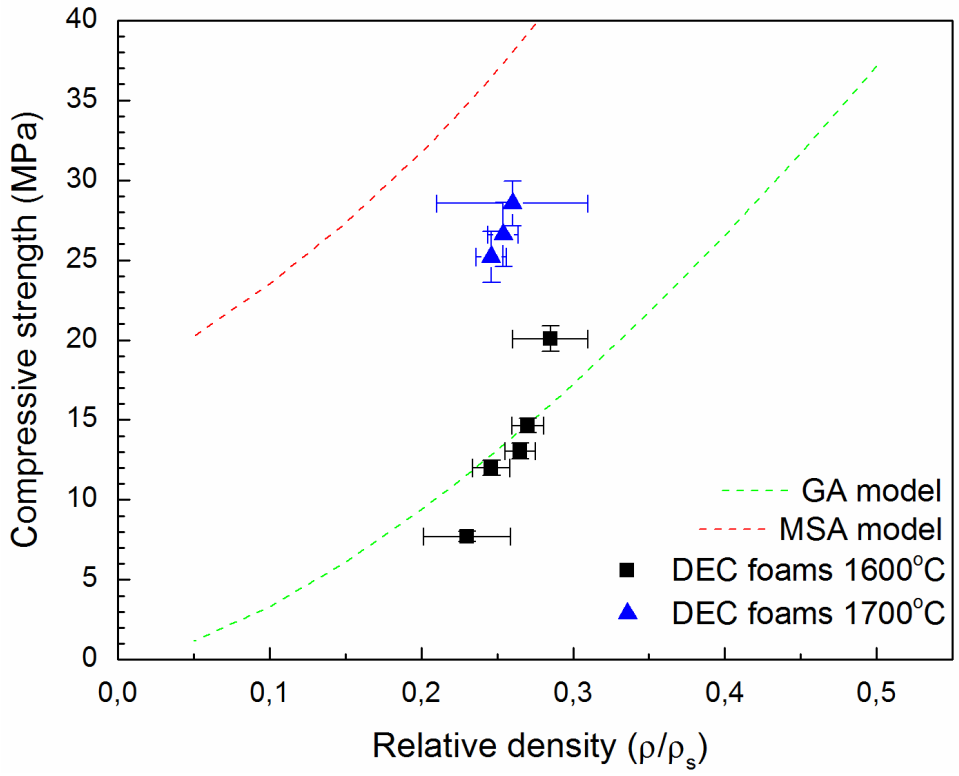

Fig. 2.13. Compression strength of sintered Si_3N_4 decane foams as function of relative density. Comparison between MSA and GA models and experimental data.

As already pointed out, when the temperature increase to 1700 °C, we observe the stimulated development of ~98% β–Si_3N_4 elongated rod-like grains, which are beneficial for strengthening by grain bridging and pullout. High strength values about ~ 28 MPa was obtained for decane foams sintered at high temperature 1700 °C, which indicates that fine-sized, fibrous Si_3N_4 grains favor high strength in porous Si_3N_4 ceramics, differently of large grains, obtained at 1600 °C, when little transformation occurred, and a wide range of strength was observed. Similar behavior was observed by Yang et al., an increasing in the flexural strength as a result of fibrous β–Si_3N_4 [11]. Besides the formation of elongated grains, the increase in strength with increasing temperature could also come from an increased degree of bonding between grains, since with increasing sintering temperature diffusion is enhanced.

However, the occurrence of the large elongated grains does not guarantee the toughening mechanism [40]. For the crack-bridging toughening effect to occur, the reinforcing elongated grains must debond from the small matrix so that the crack tip is deflected along the grain face instead of splitting the elongated grains, while leaving intact elongated grains to bridge the crack [49]. The

interfacial debonding process depends on the chemistry of the grain boundary phase, which is directly determined by the additive composition [50].

Table 2.1. Summary of the physical properties of the Si_3N_4 foams from the emulsification process.

Si_3N_4 foams (700rpm)	***d_{50} Cell size, D*** [a] ***(μm)***	***Cell window size, d (μm)***	***Total Porosity*** [b] ***(vol%)***	***Aspect ratio***	***σ Compressive strength (MPa)***
Un-sintered foams					
70 vol% OCT	36.0 ± 1.4	8.0 ± 1.2	76.8 ± 2.0	-	-
70 vol% DEC	58.3 ± 2.3	13± 2.2	83.1± 1.0	-	-
Conventional Pressureless Sintering 1600 °C, N_2 flow					
70 vol% OCT	31.0 ± 1.1	6.0 ± 0.8	73.6 ± 0.4	4.0 ± 0.6	14.1 ± 0.7
70 vol% DEC	55.0 ± 2.0	8.6 ± 1.2	73.5 ± 0.1	5.0 ± 0.7	13.1 ± 0.5
Conventional Pressureless Sintering 1700 °C, static N_2					
70 vol% OCT	28.0 ± 5.0	7.8 ± 1.3	76.0 ± 0.3	11.0 ± 5.0	24.0 ± 0.1
70 vol% DEC	45.6 ± 4.0	9.8 ± 1.4	74.0 ± 0.1	9.0 ± 2.0	28.5 ± 1.4

[a] Cumulative cell size distribution, d_{50}, measured from SEM images using linear intercept method.

[b] Calculated by assuming that the theoretical density of Si_3N_4 ceramic is 3.2 g cm^{-3}.

According to Díaz et al. [51], although attempts have been made to correlate the semi-empirical equations fitting constants to the experimental data of materials microstructure, criticisms have been made in relation to weaknesses in background theory and as regards the reliability of the actual experimental data. In fact is difficult to relate actual equation parameters to the character of the porosity in terms of MSA and GA models and semi-empirical constants.

Table 2.2. Summary of results for the size of microporosity (in the cell walls and the struts) and cell windows, and for the porosity of Si_3N_4 foams from the emulsification process. Data were obtained from mercury intrusion measurements.

Si_3N_4 Octane foams (700rpm)	***Struts/cell wall average pore size [a] (μm)***	***Cell windows average size [a] (μm)***	***Bulk density (g/cm^3)***	***Total porosity (vol%)***	***Open porosity (vol%)***
Conventional Pressureless Sintering 1600 °C, N_2 flow					
70 vol% OCT	0.7	4.6	0.6320 ± 0.03	80.3	70.9
70 vol% DEC	0.9	6.7	0.5884 ± 0.03	81.6	71.8
Conventional Pressureless Sintering 1700 °C, static N_2					
70 vol% OCT	2.7	6.5	0.7789 ± 0.03	75.7	67.1
70 vol% DEC	2.6	8.9	0.8296 ± 0.04	74.2	70.1

[a] Value selected from the individual peaks of the multimodal pore diameter distribution.

Figure 2.14 shows some typical permeability curves (pressure drop curves (pressure-drop versus air velocity, particularly these samples were tested in air) tested at different temperatures (from ~25 to ~650 ºC) for Si_3N_4 foams emulsified using octane (on the left), and decane (on the high) sintered at 1600 °C. The resistances to flow of the samples slightly differ for different alkanes and exhibit the parabolic trend proposed by Forchheimer Eq. (2.1) was confirmed by the exceptional correlation coefficient (R^2>0.99), rather than the linear relationship between pressure drop and fluid velocity stated by Darcy's law. The intensity of the quadratic term clearly increases at higher velocities (>1.0 m/s), showing that the inertial term is not irrelevant in permeability analysis. Furthermore, with the increasing in air temperature shifted the pressure drop to higher values and this behavior is related to changes in both fluid and medium properties [35,52,53]. The permeability constants k_1 and k_2 were obtained by fitting the pressure drop curves with Forchheimer's equation (2.1), and are reported in Table 2.3.

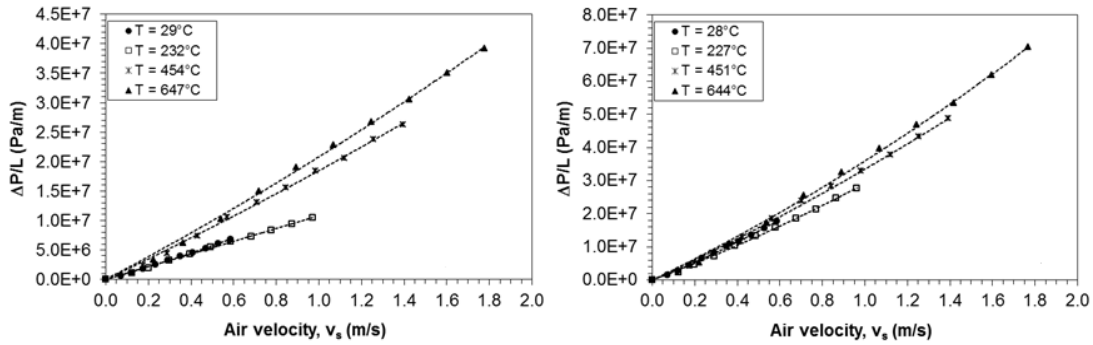

Fig. 2.14. Pressure drop curves obtained at different testing temperatures for Si_3N_4 foams emulsified using octane (on the left), and decane (on the high) sintered at 1600 °C.

With the increasing of the sintering temperature to 1700 °C, the morphology of the Si_3N_4 foams emulsified with the different alkanes present typical rod-like β–Si_3N_4 grains, as already discussed. We also investigate the influence of this morphology on the permeability behavior. Figure 2.15 presents the pressure drop curves for Si_3N_4 foams emulsified using octane (on the left), and decane (on the high) tested in argon at different temperatures (from ~25 to ~650 °C). Permeability constants k_1 and k_2 were obtained by fitting the experimental data showed in Fig. 2.15, calculated from Eq. (2.1), using the least-squares method, see Table 2.3. Is interesting to note that these values slightly increased with the increasing of the sintering temperature, it can be related to the interlocking of β–grains (residual porosity on cell wall and strut structure, see Table 2.2).

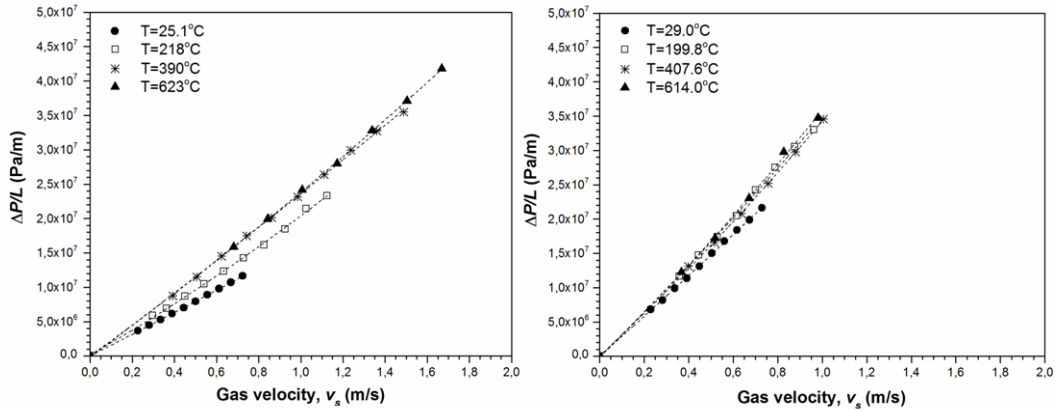

Fig. 2.15. Pressure drop curves obtained at different testing temperatures for Si_3N_4 foams emulsified using octane (on the left), and decane (on the high) sintered at 1700 °C.

In addition, experimental values of permeability constants k_1 and k_2 were then roughly used to compute the average pore size, using Ergun-like equations, originally developed for granular beds (spheres, cylinders, tablets, nodules, round sand, and crushed materials), as a function of the volumetric void fraction, i.e., porosity ε, and the equivalent particle size d_p. However, for porous media in which the solid matrix is continuous and the constitutive particles/grains/fibres are not individually recognizable, similar relationships can be derived by replacing d_p by the average pore or cell size d_c. [54]. Therefore, Ergun equations for predicting average cell sizes could be expressed as [36]:

$$k_1 = \frac{2.25}{150} \varepsilon \, d_c^2 \tag{2.2}$$

$$k_2 = \frac{1.5}{1.75} \varepsilon^2 d_c^2 \tag{2.3}$$

Thus, the average cell size d_c was estimated using the known the experimental value of k_1 (at R.T.) and ε, for Si_3N_4 foams emulsified using octane and decane sintered at different temperatures, as shown in Table 2.3. Note that these values are in accordance with those evaluated by mercury porosimetry for cell windows size. According to Biasetto et al., the best approximation for permeability constants k_1 and k_2 of microcellular ceramic foams was achieved for d_c based on cell size rather than on window cell size [36].

Table 2.3. Summary of the constants k_1 and k_2 obtained by fitting the pressure drop curves with Forchheimer's equation for the Si_3N_4 foams from the emulsification process.

Si_3N_4 foams from emulsion				
Octane foam 1600 °C	***T °C***	***$k_1(m^2)$***	***$k_2(m)$***	***d_c (μm)***
	R.T	1.88E-12	3.85E-07	12.2 ± 0.7
	600 °C	2.15E-12	6.80E-08	-
Octane foam 1700 °C	R.T	1.44E-12	3.54E-06	12.7 ± 0.8
	600 °C	2.05E-12	3.89E-07	-
Decane foam 1600 °C	***T °C***	***$k_1(m^2)$***	***$k_2(m)$***	***d_c (μm)***
	R.T	5.72E-12	1.00E-06	16.4 ± 2.8
	600 °C	3.24E-12	2.57E-07	-
Decane foam 1700 °C	R.T	7.80E-13	1.82E-06	10.6 ± 1.4
	600 °C	1.63E-12	1.30E-07	-

A comprehensive map that correlates the values of viscous and inertial constants and classifies a variety of porous media according to their permeability level and type of application was elaborated by Innocentini et al. [55]. Figure 2.16 shows such a map version that includes all values of k_1 and k_2 obtained in this work. It can be observed that the tested samples are in the range of magnitude typical for bodies produced by gelcasting of foams. An important aspect highlighted is that despite all the different processing techniques, fluids, and flow conditions used to assess permeability data, it is remarkable that a clear correlation between both permeability parameters

could link porous media of totally different structural features.

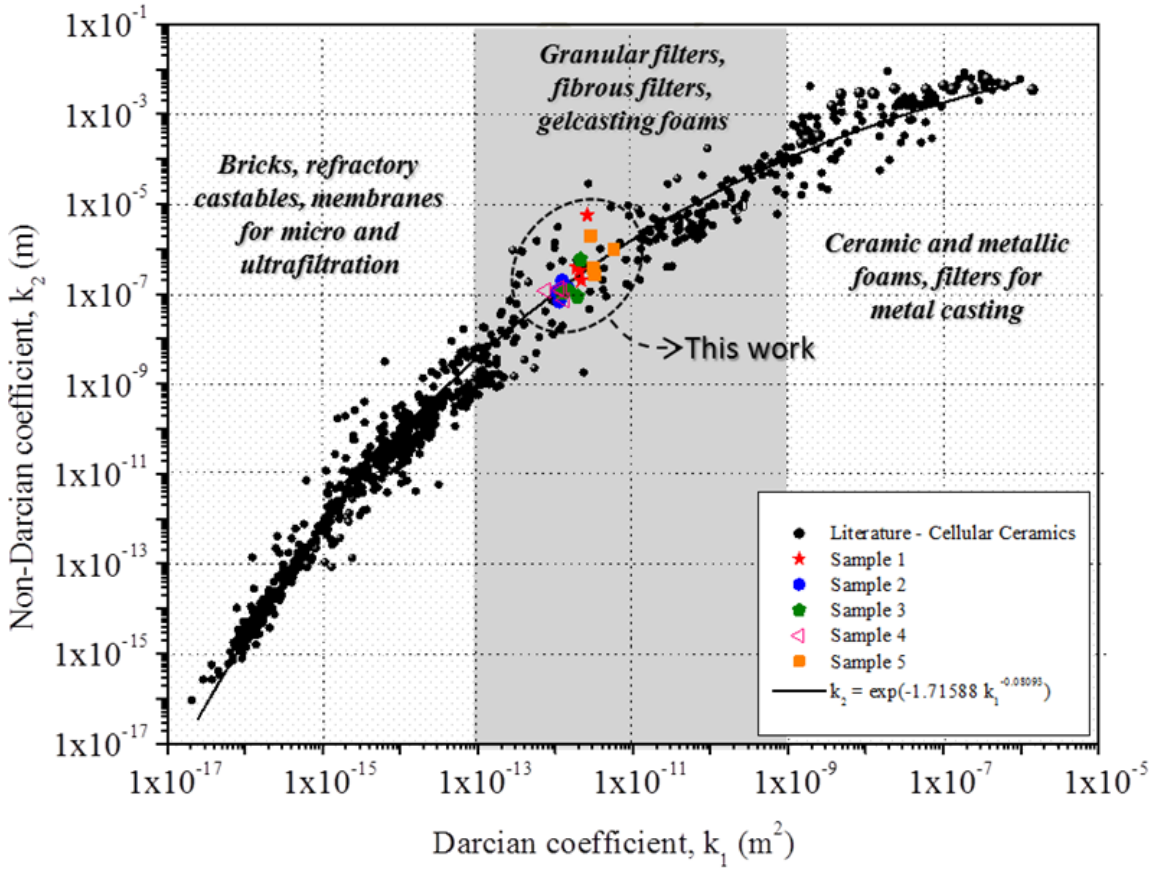

Fig. 2.16. Location of permeability data for Si_3N_4 foams emulsified using octane and decane sintered at different temperatures in a comprehensive data map available in the literature [55].

2.4 Conclusions

Highly interconnected Si_3N_4 foams emulsified using alkanes were successfully produced. Total porosity higher than 70 vol% was achieved by incorporation of high amount of alkanes. Different alkanes (octane and decane) were used, but we observe slightly differences in cell size, and strength at moderate sintering temperature (1600 °C). The degree of the strut densification as well neck formation was limited, due to the low sintering temperature, resulting in strength values around ~5 to ~20 MPa. An increase in the final sintering temperature (up to 1700 °C) enable the

development of elongated β–grains precipitated at cell walls and struts of foams, which strongly influence the strength that increased up to ~28 MPa, at 74 vol% of porosity).

Permeability evaluation shows that Si_3N_4 foams from emulsions are in the range of gelcasting foams and are suitable for filtering application.

References

[1] Scheffler M, Colombo P. Cellular ceramics: structure, manufacturing, properties and application. Weinheim: Wiley-VCH; 2005.

[2] Studart AR, Gonzenbach UT, Tervoort E, Gauckler LJ. Processing routes to macroporous ceramics - A review. *J Am Ceram Soc* 2006;**89**(6):1771–89.

[3] Gauckler LJ, Waeber MM, Conti C, Jacobduliere M. Ceramic foam for molten-metal filtration. *J Met* 1985;**37**(9):47–50.

[4] Chen QZ, Rezwan K, Armitage D, Nazhat SN, Boccaccini AR. The surface functionalization of 45S5 Bioglass-based glass-ceramic scaffolds and its impact on bioactivity. *J Mater Sci Mater Med* 2006;**17**(11):979–87.

[5] Chen QZ, Thompson ID, Boccaccini AR. 45S5 Bioglasss - derived glass-ceramic scaffolds for bone tissue engineering. *Biomater* 2006;**27**(11):2414–25.

[6] Colombo P. Conventional and novel processing methods for cellular ceramics. *Phil Trans R Soc A* 2006;**364**(1838):109–24.

[7] Riley FL. Silicon nitride and related materials. *J Am Ceram Soc* 2000;**83**(2):245–65.

[8] Moreno R, Salomoni A, Stamenkovic I, Castanho SM. Colloidal filtration of silicon nitride aqueous slips, part II: slip casting and pressure casting performance. *J Eur Ceram Soc* 1999;**19**(1):49–59.

[9] Yang JF, Beppu Y, Zhang GJ, Ohji T, Kanzaki S. Synthesis and Properties of Porous Single-Phase β'–SiAlON Ceramics. *J Am Ceram Soc* 2002;**85**(7):1879–81.

[10] Petzow G, Hermann M. Silicon nitride ceramics. In: Jansen M, editor. High performance non-oxide ceramics II. Berlin: Springer Berlin Heidelberg; 2002. p. 47–167.

[11] Yang JF, Deng ZY, Ohji T. Fabrication and characterisation of porous silicon nitride ceramics using Yb_2O_3 as sintering additive. *J Eur Ceram Soc* 2003;**23**(2):371–78.

[12] Kondo N, Inagaki Y, Suzuki Y, Ohji T. Fabrication of porous anisotropic silicon nitride by using partial sinter-forging technique. *Mater Sci Eng A* 2002;**335**(1-2):26–31.

[13] Inagaki Y, Kondo N, Ohji T. High performance porous silicon nitrides. *J Eur Ceram Soc* 2002;**22**(14-15):2489–94.

[14] Ziegler G, Heinrich J, Wötting G. Relationships between processing, microstructure and properties of dense and reaction-bonded silicon nitride. *J Mater Sci* 1987;**22**(9):3041–86.

[15] Moulson AJ. Reaction-bonded silicon nitride: its formation and properties. *J Mater Sci* 1979;**14**(5):1017–51.

[16] Díaz A, Hampshire S. Characterisation of porous silicon nitride materials produced with starch. *J Eur Ceram Soc* 2004;**24**(2):413–19.

[17] Peng HX, Fan Z, Evans JRG, Busfield JJC. Microstructure of ceramic foams. *J Eur Ceram Soc* 2000;**20**(7):807–13.

[18] Huang Y, Ma L, Tang Q, Yang J, Xie Z, Xu X. Surface oxidation to improve water-based gelcasting of silicon nitride. *J Mater Sci* 2000;**35**(14):3519–24.

[19] Nangrejo MR, Bao X, Edirisinghe MJ. Preparation of silicon carbide-silicon nitride composite foams from pre-ceramic polymers. *J Eur Ceram Soc* 2000;**20**(11):1777–85.

[20] Adler J. Ceramic diesel particulate filters. *Int J Appl Ceram Technol* 2005;**2**(6):429–39.

[21] Miyakawa N, Shinohara N, Watanabe T. Method for producing a silicon nitride filter. US Patent 7 368 076; May 6 2008.

[22] Ohji T, Fukushima M. Macro-porous ceramics: processing and properties. *Int Mater Rev* 2012;**57**(2):115–31.

[23] Gonzenbach UT, Studart AR, Tervoort E, Gauckler LJ. Stabilization of foams with inorganic colloidal particles. *Langmuir* 2006;**22**(26):10983–88.

[24] Barg S, Moraes EG, Koch D, Grathwohl G. New cellular ceramics from high alkane phase emulsified suspensions (HAPES). *J Eur Ceram Soc* 2009;**29**(12):2439–46.

[25] Barg S, Koch D, Grathwohl G. Processing and properties of graded ceramic filters. *J Am Ceram Soc* 2009;**92**(12):2854–60.

[26] Barg S, Innocentini MDM, Meloni RV, Chacon WS, Wang H, Koch D, et al. Physical and high-temperature permeation features of double-layered cellular filtering membranes prepared via freeze casting of emulsified powder suspensions. *J Membr Sci* 2011;**383**(1):35–43.

[27] Schmitt V, Leal-Calderon F, Bibette J. Preparation of monodisperse particles and emulsions by controlled shear. In: Antonietti M, editor. Colloid chemistry II. Berlin: Springer Berlin Heidelberg; 2003. p. 195–215.

[28] Barg S, Soltmann C, Andrade M, Koch D, Grathwohl G. Cellular ceramics by direct foaming of emulsified ceramic powder suspensions. *J Am Ceram Soc* 2008;**91**(9):2823–29.

[29] Reymond JP, Kolenda F. Estimation of the point of zero charge of simple and mixed oxides by mass titration. *Powder Technol* 1999;**103**(1):30–36.

[30] Ling G, Yang H. Pressureless sintering of silicon nitride with magnesia and yttria. *Mater Chem Phys* 2005;**90**(1):31–34.

[31] Nagel A, Petzow G, Greil P. Rheology of aqueous silicon nitride suspensions. *J Eur Ceram Soc* 1989;**5**(6):371–78.

[32] Oliveira MILL, Chen K, Ferreira JMF. Influence of powder pre-treatments on dispersion ability of aqueous silicon nitride-based suspensions. *J Eur Ceram Soc* 2001;**21**(13):2413–21.

[33] Blanchard CR, Schwab ST. X-ray diffraction analysis of the pyrolytic conversion of perhydropolysilazane into silicon nitride. *J Am Ceram Soc* 1994;**77**(7):1729–39.

[34] Ortega FS, Sepulveda P, Innocentini MDM, Pandolfelli VC. Surfactants: a necessity for producing porous ceramics. *Am Ceram Soc Bull* 2001;**80**(4): 37–42.

[35] Innocentini MDM, Faleiros RK, Pisani JR, Thijs I, Luyten J, Mullens S. Permeability of porous gelcast scaffolds for bone tissue engineering. *J Porous Mater* 2010;**17**(5):615–27.

[36] Biasetto L, Colombo P, Innocentini MDM, Mullens S. Gas permeability of microcellular ceramic foams. *Ind Eng Chem Res* 2007;**46**(10):3366–72.

[37] Innocentini MDM, Rizzi JAC, Nascimento LA, Pandolfelli VC. The pressure-decay technique for air permeability evaluation of dense refractory ceramics. *Cem Concr Res* 2004;**34**(2):293–98.

[38] Hampshire S, Jack KH. Densification and transformation mechanisms in nitrogen ceramics. In: Riley FL, editor. Progress in Nitrogen Ceramics. Lancaster: Martinus Nijhoff publ;1983. 225–30.

[39] Alper AM. Phase diagrams in advanced ceramics. London: Acad Press Ltd; 1995.

[40] Pyzik A, Beaman D. Microstructure and properties of self-reinforced silicon nitride. *J Am Ceram Soc* 1993;**76**(11):2737–44.

[41] Wang CM, Pan X, Rühle M, Riley FL, Mitomo M. Silicon nitride crystal structure and observations of lattice defects. *J Mater Sci* 1996;**31**(20):5281–98.

[42] Schramm, Laurier L. Emulsions, foams, and suspensions: fundamentals and applications. Weinheim: Wiley-VCH; 2005.

[43] Yu J, Yang J, Li H, Xi X, Huang Y. Study of particle-stabilized Si_3N_4 ceramic foams. *Mater Lett* 2011;**65**(12):1801–04.

[44] Barg S. Cellular ceramics via alkane phase emulsified powder suspensions [Ph.D. thesis] Bremen: University of Bremen; 2010.

[45] Karbstein H, Schubert H. Developments in the continuous mechanical production of oil-in-water macro-emulsions. *Chem Eng Process: Process Intensif* 1995;**34**(3):205–11.

[46] Jafari SM, Assadpoor E, He Y, Bhandari B. Re-coalescence of emulsion droplets during high-energy emulsification. *Food Hydrocoll* 2008; **22**(7):1191–202.

[47] Clarke DR. Intergranular phases in polycrystalline ceramics. In: Dufour LC, et al., editors. Surfaces and interfaces of ceramic materials. Dordrecht: Kluwer Academic publ; 1989. 57–79.

[48] Park JY, Kim CH. The α–to β–Si_3N_4 transformation in the presence of liquid silicon. *J Mater Sci* 1988;**23**(9):3049–54.

[49] Becher P F. Microstructural design of toughened ceramics. *J Am Ceram Soc* 1991;**74**(2):255–69.

[50] Zhu X, Sakka Y. Textured silicon nitride: processing and anisotropic properties. *Sci Technol Adv Mater* 2008;**9**(3):033001.

[51] Díaz A, Hampshire S, Yang JF, Ohji T, Kanzaki S. Comparison of mechanical properties of silicon nitrides with controlled porosities produced by different fabrication routes. *J Am Ceram Soc* 2005;**88**(3):698–706.

[52] Innocentini MDM, Salvini VR, Pandolfelli VC, Coury JR. Assessment of Forchheimer's equation to predict the permeability of ceramic foams. *J Am Ceram Soc* 1999;**82**(7):1945–48.

[53] De Sousa E, Rambo CR, Hotza D, Oliveira AP, Fey T, Greil P. Microstructure and properties of LZSA glass-ceramic foams. *Mater Sci Eng A* 2008;**476**(1):89–97.

[54] Simão L, Montedo ORK, Paula MMDS, Silva LD, Caldato RF, Innocentini MDM. Structural and fluid dynamic characterization of calcium carbonate-based porous ceramics. *Mater Res* 2013;**16**(6):1439–48.

[55] Innocentini MDM, Sepulveda P, Ortega FS. Permeability. In: Scheffler M, Colombo P, editors. Cellular ceramics: structure, manufacturing, properties and applications. Weinheim: Wiley-VCH; 2005. 313–41.

3. Silicon nitride foams from emulsions sintered by rapid intense thermal radiation

E. G. de Moraes, D. Li, P. Colombo and Z. Shen, "Silicon nitride foams from emulsions sintered by rapid intense thermal radiation", manuscript submitted.

3.1. Introduction

Ceramics with a cellular structure and containing designed interconnected porosity above 60 vol% find applications particularly where the transport of fluids is required, e.g. molten metal and exhaust particulate filters at high temperature, gas-burner systems, catalyst support and in energy-related industries [1–6]. These porous components exhibit a special combination of properties such as light weight, high temperature stability and permeability to fluids that cannot normally be reached by conventional dense materials or materials with a non-designed porosity [7].

Silicon nitride (Si_3N_4) is one of the most widely used ceramics in many engineering applications due to its outstanding thermo-mechanical properties, such as flexural strength and Young's modulus around 900 MPa and 310 GPa, respectively, fracture toughness between 3 to 12 $MPa \cdot m^{1/2}$ [8], and strain-to-failure around 3×10^{-3} [9,10]. Its excellent thermal shock resistance can be attributed to the combination of a low thermal expansion coefficient, medium elastic constant, and moderate thermal conductivity [8,11,12]. However, the high cost of production (sintering is generally assisted by pressure), due to the highly covalent bonding between silicon and nitrogen atoms and very slow solid-state diffusion [13], limits significantly the use of silicon nitride-based ceramics to specialized, high value applications. The additions of sintering additives, which are usually metal oxides that form a low-melting-point eutectic liquid with the oxide surface layers of the silicon nitride powder, improve sintering activity considerably and promote high densities without the use of pressure during sintering [14,15]. The development of more economical processes for the production of silicon nitride component in structural applications, with proper process control and uniformity in the properties of the final product, is a challenge from a technological point of view [16].

Various processing methods for the production of highly porous Si_3N_4, such as partial sintering [17,18], reaction sintering [19,20], the use of sacrificial templates using starch consolidation [21], direct foaming [22], gelcasting [23] and preceramic polymers [24], have been proposed. Recently, emulsions have been used as efficient intermediates in the production of porous

materials via direct foaming processes [2,25,26]. They consist of two immiscible fluids, one being dispersed in the other, and are thermodynamically unstable due to their large oil-water interfacial area and thus high overall free energy. Therefore, surface active agents (e.g. surfactants or proteins) are used to reduce the free energy of the system [27,28]. The objective of the present work is to develop cellular silicon nitride ceramics with tailored porosity by using an emulsification process that enables the fabrication of components possessing a well interconnected (open) cell morphology and small, uniform cell sizes [29] and improved mechanical properties by a novel processing approach (rapid pressureless sintering by intense thermal radiation).

3.2. Experimental procedure

Silicon nitride powder (grain size d_{50} = 0.6 μm, purity ~96 wt%, main impurity Fe, oxygen content 7.4 ± 0.08 wt%, α phase ~91.5%, Yantai Tomley Hi-tech Ind.&Tra. Co., Ltd, Yantai, Shandong, China) was used as raw material in this study. The equilibrium pH_{iep} 8.27 ± 0.01 of the powder was measured after 24h aging in water, following the procedure reported in Ref. [30]. High purity Y_2O_3 (d_{50} = 50 nm, Inframat Advanced Materials L.L.C., Manchester, New Hampshire, USA), and MgO (d_{50} = 4.6 μm, Bitossi Ceramiche S.R.L., Montelupo Fiorentino, Firenze, Italy), were used as sintering additives; the label 5YM was used to denote specimens containing 5 wt% Y_2O_3 and 5 wt% MgO, and the amount of sintering aids was inferred from the literature [13]. The powder mixture was wet-milled in ethanol for 4 h, using silicon nitride cylinders and planetary velocity of 300 rpm. The slurry was dried and sieved through a 300 μm screen. The powder mixture was treated in air at 600 °C for 2h, in order to form a silica layer on the particle surfaces to improve their aqueous dispersibility and, consequently decrease the viscosity of the suspension [31]. 1 wt% polyacrylic acid (PAA, Sigma-Aldrich Sweden AB, Stockholm, Sweden) was used as dispersing agent to stabilize the suspensions. 0.22 vol% polysorbate (Tween 80, VWR International, Bedfordshire, UK) was used as nonionic surfactant and consequently foam stabilizer. Water-based Si_3N_4 slurries with 35 vol% of solids and containing PAA were prepared by ball milling for 2 hours at 200 rpm. Afterwards, the emulsification process took place by addition of 50~70 vol% alkane phase (octane, C_8H_{18}, Sigma-Aldrich Sweden AB, Stockholm, Sweden) and subsequently the suspension was stirred at 700 or 1000 rpm for 3 minutes. Then, the emulsions were poured in a Teflon mold and dried at ambient air for approximately 24h.

Rapid pressureless sintering was conducted in a modified SPS set-up (Dr. Sinter 2050, Sumitomo Coal Mining Co., Tokyo, Japan) under vacuum. The green foams were loaded in a

covered cylindrical graphite crucible with an inner diameter of 50 mm and outer diameter of 70 mm. The samples were protected by a Si_3N_4 powder bed and isolated by graphite felts. Two sintering regimes, namely PLSPS-1 and PLSPS-2, were set as follows: the temperature was automatically raised to 600 °C over a period of 5 min, and from there onwards it was monitored and regulated by an optical pyrometer focused on the wall centrally inside the crucible through a hole of ~5 mm in diameter. For PLSPS-1, in the first step the samples were heated to 1500 °C with a heating rate of 50 °C·min^{-1} and maintained for 10 min, then heated to 1600 °C at 50 °C·min^{-1} and held for 3 min. Same steps and temperatures were used for PLSPS-2, differing only for the heating rate and dwell time, which were instead 100 °C·min^{-1} and 5 min for the first step, respectively. More details about this rapid sintering procedure can be found elsewhere (see Ref. [32]).

The bulk density and the total porosity were calculated from the weight-to-volume ratio of the samples, while the open porosity was determined using a mercury intrusion porosimetry (Micromeritics AutoPore III 9410, Norcross, Georgia, USA). The surface tension and the contact angle of the mercury were set to 0.485 N·m^{-1} and 130°, respectively. The crystalline phases were determined on powdered samples by X-ray diffraction (XRD, X'pert PRO MPD diffractometer, PANalytical, Almelo, Netherlands), using CuKα radiation λ= 1.542 Å, at 40 kV and 40 mA. The 2θ range was varied from 10° to 90° with a step size of 0.05° and a step time of 2 s. The data were analyzed utilizing the ICSD database, and the weight fractions of the α– and β–Si_3N_4 crystalline phases were evaluated by the method described in Ref. [33]. The microstructure of the Si_3N_4 based foams was characterized by a field emission scanning electron microscope (FE-SEM, JSM-7000F, JEOL, Tokyo, Japan) and a Schottky-type field emission transmission electron microscope (TEM, JEM-2100F, JEOL, Tokyo, Japan) operated at 200 kV, equipped with an energy-dispersive X-ray spectroscopy (EDX) detector. Electron diffraction (ED) data were collected using a LaB6 based transmission electron microscope (TEM, JEM-2100, JEOL Ltd, Tokyo, Japan) at 200 kV. For TEM study, the sample was crushed into powder and dispersed in ethanol. The average cell and cell window sizes were obtained from SEM images using the linear intercept method according to ASTM E112-12 (diagonal opposite directions), using an image analysis program (Axio Vision LE). When the cells are spherical and uniformly distributed, according to ASTM D3576-98, the relationship between the average measured chord length t and the average sphere diameter D is: D = t·1.623.

The mechanical behavior of the Si_3N_4 based foams was determined by uniaxial compressive strength tests performed using a hydraulic mechanical testing machine (1121 UTM, Instron, Norwood, MA, USA), according to ASTM C133-97 standard. The cross-head speed was 1.0

mm/min and the compressive load cell was 5 kN. Specimens with a nominal size of 10 mm × 10 mm × 10 mm, cut from larger bodies, were tested for each sample. Each data point represents the average value of five individual tests.

3.3. Results and discussion

Influence of sintering additives

The X-ray diffraction patterns of the as prepared powder mixture and rapid sintered Si_3N_4 foams (PLSPS-1 sintering regime) are reported in Figure 3.1. The main phase was α–Si_3N_4 for both samples, while an increase of ~27% in the β–phase was observed after rapid sintering; the relative amounts were estimated on the basis of the ratio of the intensities of the (210) peak for both phases (located at $2\theta \sim 35.42°$ for the α–phase and at $2\theta \sim 36.12°$ for the β–phase), using a normalizing factor, *L*, to correct the peak intensities from errors due to extinction and preferred orientations [33]. The increase of the β–phase after sintering can be explained by the phase transformation α– to β– that occurs above 1600 °C, with the use of Y_2O_3 and MgO as sintering aids in the presence of a liquid phase through a solution-reprecipitation mechanism [34]. The peaks relative to the sintering aids disappeared almost completely after heating because of their incorporation into an amorphous intergranular phase, which distributed homogeneously as a liquid throughout the entire grain boundaries during sintering, due to the modification of the anisotropic solid-liquid interfacial energies at the grain boundaries [35]. The MgO-containing low-viscosity glass migrates to the boundaries, suppressing abnormal grain growth and also creates a pathway for crack damping at nanoscale [36]. The diffusion through the highly viscous liquid is relatively slow, enhancing rapid solution-precipitation and the α→β transformation that starts to occurs in the contact areas without significant material transport and hence with little densification [37].

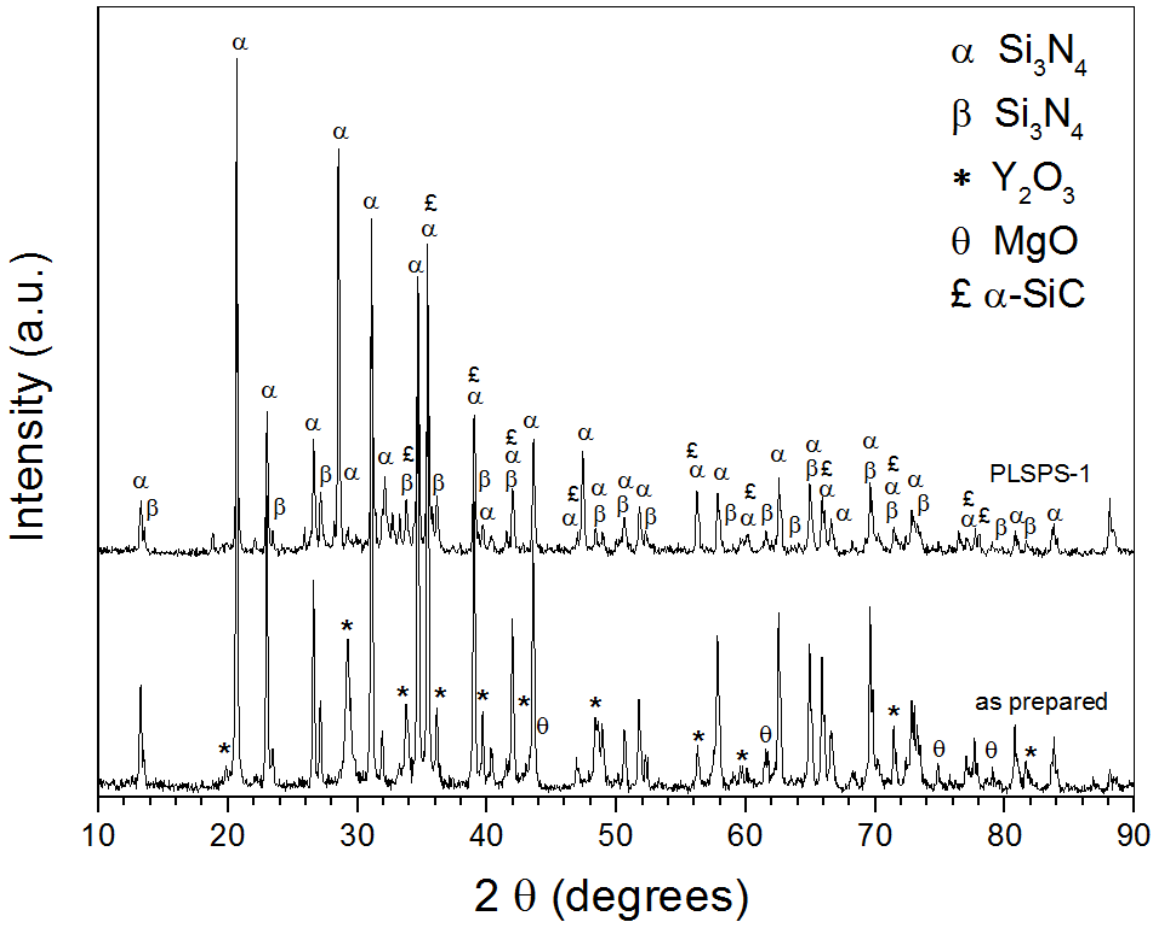

Fig 3.1. XRD patterns for the as-prepared and as-sintered Si_3N_4 foams (PLSPS-1 sintering regime) containing 5 wt% Y_2O_3 and 5 wt% MgO. (ICSD α–Si_3N_4 # 041-0360, β–Si_3N_4 # 033-1160, α–SiC # 049-1428).

Note the evidence in the diffraction patterns of the presence of α–SiC coexisting with the α– and β–Si_3N_4 phases, probably due to the composition of the nanowires (NWs) that formed during processing (see details later).

Influence of octane concentration and stirring velocity

The morphology of the Si_3N_4 sintered foams emulsified with 50 or 70 vol% of octane (700 rpm, PLSPS-1 sintering regime) is shown in Figure 3.2. Typical fracture surfaces are shown in (a) to (c), for moderate octane concentration (ϕ = 50 vol%) and in (d) to (f), for high octane concentration (ϕ = 70 vol%). The foams featured homogeneously dispersed spherical and

interconnected open cells and possessed struts decorated with SiC nanowires (see details later). Note the presence in the Si_3N_4-based matrix of well distributed sintering additives, especially visible in the back-scattered images showing bright spots related to Y_2O_3. Grey regions related to the mixture of α–, β–Si_3N_4 phase and MgO, as well as black regions related to pores, in accordance with the amount of β–Si_3N_4 phase developed, are also observable (Figure 3.2 (a) for 50 vol% of octane concentration and (d) for 70 vol% of octane concentration, respectively). In addition, we can observe the formation of strong necks among the silicon nitride particles in the struts as well as the presence of microporosity on the cell walls (due to incomplete sintering) for the foams produced with moderate octane concentration (Figure 3.2 (b)). The formation of well-defined necks is related to the rapid heating between particles and enhanced diffusion facilitated by intense thermal radiation [32,38].

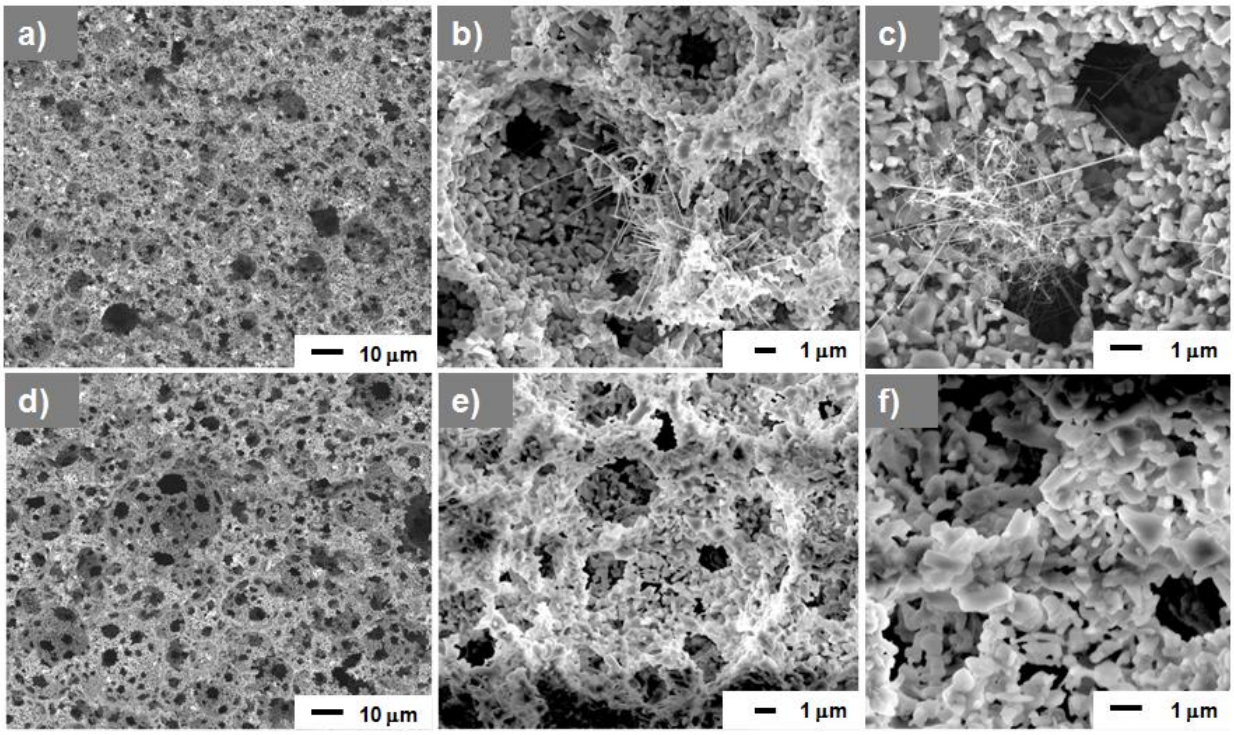

Fig 3.2. SEM images of the fracture surfaces of Si_3N_4 , PLSPS-1 sintered foams obtained from: (a) to (c) 50 vol%, and (d) to (f) 70 vol% of octane (700 rpm). Note the back-scattered images: (a) for 50 vol% of octane concentration and (d) for 70 vol% of octane concentration, respectively), and the presence of NWs decorating the cell walls.

The alkane concentration mainly influenced the amount of total porosity, which increased from 79 to 86 vol% when the octane concentration increased from 50 to 70 vol%, while the average cell size value was quite similar for both alkane concentrations, as a result of an equilibrium between droplet break-up and re-coalescence (so called "over-processing") [39].

The average cell size and cell window size, the total porosity and the mechanical strength values (see later) of Si_3N_4 sintered foams are summarized in Table 3.1.

The size distribution for the microporosity in cell walls and in the struts as well as for the cell windows was obtained by the mercury intrusion method, and the data (see later) are reported in Table 3.2. The average values reported in the table were deduced from the two main peaks of the multimodal pore diameter distribution curves obtained by mercury porosimetry (see Figure 3.3). Changing the sintering regime reduces the microporosity: the PLSPS-1 cycle leads to a higher α– to β–Si_3N_4 phase transformation, with a certain level of interparticle porosity, while the PLSPS-2 cycle enhances the densification of the struts and cell walls. With increasing the stirring velocity from 700 to 1000 rpm, the average cell window size decreased in accordance with the reduction in the average cell size (see later).

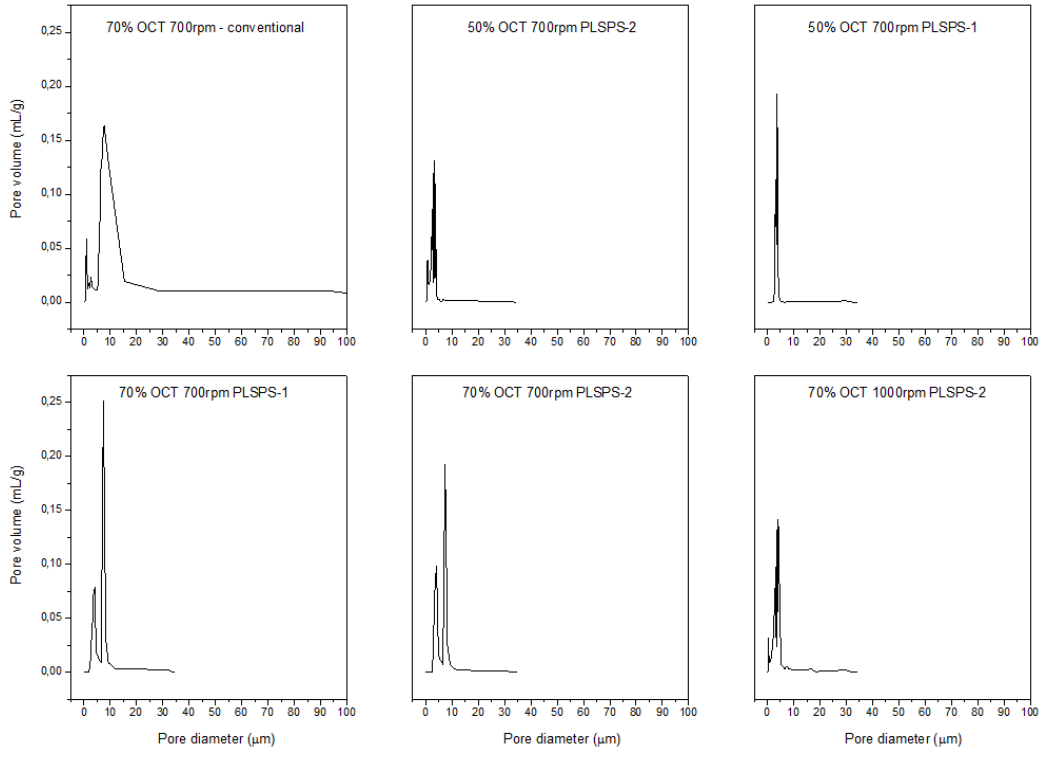

Fig 3.3. Pore volume and diameter for foam samples produced using the two SPS sintering regimes (PLSPS-1 and PLSPS-2) and conventional sintering, produced with 50 and 70 vol% of octane at different stirring speeds (700 and 1000 rpm).

The microstructure of surfactant stabilized foams shows the presence of interconnected porosity (open cells) because the thin liquid films between the bubbles can rupture when adjacent oil bubbles come into contact and during drying. The number of droplets in the system increases with the amount of added oil during emulsification, making droplet-to-droplet contact during processing more probable (Figure 3.2(e)) [40]. Contrarily to the emulsification method, the alternative fabrication approach of particle stabilization leads to Si_3N_4 foams possessing spherical but closed pores, as reported by Yu et al. [41], because the displacement of powder from the gas-liquid interface is thermodynamically unfavorable. In the case of emulsions, foaming is driven by the autonomous evaporation of the alkane phase [28], and the emulsified suspensions are consolidated by the expansion of the alkane droplets and drying of the aqueous medium.

Two main destabilization processes occurring in wet foams, Ostwald ripening and coalescence (film rupture) [2], decrease the overall system free energy leading to foam destabilization and consequently a variation in the cell size [27]. Figure 3.4 shows the cell size and cell window size distributions (D_{10} and D_{90}) for samples processed using the PLSPS-1 sintering cycle, obtained from image analysis. They ranged from 18 to 31 μm (D_{50} = 25.0 ± 0.6 μm) and 3 to 8 μm (D_{50} = 5.6 ± 0.6 μm), respectively, for octane foams with moderate concentration of the alkane phase (ϕ = 50 vol%, 700 rpm), see Figure 3.4 (a) and (c); from 16 to 39 μm (D_{50} = 26.0 ± 1.2 μm) and 4 to 10 μm (D_{50} = 6.3 ± 1.0 μm), respectively, for octane foams with high concentration of the alkane phase (ϕ = 70 vol%, 700 rpm), see Figure 3.4 (b) and (d). The size distribution was narrower for the sample produced using a lower amount of octane, indicating that this system produces more stable wet foam.

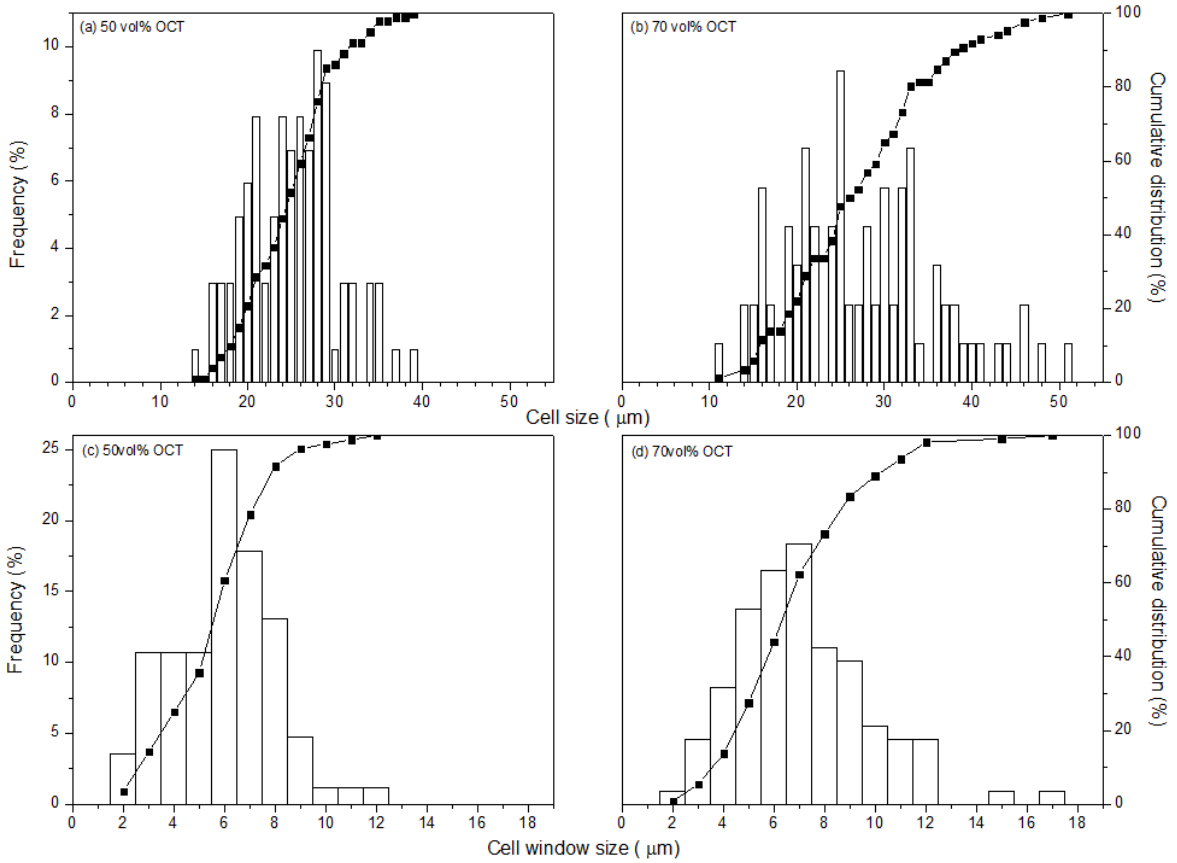

Fig 3.4. Cumulative cell size and cell window size distribution of Si_3N_4, PLSPS-1 sintered foams produced using: (a) and (c) 50 vol%, and (b) and (d) 70 vol% of octane (700 rpm).

Figure 3.5 shows the microstructure of Si_3N_4 foams sintered using the PLSPS-2 sintering regime, produced using 70 vol% of octane and stirred for 3 min at: 700 rpm (a) and (b), and 1000 rpm (c) and (d). The main morphological features of the foams (spherical and interconnected cells) were similar to those of samples processed using the PLSPS-1 sintering regime.

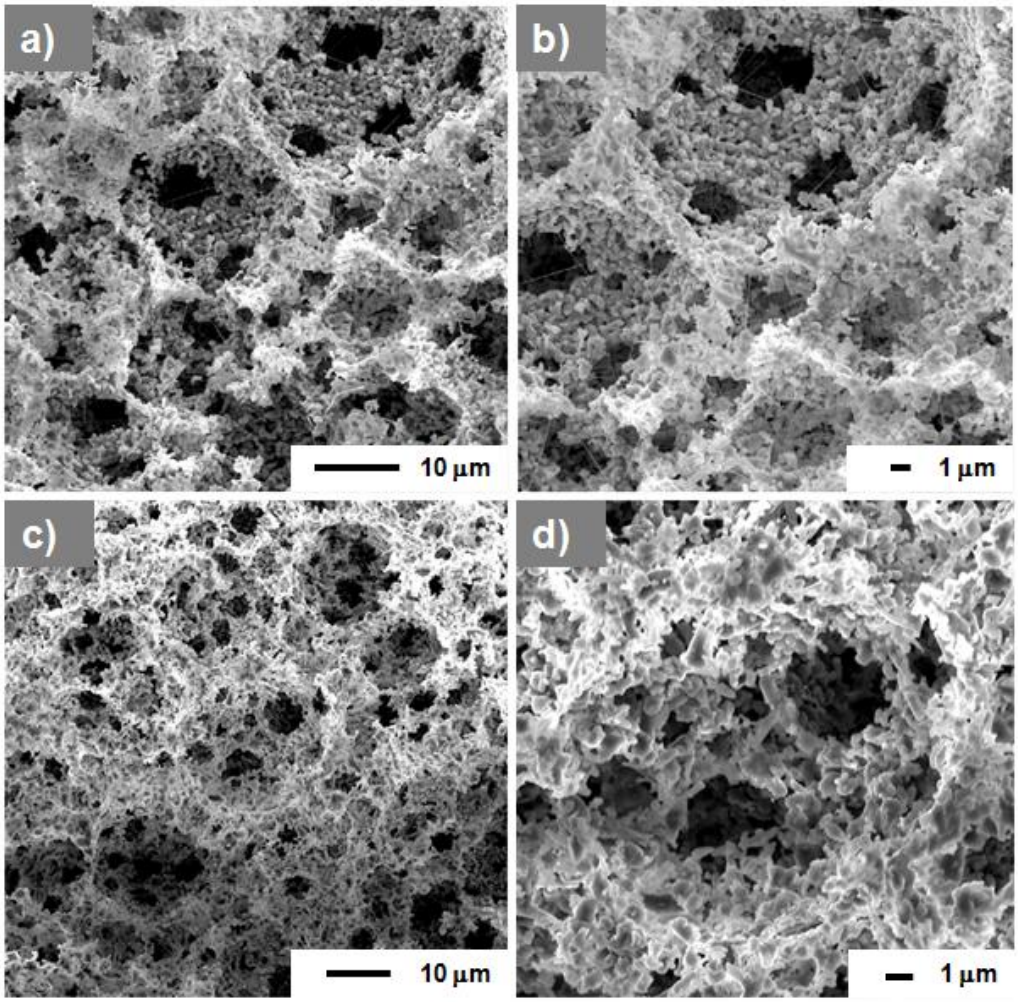

Fig 3.5. SEM images of the fracture surface of Si_3N_4, PLSPS-2 sintered foams containing 70 vol% of octane stirred for 3 min at: (a) and (b) 700 rpm, and (c) and (d) 1000 rpm. Note the presence of NWs decorating the cell walls.

Figure 3.6 reports the cumulative cell size and cell window size distribution of Si_3N_4, PLSPS-2 sintered foams containing 70 vol% of octane stirred for 3 min at: (a) and (c) 700 rpm, and (b) and (d) 1000 rpm. With increasing the stirring velocity from 700 to 1000 rpm, the D_{50} value for the cell size decreased from 24 ± 0.9 to 14 ± 1.9 μm, and the D_{50} for the cell window size from 6.0 ± 1.0 to 4.8 ± 0.8 μm, mainly as a result of the increase of the shear rate (from 381 to 544 s^{-1}) which leads to the breaking up of the oil drops into smaller droplets [26,27].

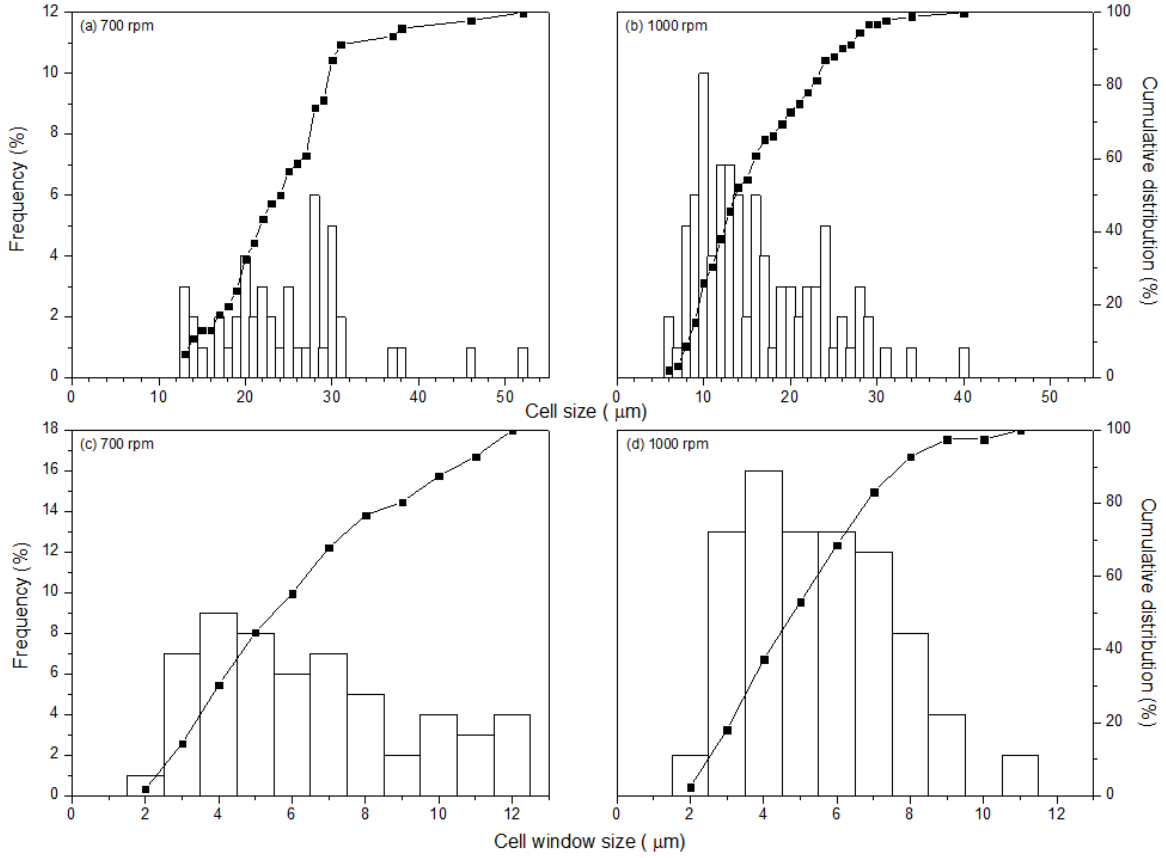

Fig 3.6. Cumulative cell size and cell window size distribution of Si_3N_4 (PLSPS-2) sintered foams containing 70 vol% of octane stirred for 3 min at: (a) and (c) 700 rpm, and (b) and (d) 1000 rpm.

The stirring velocity also had a strong influence on the size of the micropores (pores in the struts and cell walls that decreased from 0.9 to 0.4 μm, see Table 3.2) because of the higher solid packing in the aqueous slurry, leading also to a larger amount of closed porosity (see Table 3.2). The total porosity value was quite similar for both stirring velocities (see Table 3.1), because the amount of oil used to form the porosity was the same, indicating that the amount of microporosity in the struts of the samples is limited with respect to the total porosity.

The mercury porosimetry analysis (see Table 3.2), conducted on octane foams stirred at 700 rpm and sintered using the PLSPS-1 regime, gave data in agreement with the values reported in Table 3.1, with an average cell window size of about 3 μm and 79.5 vol% of porosity for moderate octane concentration (50 vol%), and an average cell window size of about 5 μm and 87 vol% of porosity for high octane concentration (70 vol%). Note that mercury porosimetry measurements

give the amount of open porosity, and therefore the results indicate that the produced foams had a completely interconnected cellular structure.

Peng et al. [22] suggested that the ratio of the cell window (d) to cell diameter (D) is directly related to the pore volume fraction in the case of a face centered cubic array of cells of uniform diameter, and this allows to quantitatively compare different cellular microstructures. It is important to note that the permeability, hence the flow rate, is very dependent on the pore size and pore volume [42]. The ratio d/D was plotted in Figure 3.7 for foams produced using the PLSPS-2 sintering regime and different stirring rates as function of pore volume fraction, V_p, calculated according to equation (1), suggested by Peng et al. [22]:

$$V_P = \frac{\pi}{\sqrt{2}}\left[\frac{3}{1-k^2} - \frac{5}{3}\left(\frac{1}{\sqrt{1-k^2}}\right)^3 - 1\right] \tag{3.1}$$

where $k = d/D$. Note that for cellular ceramics, $0.7 < V_p < 1.0$ [43].

The calculated total porosity values (V_p) show good agreement with those calculated from the measured weight-to-volume ratio of the foams (see Table 3.1), therefore confirming the good uniformity in the cell size distribution for the produced foams and the significant effect of the stirring rate on the cellular architecture.

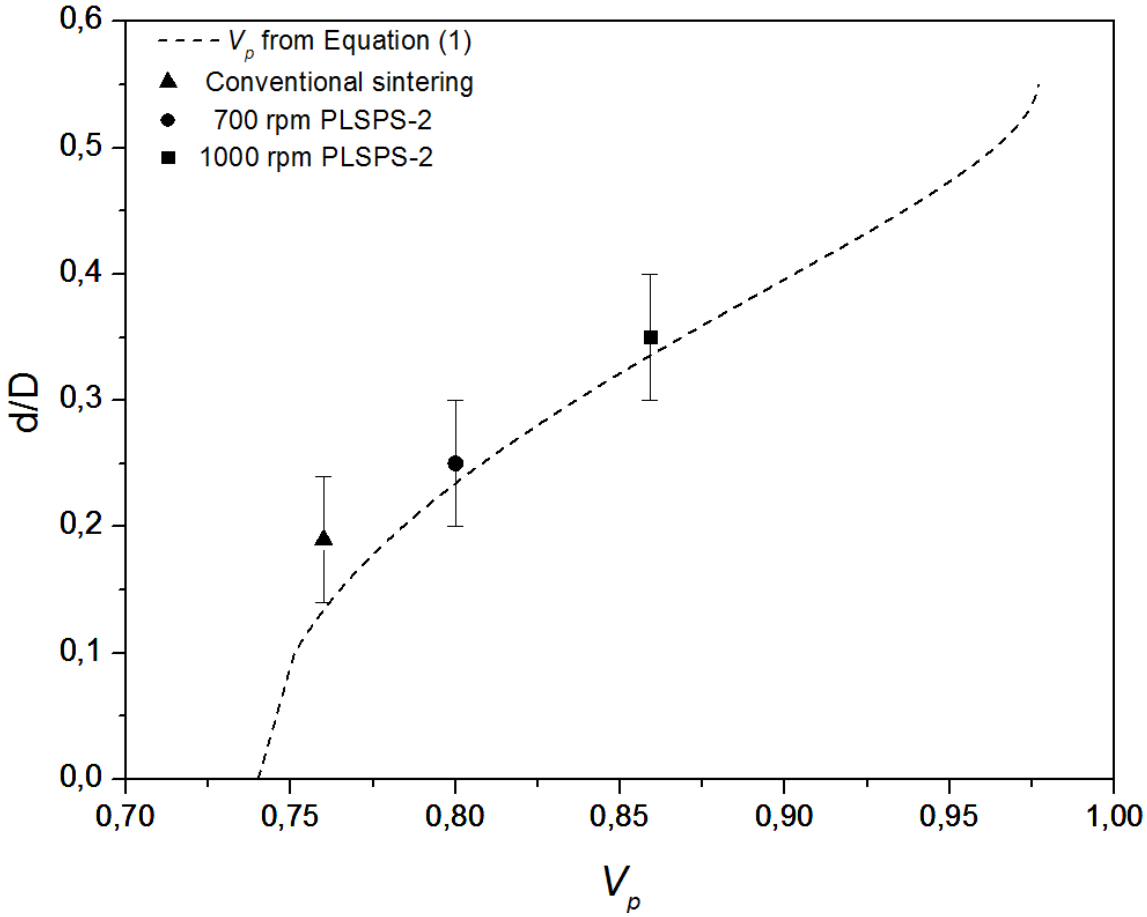

Fig 3.7. The ratio d/D as a function of the pore volume fraction, V_p, for Si_3N_4 foams sintered using the PLSPS-2 sintering regime (70 vol% of octane, stirred at 700 and 1000 rpm) and a foam processed by conventional sintering (70 vol% of octane, stirred at 700 rpm [29]).

Some of the SEM images of the sintered samples show the presence of nanowires (NWs) with a length of a few micrometers protruding from the cell walls of the foams, independently on the processing conditions (stirring rate, amount of octane and sintering regime) adopted. TEM analysis (see Figure 3.8) showed that the nanowires, with average diameter ~150 nm, had a tip-body structure.

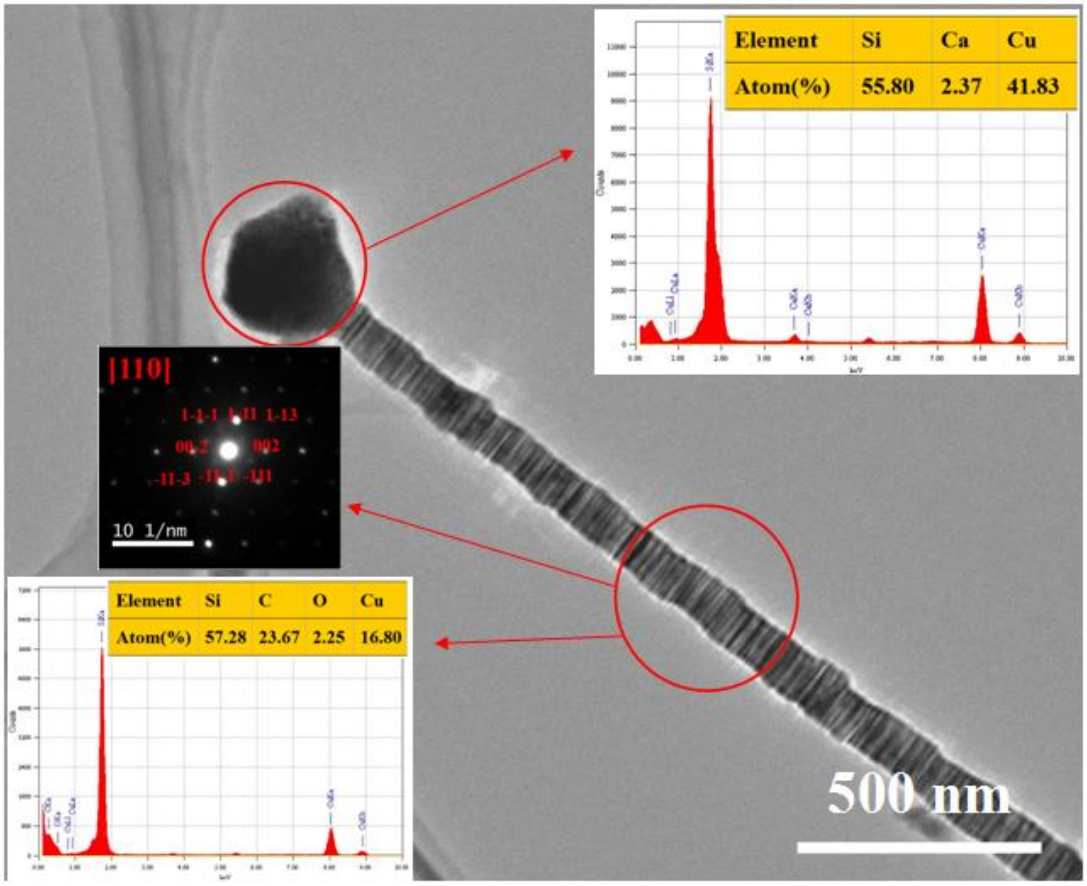

Fig 3.8. TEM/SAED/EDX analysis of the NWs present on the cell walls of Si_3N_4 sintered foams (PLSPS-1 sintering regime, 70 vol% octane, 700 rpm).

The EDX analysis of the body of the NW showed the presence of Si, C, O (from the oxidized surface) and Cu (from the grid), while the indexed selected-area electron diffraction (SAED) patterns collected were compatible with the [110] planes of α–SiC, confirming the XRD data and proving that the NW was constituted of silicon carbide. The EDX data for the tip indicated the presence of Si, Ca (from the raw powder) and Cu (from the grid). A detailed investigation of the catalyst-assisted vapor-liquid-solid mechanism for the growth of the NWs can be found in Ref. [32].

Mechanical strength of sintered foams

The compressive strength of Si_3N_4 rapid sintered (PLSPS-1) foams emulsified with 50 or 70 vol% of octane is reported in Table 3.1. The strength values decreased from 9.9 ± 0.9 (for moderate octane concentration, 50 vol%) to 1.7 ± 0.3 MPa (for high octane concentration, 70 vol%) when the porosity increased from ~79 to 86 vol% (see Table 3.1), respectively. A similar trend has been

observed for many other porous silicon nitride ceramics fabricated by different techniques such as reaction sintering [19,20,44], sacrificial templates [21,45] or partial sintering [46], and is related to the decrease in the amount of load bearing material with increasing porosity [43]. The strength of PLSPS-1 foam is ~30% higher than the PLSPS-2 one, due to the higher amount of β–Si_3N_4 [32]. A direct comparison with the strength of foams produced using conventional sintering (1600 °C in N_2 flux) is more difficult, as they possessed a lower average porosity (~73 vol%) and a compressive strength of ~14 MPa (see Table 3.1) [29], but we can note that the rapid sintering by intense thermal radiation of foams produced in the same experimental conditions (70 vol% octane, 700 rpm) led to cellular structures of lower density, due to the presence of a higher amount of intergranular porosity in the cell walls and struts. This, in turn, could be attributed to a higher decomposition of silicon nitride caused by the localized intense radiation, the use of vacuum and a more enhanced α– to β–phase transformation. It is interesting to note that the grain growth was inhibited when Si_3N_4 foams (70 vol% octane, 700 rpm) were sintered by the PLSP-1 sintering regime, in comparison to conventionally sintered foams. In the first case (SPS processing), the average grain size for the α–Si_3N_4 phase was 1.7 ± 0.1 μm, while in the case of conventional sintering it was 3.7 ± 0.1 μm. This effect was also noticed by Zhang et al. [38], and led to improved mechanical properties because of the enhanced neck formation.

The data in Table 3.1 correlate the mechanical behavior of the foams with the total porosity and average cell size values. As shown by Sepulveda [47], in foams produced by direct foaming the cell size varies with the bulk density, typically increasing with increasing porosity. Although it is impossible to separate the simultaneous contribution of density and cell size on the mechanical strength of cellular structures, we can observe that the pore shape influences the strength and fracture energy [48], e.g., there is no stress concentration for spherical or cylindrical pores under uniaxial compression [49]. However, one should also consider the differences in the microstructure of the samples, especially the fact that foams processed using 70 vol% of octane had thinner struts because the thickness of the liquid films around the gas bubbles was reduced for highly concentrated octane foams, and the number of cell windows was higher (see Figure 3.2) [50]. More investigations are needed to better elucidate the specific and independent contribution of each factor (amount of porosity, cell and cell windows size, strut thickness) to the overall mechanical strength of ceramic foams.

Table 3.1. Summary of the physical properties of the Si_3N_4 foams from the emulsification process.

Si_3N_4 foams	*Cell size, d_{50}[a] (μm)*	*Cell window size, d (μm)*	*Total Porosity[b] (vol%)*	*d/d_{50}*	*V_P[c]*	*σ Compressive strength (MPa)*
Conventional Pressureless Sintering 1600ºC, N_2 flow **[29]**						
70 vol% OCT 700 rpm	~ 18 to 47	~ 4 to 10	~71 to ~75	0.19[d]	0.779[d]	~5 to ~20
Rapid Sintering - PLSPS-1 under vacuum						
50 vol% OCT 700 rpm	25 ± 2.2	6 ± 0.4	79 ± 0.5	0.24	0.802	9.9 ± 0.9
70 vol% OCT 700 rpm	26 ± 1.2	6 ± 0.9	86 ± 0.3	0.23	0.797	1.7 ± 0.3
Rapid Sintering - PLSPS-2 under vacuum						
50 vol% OCT 700 rpm	27 ± 1.7	7 ± 0.4	79 ± 0.4	0.25	0.808	8 ± 1.0
70 vol% OCT 700 rpm	24 ± 0.9	6 ± 1.0	86 ± 0.1	0.25	0.808	-
70 vol% OCT 1000 rpm	14 ± 1.9	5 ± 0.8	85 ± 0.3	0.35	0.868	1 ± 0.1

[a] Cumulative cell size distribution, d_{50}, measured from SEM images using linear intercept method.

[b] Calculated by assuming that the theoretical density of Si_3N_4 ceramic is 3.2 g cm^{-3}.

[c] Pore volume fraction, V_P, determined.

[d] Sample's density = 0.845 g/cm^3 [29].

Table 3.2. Summary of results for the size of microporosity (in the cell walls and the struts) and cell windows, and for the porosity of Si_3N_4 foams from the emulsification process. Data were obtained from mercury intrusion measurements.

Si_3N_4 Octane foams	*Struts/cell wall average pore size* [a] *(μm)*	*Cell windows average size* [a] *(μm)*	*Bulk density (g/cm^3)*	*Total porosity (vol%)*	*Open porosity (vol%)*
Conventional Pressureless Sintering 1600ºC, N_2 flow **[29]**					
70 vol% OCT 700 rpm	0.7	4.6	0.6320 ± 0.03	80.3	70.9
Rapid Sintering - PLSPS-1 under vacuum					
50 vol% OCT 700 rpm	0.7	3.3	0.7006 ± 0.04	78.1	72.1
70 vol% OCT 700 rpm	1.6	7.4	0.4390 ± 0.02	86.3	73.3
Rapid Sintering - PLSPS-2 under vacuum					
50 vol% OCT 700 rpm	-	3.5	0.7044 ± 0.04	77.9	66.2
70 vol% OCT 700 rpm	0.9	7.4	0.4503 ± 0.02	86.0	72.9
70 vol% OCT 1000 rpm	0.4	3.7	0.5966 ± 0.03	81.3	61.6

[a]Value selected from the individual peaks of the multimodal pore diameter distribution (see Figure 3.3).

3.4 Conclusions

Cellular silicon nitride components possessing homogeneous microstructure with fully interconnected cells and high level of porosity (> 79%) were prepared using emulsions. Using different octane concentrations, it was possible to control the amount of porosity from ~79 to ~86 vol%, while variations in the stirring velocity (as a result of the increase in the shear rate) affected the average cell size enabling the fabrication of foams with small cell size (ranging from ~14 to ~27 μm) and narrow size distribution, and cell window size from ~5 to ~8 μm. The applied consolidation process, sintering by intense thermal radiation (SITR), generated ceramic foams with compressive strength ranging from ~2.0 to ~10 MPa at lower temperature and shorter time in comparison with conventional pressureless sintering.

References

[1] Scheffler M, Colombo P. Cellular ceramics: structure, manufacturing, properties and application. Weinheim: Wiley-VCH; 2005.

[2] Studart AR, Gonzenbach UT, Tervoort E, Gauckler LJ. Processing routes to macroporous ceramics - A review. *J Am Ceram Soc* 2006;**89**(6):1771–89.

[3] Gauckler LJ, Waeber MM, Conti C, Jacobduliere M. Ceramic foam for molten-metal filtration. *J Met* 1985;**37**(9):47–50.

[4] Chen QZ, Rezwan K, Armitage D, Nazhat SN, Boccaccini AR. The surface functionalization of 45S5 Bioglass-based glass-ceramic scaffolds and its impact on bioactivity. *J Mater Sci Mater Med* 2006;**17**(11):979–87.

[5] Chen QZ, Thompson ID, Boccaccini AR. 45S5 Bioglasss - derived glass–ceramic scaffolds for bone tissue engineering. *Biomater* 2006;**27**(11):2414–25.

[6] Colombo P. Conventional and novel processing methods for cellular ceramics. *Phil Trans R Soc A* 2006;**364**(1838):109–24.

[7] Greil P. Advanced Engineering Ceramics. *Adv Mater* 2002;**14**(10): 709–16.

[8] Riley FL. Silicon nitride and related materials. *J Am Ceram Soc* 2000;**83**(2):245–65.

[9] Moreno R, Salomoni A, Stamenkovic I, Castanho SM. Colloidal filtration of silicon nitride aqueous slips, part II: slip casting and pressure casting performance. *J Eur Ceram Soc* 1999;**19**(1):49–59.

[10] Yang JF, Beppu Y, Zhang GJ, Ohji T, Kanzaki S. Synthesis and Properties of Porous Single-Phase β'-SiAlON Ceramics. *J Am Ceram Soc* 2002;**85**(7):1879–81.

[11] Petzow G, Hermann M. Silicon nitride ceramics. In: Jansen M, editor. High performance non-oxide ceramics II. Berlin: Springer Berlin Heidelberg; 2002. p. 47–167.

[12] Yang JF, Deng ZY, Ohji T. Fabrication and characterisation of porous silicon nitride ceramics using Yb_2O_3 as sintering additive. *J Eur Ceram Soc* 2003;**23**(2):371–78.

[13] Ling G, Yang H. Pressureless sintering of silicon nitride with magnesia and yttria. *Mater Chem Phys* 2005;**90**(1):31–34.

[14] Alper AM. Phase diagrams in advanced ceramics. London: Acad Press Ltd; 1995.

[15] Lange H, Wötting G, Winter G. Silicon nitride-from powder synthesis to ceramic materials. *Angew Chem Int Engl* 1991;**30**(12):1579–97.

[16] Moreno R, Salomoni A, Castanho SM. Colloidal filtration of silicon nitride aqueous slips, part I: optimization of the slip parameters. *J Eur Ceram Soc* 1998;**18**(4):405–16.

[17] Kondo N, Inagaki Y, Suzuki Y, Ohji T. Fabrication of porous anisotropic silicon nitride by using partial sinter-forging technique. *Mater Sci Eng A* 2002;**335**(1-2):26–31.

[18] Inagaki Y, Kondo N, Ohji T. High performance porous silicon nitrides. *J Eur Ceram Soc* 2002;**22**(14-15):2489–94.

[19] Ziegler G, Heinrich J, Wötting G. Relationships between processing, microstructure and properties of dense and reaction-bonded silicon nitride. *J Mater Sci* 1987;**22**(9):3041–86.

[20] Moulson AJ. Reaction-bonded silicon nitride: its formation and properties. *J Mater Sci* 1979;**14**(5):1017–51.

[21] Díaz A, Hampshire S. Characterisation of porous silicon nitride materials produced with starch. *J Eur Ceram Soc* 2004;**24**(2):413–19.

[22] Peng HX, Fan Z, Evans JRG, Busfield JJC. Microstructure of ceramic foams. *J Eur Ceram Soc* 2000;**20**(7):807–13.

[23] Huang Y, Ma L, Tang Q, Yang J, Xie Z, Xu X. Surface oxidation to improve water-based gelcasting of silicon nitride. *J Mater Sci* 2000;**35**(14):3519–24.

[24] Nangrejo MR, Bao X, Edirisinghe MJ. Preparation of silicon carbide-silicon nitride composite foams from pre-ceramic polymers. *J Eur Ceram Soc* 2000;**20**(11):1777–85.

[25] Gonzenbach UT, Studart AR, Tervoort E, Gauckler LJ. Stabilization of foams with inorganic colloidal particles. *Langmuir* 2006;**22**(26):10983–88.

[26] Barg S, Moraes EG, Koch D, Grathwohl G. New cellular ceramics from high alkane phase emulsified suspensions (HAPES). *J Eur Ceram Soc* 2009;**29**(12):2439–46.

[27] Schmitt V, Leal-Calderon F, Bibette J. Preparation of monodisperse particles and emulsions by controlled shear. In: Antonietti M, editor. Colloid chemistry II. Berlin: Springer Berlin Heidelberg; 2003. p. 195–215.

[28] Barg S, Soltmann C, Andrade M, Koch D, Grathwohl G. Cellular ceramics by direct foaming of emulsified ceramic powder suspensions. *J Am Ceram Soc* 2008;**91**(9):2823–29.

[29] Moraes EG, Colombo P. Silicon nitride foams from emulsions. *Mat Lett* 2014;**128**:128–31.

[30] Reymond JP, Kolenda F. Estimation of the point of zero charge of simple and mixed oxides by mass titration. *Powder Technol* 1999;**103**(1):30–6.

[31] Nagel A, Petzow G, Greil P. Rheology of aqueous silicon nitride suspensions. *J Eur Ceram Soc* 1989;**5**(6):371–78.

[32] Li D, Moraes EG , Guo P, Zou J, Zhang J, Colombo P, Shen Z. Rapid sintering of silicon nitride foams decorated with one-dimensional nanostructures by intense thermal radiation. *Sci Technol Adv Mater* 2014;**15**(4):045003.

[33] Blanchard CR, Schwab ST. X-ray diffraction analysis of the pyrolytic conversion of perhydropolysilazane into silicon nitride. *J Am Ceram Soc* 1994;**77**(7):1729–39.

[34] Wang CM, Pan X, Rühle M, Riley FL, Mitomo M. Silicon nitride crystal structure and observations of lattice defects. *J Mater Sci* 1996;**31**(20):5281–98.

[35] Bae S, Baik S. Critical concentration of MgO for the prevention of abnormal grain growth in alumina. *J Am Ceram Soc* 1994;**77**(10):2499–504.

[36] Tan CY, Yaghoubi A, Ramesh S, Adzila S, Purbolaksono J, Hassan MA, Kutty MG. Sintering and mechanical properties of MgO-doped nanocrystalline hydroxyapatite. *Ceram Int* 2013;**39**(8):8979–83.

[37] Hampshire S, Jack KH. Densification and transformation mechanisms in nitrogen ceramics. In: Riley FL, editor. Progress in Nitrogen Ceramics. Lancaster: Martinus Nijhoff publ;1983. 225-230.

[38] Zhang F, Lin K, Chang J, Lu J, Ning C. Spark plasma sintering of macroporous calcium phosphate scaffolds from nanocrystalline powders. *J Eur Ceram Soc* 2008;**28**(3):539–45.

[39] Karbstein H, Schubert H. Developments in the continuous mechanical production of oil-in-water macro-emulsions. *Chem Eng Process: Process Intensif* 1995;**34**(3):205–11.

[40] Schramm, Laurier L. Emulsions, foams, and suspensions: fundamentals and applications. Weinheim: Wiley-VCH; 2005.

[41] Yu J, Yang J, Li H, Xi X, Huang Y. Study of particle-stabilized Si_3N_4 ceramic foams. *Mater Lett* 2011;**65**(12):1801–04.

[42] Nettleship I. Applications of porous ceramics. *Key Eng Mater* 1996;**122**:305–24.

[43] Gibson LJ, Ashby MF. Cellular Solids: Structure and Properties. 2nd edition. Cambridge: Cambridge University Press; 1999.

[44] Hampshire S. Silicon nitride ceramics – review of structure, processing and properties. *J Achiev Mater Manuf Eng* 2007;**24**(1):43–50.

[45] Díaz A, Hampshire S, Yang JF, Ohji T, Kanzaki S. Comparison of mechanical properties of silicon nitrides with controlled porosities produced by different fabrication routes. *J Am Ceram Soc* 2005;**88**(3):698–706.

[46] Yang JF, Ohji T, Kanzaki S, Díaz A, Hampshire S. Microstructure and mechanical properties of silicon nitride ceramics with controlled porosity. *J Am Ceram Soc* 2002;**85**(6):1512–16.

[47] Sepulveda P. Gelcasting foams for porous ceramics. *Ceram Bull* 1997;**76**(10):61–65.

[48] Gündüz G. Effect of porosity on interfacial failure in steel-fibre-reinforced polymer-impregnated concrete. *Comp Sci Tech* 1988;**32**(2):121–36.

[49] Rice RW. Porosity of ceramics. New York: Marcel Dekker Inc.; 1998.

[50] Brezny R, Green DJ, Dam CQ. Evaluation of strut strength in open-cell ceramics. *J Am Ceram Soc* 1989;**72**(6):885–89.

4. Silicon nitride foams from gelcasting of biopolymers

E. G. de Moraes and P. Colombo, "Silicon nitride foams from gelcasting of biopolymers", manuscript in preparation.

4.1 Introduction

Cellular ceramics are materials tailored to possess exceptional combination of properties as high porosity and lightweight, as well special functional properties, such as low thermal conductivity, high-temperature stability, and excellent thermal shock resistance, good resistance against crack propagation, high permeability and high surface area. These materials are used for a wide range of technological applications, such as filters, membranes, catalyst substrate, thermal insulation, gas burner media, refractory materials, as well as porous implants in the area of biomaterials [1–4].

Silicon nitride (Si_3N_4) is one of the most promising materials in various engineering applications, owing to the good combination of high mechanical performance (even with certain levels of porosity) [5] and thermal properties, such as, high strength at temperatures above 1000 °C, good thermal stress resistance, combined with the low density of Si_3N_4 (3.2 $g \cdot cm^{-3}$) consists an important advantage [6]. Also the outstanding properties as fracture toughness, hardness, friction and wear resistance has pointed Si_3N_4 composites as interesting candidates for many high-load medical applications [5].

However, the high cost of production (sintering is generally assisted by pressure), due to the highly covalent bonding between silicon and nitrogen atoms and very slow solid-state diffusion [7], limits significantly the use of silicon nitride-based ceramics to specialized, high value applications. The additions of sintering additives, which are usually metal oxides that form a eutectic liquid phase with the oxide surface layers of the silicon nitride powder, improve sintering activity considerably and promote the solution-precipitation process, in which α–grains dissolve into the liquid phase and precipitate as β–grains, known as the α→β phase transformation [8–10].

The development of more economical processes for the production of silicon nitride component in structural applications, with proper process control and uniformity in the properties of the final product, is a challenge from a technological point of view [11].

Foams based on silicon nitride can be processed by direct foaming methods, such as preceramic polymers [12], particle stabilized foams [13], emulsification based on surfactant stabilization [14] and gelcasting [15], among others.

The current work is concerned with the fabrication of silicon nitride foams with tailored microstructure in terms of porosity (> 75vol%) and cell size distribution (> 150 μm) using a gelcasting processing method associated with the aeration of an aqueous suspension using environmentally friendly biopolymers as gelling agents. Alternative biopolymers such as globular proteins (egg white albumen) [16], agar-agar [17,18], and methylcellulose [18,19] are used to produce silicon nitride foams by means of in situ formation of a percolating network of ceramic particles maintaining both macrostructures and microstructures.

The microstructure, mechanical properties and permeability of the gelcasting Si_3N_4 foams pressureless sintered were evaluated. Additionally, the influence of the sintering additives, Y_2O_3 and MgO, and the effect of the temperature on the formation of rod-like β–grains were investigated.

4.2 Experimental procedure

Solution preparation

Agar-agar (Erbamea S.r.l, Italy) was used as gelling additive. 3 wt% of agar solutions (1 wt% of agar powder based on the Si_3N_4 powder suspension content) were prepared in a flask by mixing the gel-former with deionized water heated up to 90 °C during 120 min [17,18].

Water-soluble methylcellulose (MC), Methocel™ A4M (Dow Chemical Company, Italy) was used as gelling additive. 0.5 wt% of methylcellulose solutions were prepared in a flask containing deionized water (Millipore, electrical resistivity > 18 $M\Omega \cdot cm^{-1}$) heated up to 90 °C followed by addition of the gel-former and subsequent magnetic stirring during 120 min. Afterward, the solution was cooled to room temperature in continuous mixing [19].

Suspension preparation and foaming

A detailed procedure for suspension preparation can be found in section 2.2. The preparation of aqueous colloidal suspensions varied according to the gelling agent and thermal gelling procedure used.

In the case of egg white albumen, the water-based Si_3N_4 slurries with 30 vol% of solids (labeled as SN-5YM30), and containing 1 wt% PAA (based on the ceramic powder content) were prepared by step-wise adding the dry powder to deionized water upon continuous stirring with a

laboratory mixer. The ceramic suspension was homogenized by ball milling for 2 hours at 200 rpm using Si_3N_4 cylinders. In case of Si_3N_4 suspensions the pH was set to values above ~11.4 by adding small aliquots of 0.1 N, NaOH. Afterwards, the slurry was aerated with a double shear mixer during 2 minutes followed by addition of 5 wt% of albumen (egg white, based on the ceramic powder content) and subsequently the suspension was vigorous stirred during 10 minutes to foaming. Then, the foams were poured in a Teflon mold and thermal gelling occurs in a dryer at 80 °C for 2 hours to cross-linking of aminoacids (cistein), and at ambient air for approximately 24h. Sintering was conducted in two steps: pre-calcination at 650 °C (2 h; 1 °C/min heating rate), to decompose the organic phase; proceed heat-treating to 1600 °C (3 h, 2 °C/min heating rate) under 99.99 % N_2 flow [14].

For agar, the incorporation of the solution (maintained at 60 °C) required the previous heating of the Si_3N_4 suspension with 35 vol% of solids (labeled as SN-5YM35), at a temperature above the 60 °C, conditions where no water evaporation occurs. After adding the agar solution, the final Si_3N_4 suspension concentration reaches 30 vol% (~59 wt%). Since the gelcasting suspensions containing agar solution and Si_3N_4 suspension are mix together, 1.0 wt% of Tergitol TMN–10 (based on the ceramic powder content), a non-ionic surfactant was incorporated into the hot suspension. Thereafter, the gelcasting suspensions were mechanical stirred (maximum velocity) with a double shear mixer for shearing times of 10 min in order to promote bubble formation [17]. The foams was poured into a plastic mould and cooled down at 15 °C using cold water to promote gel-network formation. The foams were dried at ambient air for approximately 24 h. The sintering of the consolidated foams was performed in two steps as earlier reported for egg white albumen foams.

Particularly for methylcellulose (MC), gelcasting suspensions were prepared by addition of 30 or 35 vol% of solids concentration in a methylcellulose solution (previously prepared) instead of water containing 1 wt% PAA (based on the ceramic powder content), followed by homogenization with ball milling for 2 hours as earlier described for egg white albumen suspension preparation. Thus, a non-ionic surfactant, Tergitol TMN–10, was incorporated in a gelcasting suspension by stirring (maximum velocity) with a double shear mixer during 10 min to foaming. The foams was poured into a silicon mould and kept at ~47 °C overnight to form a gel-network and dried at ambient air for 24 h. The sintering conditions were the same as described above for egg white albumen foams.

Characterization

The crystalline phases were determined on powdered samples by X-ray diffractometry using Bruker AXS D8 Advance diffractometer (CuKα, 40 kV, 40 mA, 0.05°, 2s). The data were analyzed utilizing the ICSD database, and the weight fractions of the α– and β–Si_3N_4 crystalline phases were evaluated by the method described in Ref. [20]. The microstructure of the Si_3N_4 based foams was investigated by scanning electron microscopy (FEI Quanta 200, FEI Italia, Milan, Italy). Cell size and cell windows sizes were measured by the linear intercept method (ASTM E112-12), (diagonal opposite directions), using an image analysis program (Axio Vision LE). The average values were obtained considering stereological relations (ASTM D3576-98), the relationship between the average measured chord length t and the average sphere diameter D is: D = t·1.623. The total porosity was calculated from the weight-to-volume ratio of the samples, while the open porosity and bulk density were measured using a mercury porosimeter (Pascal 140/440 Porosimeter 2000, Germany). The mechanical behavior of the Si_3N_4 based foams was determined by uniaxial compression strength tests performed using a hydraulic mechanical testing machine (1121 UTM, Instron, Norwood, MA, USA), according to ASTM C133-97 standard. The cross-head speed was 1.0 mm/min and the compressive load cell was 5 kN using a universal testing machine (Instron 1121, Instron Danvers, MA; ASTM C133-94). Specimens with a nominal size of 10 mm × 10 mm × 10 mm, cut from larger bodies, were tested for each sample. Each data point represents the average value of five individual tests. The permeability of the Si_3N_4 based foams was evaluated using Forchheimer's equation for compressible fluids:

$$\frac{P_i^2 - P_o^2}{2PL} = \left(\frac{\mu}{k_1}\right) v_s + \left(\frac{\rho}{k_2}\right) v_s^2 \qquad (4.1)$$

in which P_i and P_o are, respectively, the absolute gas pressures at the entrance and exit of the sample, v_s is the superficial gas velocity, determined by dividing the exiting volumetric flow rate Q, by the sample face area A exposed to flow, L (0.5 - 0.8 cm) is the sample's thickness, μ is the gas viscosity (1.77×10^{-5} Pa·s); and ρ is the gas density (1.15 kg·m^{-3}), evaluated for the pressure P_o = 760 mmHg and T = 24 °C. The parameters k_1 (expressed in square meters) and k_2 (expressed in meters), are respectively known as Darcian and non-Darcian permeability coefficients, in reference to Darcy's law, which establishes a linear dependence between ΔP and v_s. These coefficients weigh the contributions of viscous and inertial losses on the total pressure drop, i.e., the influence of viscous and inertial interactions between fluid and the porous medium [21]. The contribution of the

porous structure in Eq. (4.1) is quantified by the thickness L and permeability parameters k_1 and k_2, which are complex functions of the morphology, size distribution, connectivity and volume of the void fraction. [22]. The terms k_1 and k_2 are usually referred as constants, since they are supposed to be independent of the body dimensions and of both fluid and flow conditions, even though they may vary with temperature.

The first term of Forchheimer's equation, $(\mu/ k_1)\cdot v_s$ represents viscous energy losses due to friction between fluid layers and prevails at low fluid velocities. On the other hand, the quadratic term, $(\rho/k_2)\cdot v_s^2$, which is not considered by Darcy's equation, although it becomes increasingly significant at high-speed flow rates, and represents the kinetic energy losses due to changes in the direction of motion and to acceleration or deceleration of the fluid caused by changes in the flow path (contraction or enlargement of the pore section or pore tortuosity along the flow direction)[21,22]. The knowledge of the predominant relationship (linear or quadratic) for the pressure drop curve is critical for designing the best driving equipment for fluid flow in a given application [23].

The experimental evaluation of permeability parameters was carried out with argon flow at room temperature in a laboratory-made hot gas permeameter described elsewhere (see Appendix B.6, Figure B.1). Two to three disks of ~36 mm of diameter and ~7 mm of height were tested for each sample. The gas was forced to flow in stationary regime through the cylindrical samples had their lateral surface previously sealed (using Teflon tape), to allow the gas flow to occur only in the top-bottom direction. The gas velocity was varied between 0 to 6.5 m/sec, using a valve associated with a rotameter. A digital manometer was used to measure the pressure before and after the sample. Following this procedure, a curve $(P_i^2 - P_o^2)/2PL$ versus gas velocity was obtained. This allowed k_1 and k_2 values to be adjusted according to the Forchheimer's equation (4.1) [21,23,24].

4.3 Results and discussion

The X-ray diffraction patterns of the as prepared and sintered Si_3N_4 gelcasting foams are reported in Figure 4.1. The main phase was α–Si_3N_4 in both samples, and an increase in the β–phase was observed after sintering, from 12.9% for the as prepared powders to about ~30% for sintered foams, as estimated based on the ratio of the intensities of the [210] peak for both phases (located at 35.4 2θ for the alpha phase and at 35.9 2θ for the beta phase), using a normalizing factor, L (see Appendix B.1, Table B.1), to correct the peak intensities from errors due to extinction and preferred orientations [20]. The increase in β–Si_3N_4 during sintering in the presence of a liquid Y_2O_3-MgO-

containing phase is owing to a solution-reprecipitation mechanism that starts occurring around 1600 °C and occurs preferentially at the contact areas between particles [8,25,26]. The peaks relative to the sintering aids disappeared almost completely after heating due to their incorporation into an amorphous intergranular phase and no substitution for silicon or nitrogen in the Si_3N_4 structure by metal ions was detected [25–28].

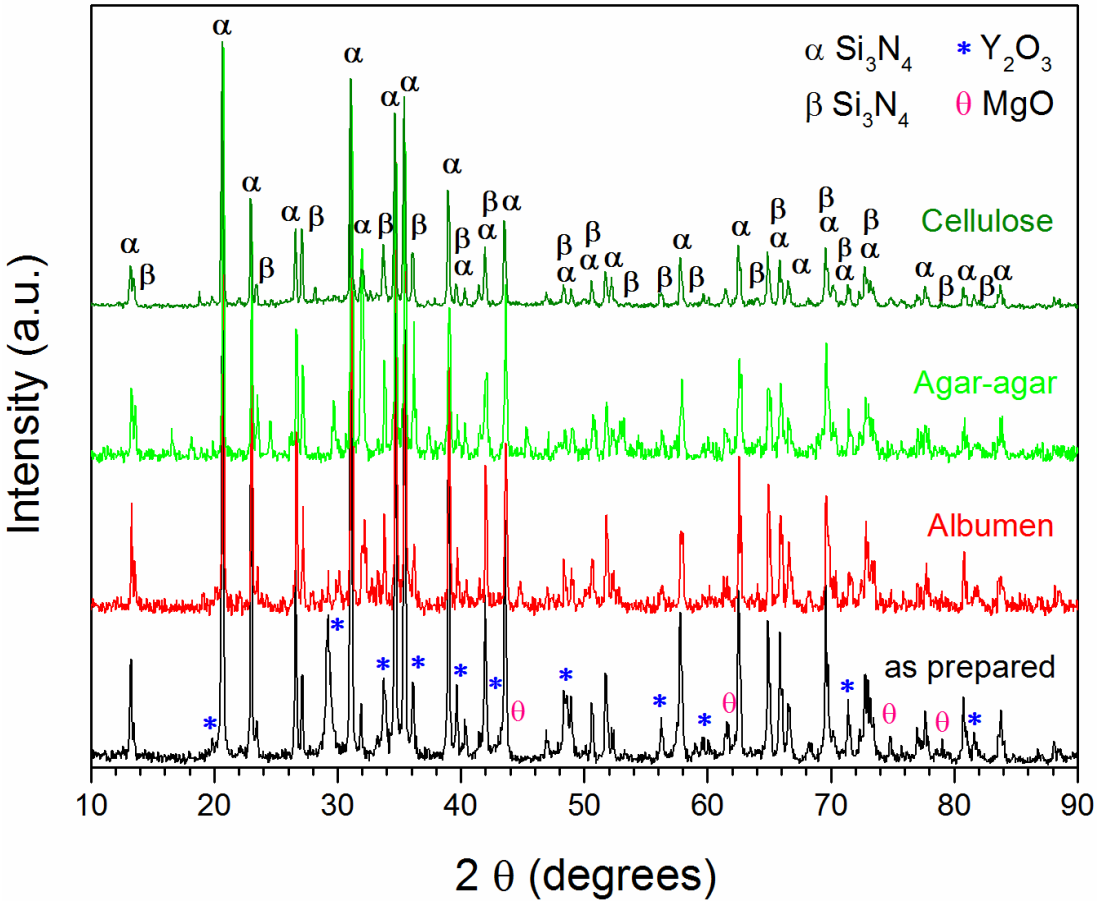

Fig 4.1. XRD patterns for as prepared and sintered Si_3N_4 gelcasting foams (egg white albumen, agar-agar and methylcellulose (labeled as cellulose)) containing 5 wt% Y_2O_3 and 5 wt% MgO. (ICSD α–Si_3N_4 # 04-0360, β–Si_3N_4 # 033-1160, Y_2O_3 # 043-0661, MgO # 045-0946).

The morphology of the SN-5YM30 albumen (egg white) sintered foams presenting an interconnected network of spherical cells (open cells), homogeneously distributed with dense struts is reported in Figure 4.2. The high stability of the wet foams was achieved by thermal gelling of the liquid phase (~80 °C) allowing a narrower distribution in the average cell and window size from

121(D_{10}), 199 (D_{50}) to 278 μm (D_{90}), and from 22 (D_{10}), 51 (D_{50}) to 75 μm (D_{90}), respectively. The average cell size and cell window size, the total porosity and the mechanical strength values (see later) of Si_3N_4 sintered foams are summarized in Table 4.1. The amount of total porosity was on the average ~79 vol%. Note that these values can be related to the adsorption of proteins at air-water interface, which is diffusion controlled. Hereafter, once at interface, a surface denaturation takes place i.e., a slow structural rearrangements and conformational change, which makes the globular protein (egg white) more disordered, and at the same time exposes more hydrophobic residues and lowering the interfacial tension [29]. Which in turns permit coalescence of the bubbles until a complete adsorption of proteins at air-water interface, when a flexible and cohesive film is formed by a high packing density and intermolecular cross-linking reducing gas permeability and inhibiting the variation in the bubbles cell size [30].

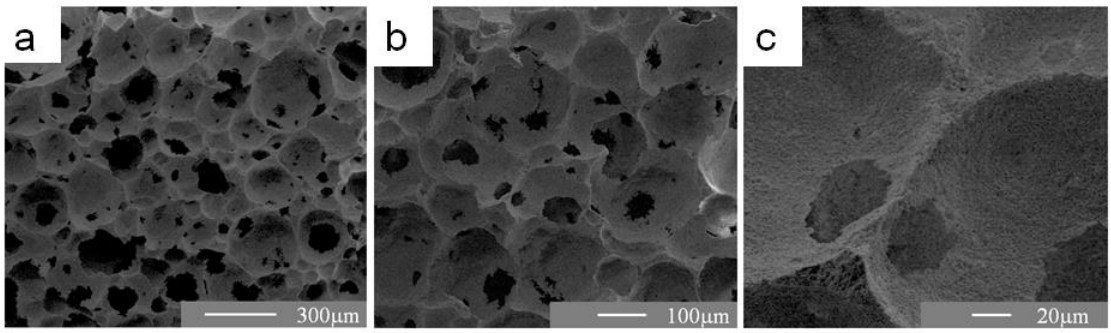

Fig. 4.2. SEM images of the fracture surface of Si_3N_4 sintered gelcasting foams: egg white albumen a) and b) general feature; c) higher magnification (detail of strong packing of particles on cell walls and struts).

Figure 4.3 shows the highly interconnected open cell morphology of SN-5YM30 sintered gelcasting foams: agar a) and b); and methylcellulose c) and d). A general view is reported in Fig. 4.3. a), and the strut structure presenting residual porosity is showed in Fig. 4.3 b), for agar foams. The thermal gelling of the liquid foam containing 1wt% of agar as a solution, occurs during cooling at ~15 °C, using cold water. The use of agar solution inhibits the formation of agglomerates [18] and allows to the homogeneous distribution of the gel-former i.e., high microstructural uniformity; cells do not exhibit particular direction of expansion. A statistical analysis of the data obtained from SEM images showed monomodal distribution of cell size around 302 (D_{10}), 456 (D_{50}) to 798 μm (D_{90}), and cell window size around 45 (D_{10}), 79 (D_{50}) to 160 μm (D_{90}), respectively, see Table 4.1,

note that these values are strongly higher than that for egg white albumen foams owing to foaming ability of surfactants and very dynamic adsorption and desorption of these amphiphiles leading to coalescence mechanism [17].

Methylcellulose foams featuring spherical and interconnected cells were similar to those samples processed using agar as gel-former, however the thermal gelation occurs on heating at ~47 °C, as a result of lose the water of hydration [18] and, consequently polymer–polymer association. Very wide distribution of cell sizes around 428 (D_{10}), 852 (D_{50}) to 1360 μm (D_{90}), and window size around 65 (D_{10}), 152 (D_{50}) to 355 μm (D_{90}), see Table 4.1. Methylcellulose is recognized as a surface-active biopolymer and can be used as emulsifier, but it produces coarser droplets owing to high molecular weight; long time to adsorb at the interface and prevent coalescence of the newly formed droplets [31]. Additionally, some deformation and development of cracks on the cell walls due to insufficient gel consistency, see Fig. 4.3 c) [18]. Since the gel-strength depends of the concentration of methylcellulose, which in turns can sharply affect the viscosity. Note the struts containing some closed porosity in detail on Fig. 4.3 d), owing to combined effect of coalescence (liquid film rupture) and Ostwald ripening i.e., diffusion of gas molecules from smaller to larger bubbles over time [3]. According to Bibette et al., this mechanism does not involve any film rupture: instead, there is a continuous exchange of matter that increases the average droplet diameter while reducing their number [32].

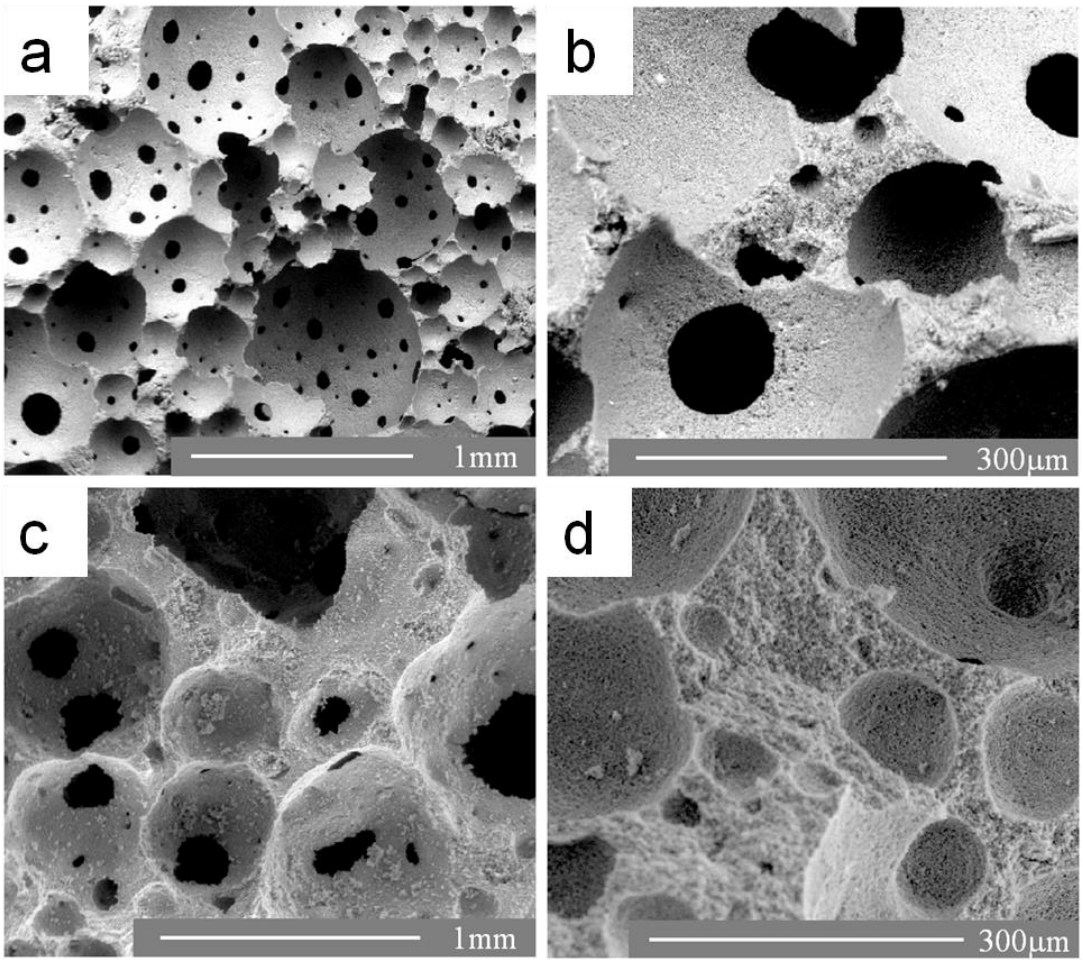

Fig. 4.3. SEM images of the fracture surface of SN-5YM30 sintered gelcasting foams: agar a) general feature and b) higher magnification (detail of porous struts); and methylcellulose c) general view and presence of some cracks, and d) higher magnification (detail of struts containing some closed porosity).

With the increasing of the solids content to 35 vol% of Si_3N_4-based powder concentration, the methylcellulose foams featuring similar interconnected network of cells morphology, however we observed a strong packing of particles on cell walls and struts, as showed in Figure 4.4. Moreover, a similar wide distribution of cell sizes around 333 (D_{10}), 643 (D_{50}) to 1165 μm (D_{90}), and window size around 57 (D_{10}), 119 (D_{50}) to 297 μm (D_{90}), see Table 4.1, these values are slightly lower than for those for 30 vol% of solids concentration. Additionally, the amount of porosity decreases from 89.3 ± 0.5 (SN-5YM30) to 83.0 ± 1.1 vol% (SN-5YM35), see Table 4.1, respectively.

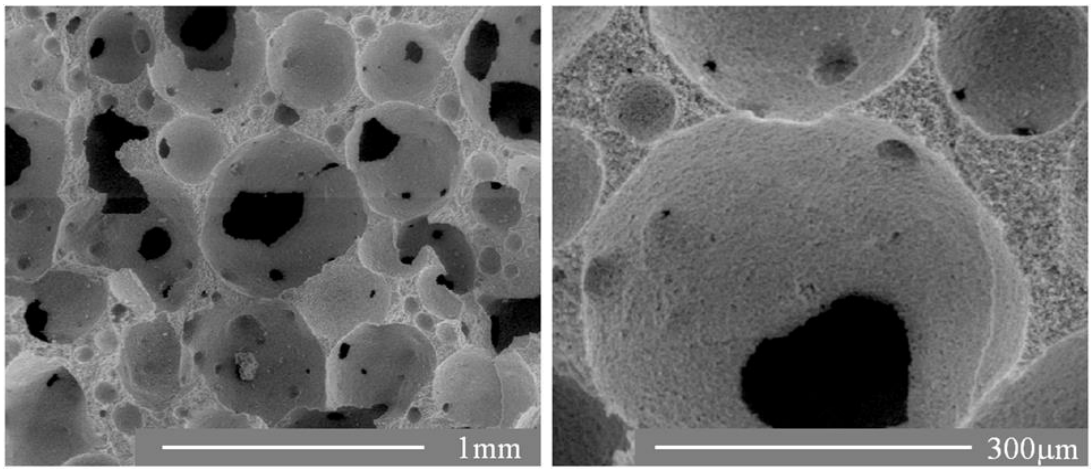

Fig. 4.4. SEM images of the fracture surface of SN-5YM35 sintered methylcellulose foams: general view (on the left) and higher magnification (on the right, detail of a strong packing of particles on cell walls and struts).

The effect of increase sintering temperature up to 1700 °C on the microstructure and α→ β transformation was investigated. The X-ray diffraction patterns of the methylcellulose foams prepared with 35 vol% of solids concentration are reported in Figure 4.5. The β–phase significantly increased up to ~98% (estimated value [20]), since the rate of transformation is increased with sintering temperature enabling the formation of elongated β–Si_3N_4 grains [33]. Additionally, the peaks relative to the sintering aids almost disappeared suggesting their incorporation into intergranular phase, since no substitution for silicon or nitrogen in the Si_3N_4 structure by metal ions was detected [25–28].

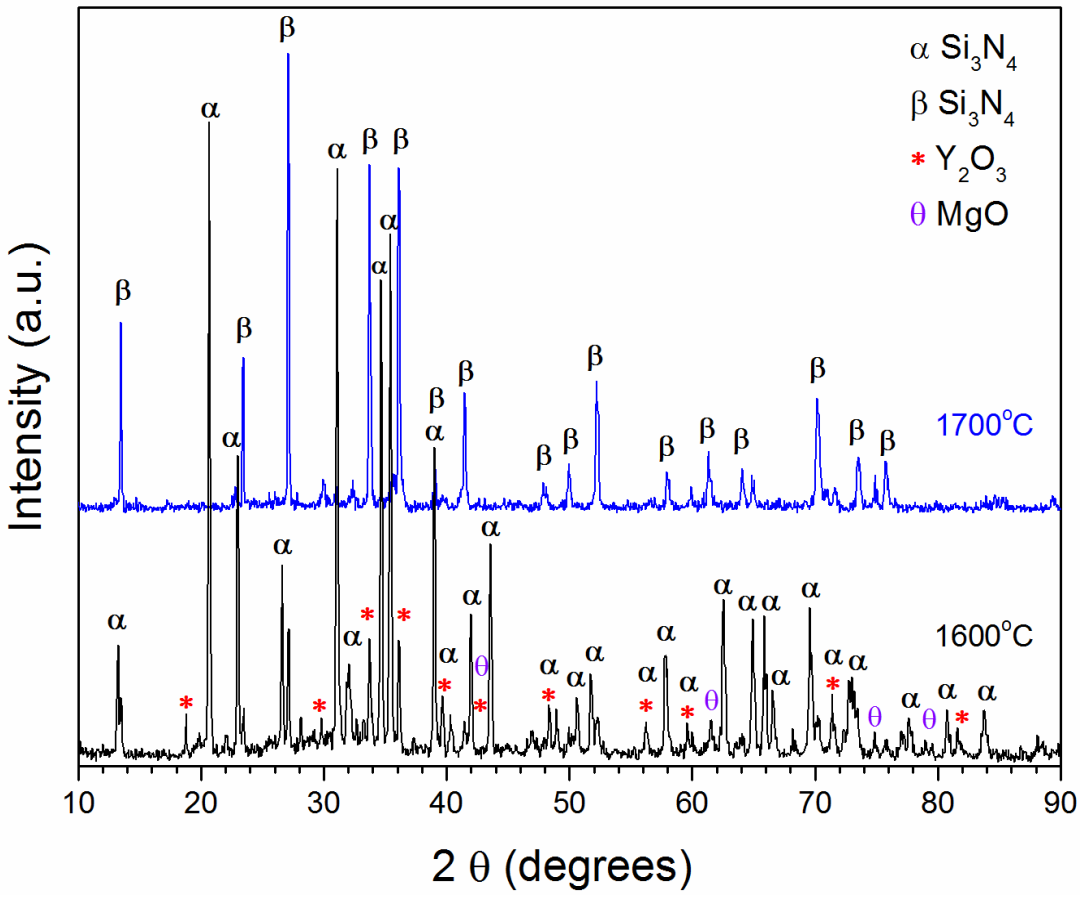

Fig. 4.5. XRD patterns for SN-5YM35 methylcellulose foams containing 5 wt% Y_2O_3 and 5 wt% MgO. (ICSD α–Si_3N_4 # 041-0360, β–Si_3N_4 # 033-1160, Y_2O_3 # 043-0661, MgO # 045-0946).

Figure 4.6 presents SEM images of the Si_3N_4 methylcellulose foams prepared with 30 and 35 vol% of solids concentration and sintered at high temperature. Gelcasting foams featuring similar interconnected network of spherical cell morphology and presenting typical rod-like β–Si_3N_4 grains. Note that when the temperature is increased up to 1700 °C the amount of porosity of the SN-5YM30 methylcellulose foams decreased from ~89 to ~81vol% (see Table 4.1), since the α→ β transformation takes place without much densification [25]. In addition, the average cell size slightly decreased with the sintering temperature around 450 (D_{10}), 773 (D_{50}) to 1354 μm (D_{90}), and also window size around 57 (D_{10}), 152 (D_{50}) to 274 μm (D_{90}), see Table 4.1. Similar influence of the temperature on the amount of porosity of the SN-5YM35 methylcellulose foams that decreased from ~83 to ~72 vol% (see Table 4.1). Note also a presence of a wide distribution of cell sizes around 387 (D_{10}), 544 (D_{50}) to 718 μm (D_{90}), and window size around 66 (D_{10}), 108 (D_{50}) to 147 μm (D_{90}), see Table 4.1. A general view of the interlocking of β–Si_3N_4 grains present on cell walls

and struts of the SN-5YM30 methylcellulose foams, is reported in Fig. 4.6 a), and b) higher magnification of β–grains which exhibit aspect ratio around ~7.0 ± 0.9. While a slightly decrease on aspect ratio (~6.0 ± 2.0), is observed for SN-5YM35 methylcellulose foams, see Fig. 4.6 c) general feature, and d) higher magnification of the elongated β–Si_3N_4 grains. Note that the aspect ratio slightly decreases with the solid concentration, as the anisotropic growth of β–grains became restrained when the porosity decreased [34]. Therefore, the rate of α→β transformation is increased with heat temperature which enable the solution of α–Si_3N_4 into the amorphous liquid Y_2O_3-MgO-containing phase and subsequently precipitation of β–Si_3N_4 (less soluble and more stable) resulting in the formation of elongated interlocking β–grains [33].

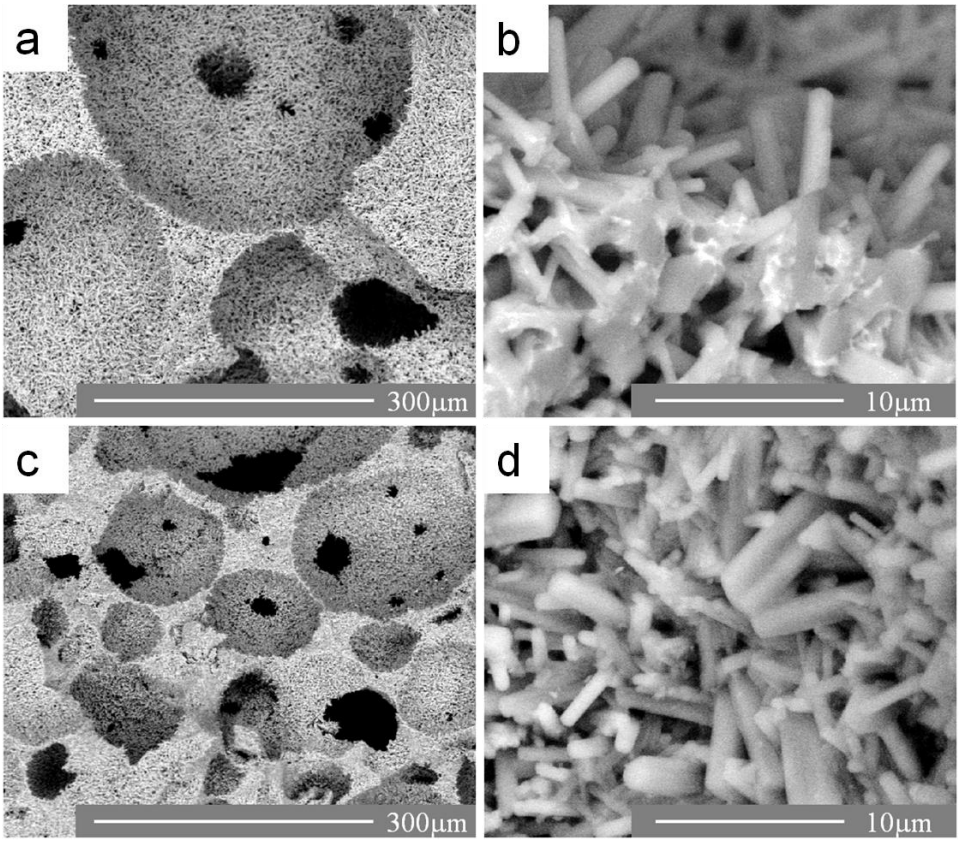

Fig. 4.6. SEM images of the fracture surface of Si_3N_4 sintered methylcellulose foams: 30 vol% of solid concentration a) general feature and b) higher magnification (detail of interlocking β–grains); 35 vol% of solid concentration c) general view and d) higher magnification (detail of interlocking β–grains).

Peng et al. [35] suggested that the ratio of the cell window (*d*) to cell diameter (*D*) is directly related to the pore volume fraction in the case of a face centered cubic array of cells of uniform diameter, and this allows to quantitatively compare different cellular microstructures. It is important to note that the permeability, hence the flow rate, is very dependent on the pore size and pore volume [36].

The ratio *d/D* was plotted in Figure 4.7 for gelcasting foams produced using different gel formers as function of pore volume fraction, *Vp*, calculated according to equation (4.2), suggested by Peng et al. [35]:

$$V_P = \frac{\pi}{\sqrt{2}}\left[\frac{3}{1-k^2} - \frac{5}{3}\left(\frac{1}{\sqrt{1-k^2}}\right)^3 - 1\right] \tag{4.2}$$

where $k = d/D$. Note that for cellular ceramics, $0.7 < V_p < 1.0$ [37].

The calculated total porosity values (V_p) show differences related to those measured from the weight-to-volume ratio for all gelcasting foams, with exception of the egg white albumen, which is more efficient to stabilize the foam due to a formation of a cohesive film at air-water interface (see Table 4.1). While agar and methylcellulose foams are more susceptible to the destabilization mechanisms: coalescence and Ostwald ripening, allowing a wide distribution of cells and windows sizes.

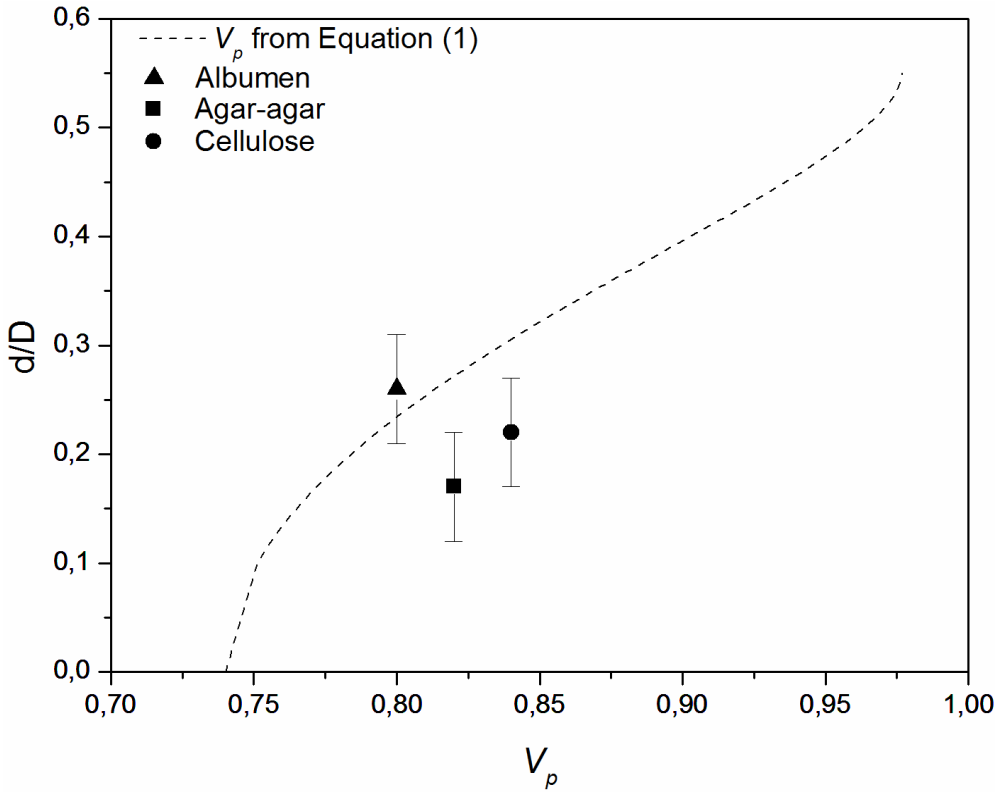

Fig. 4.7 The ratio *d/D* as a function of the pore volume fraction, V_p, for Si_3N_4 sintered gelcasting foams.

Compressive strength as a function of total porosity is reported in Figure 4.8 for gelcasting foams produced with different gelling agents and containing 30 or 35 vol% of solids concentration. The values increased from ~2 to ~9 MPa, when porosity decreased from ~89 to ~79 vol% (see Table 4.1). Higher values of strength are associated with egg white albumen, which is more efficient to stabilize the foam. According to Clark et al., [30] during surface denaturation the interaction between neighboring molecules enables formation of a cohesive viscoelastic surface layer of uniform thickness that makes desorption of proteins molecules highly improbable. Afterward, agar foam which is able to fast consolidation of foam and suitable gel strength by the formation of hydrogen bonds with water molecules, and methylcellulose (labeled cellulose) macromolecules that form viscous adsorbed layers at liquid–interfaces, though they form poor-gel strength leading to coalescence of the foam, both foams were prepared with 30 vol% of solids concentration. In addition, varying the solids concentration to 35 vol% for methylcellulose foams (labeled as cellulose*), we observed an increasing in the compressive strength ~7.5 MPa (see Table 4.1), due to decrease in porosity and strong packing of Si_3N_4 particles on the cell walls and struts.

The variation in density and strength among samples processed using different gel formers reflects the differences between thermal gelling, and indeed leads to the design of a wide range of microstructures concerning to cell and windows sizes and porosity.

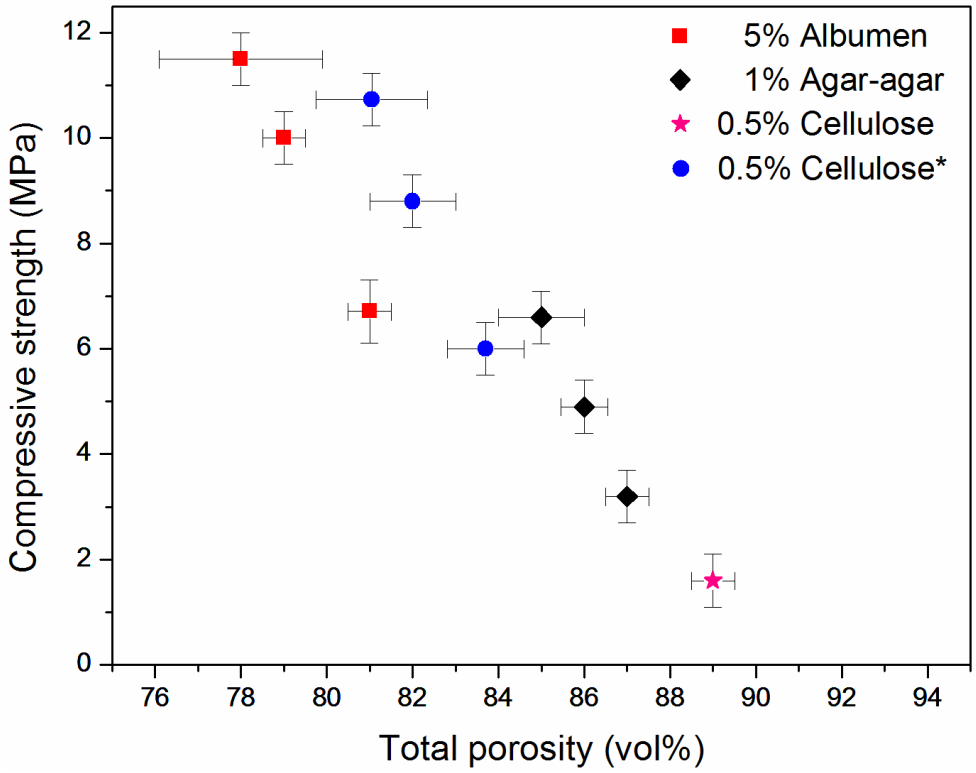

Fig.4.8 Compressive strength of sintered SN-5YM30 gelcasting foams (egg white albumen, agar-agar and methylcellulose (labeled as cellulose)), as a function of total porosity. The symbol (*) represents SN-5YM35 methylcellulose foam.

The development of ~98% β–Si_3N_4 elongated rod-like grains with the increasing heat temperature up to 1700 °C, as already outlined, clearly influences the strength by means of increased degree of bonding between grains, since with increasing sintering temperature diffusion is enhanced, as well toughness mechanisms grain bridging and pullout. A significant increase in the compressive strength values was obtained for SN-5YM30 methylcellulose foams from ~2 to about ~ 8 MPa (see Table 4.1), with the increase of sintering temperature. Moreover, we observed higher values for foams prepared with 35 vol% of solids concentration, as ~7.5 up to ~33.5 MPa (see Table 4.1), with the increasing of sintering temperature up to 1700 °C, which indicates that fine-sized, fibrous Si_3N_4 grains favor high strength in porous Si_3N_4 ceramics [38].

Table 4.1 Summary of the physical properties of the Si_3N_4 foams from gelcasting process.

Si_3N_4 foams	*d_{50} Cell size, D [a] (μm)*	*Cell window size, d (μm)*	*Total Porosity[b] (vol%)*	*d/D*	*V_P [c]*	*σ Compressive strength (MPa)*
Conventional Pressureless Sintering 1600°C, N_2 flow						
5 wt% Albumen	199 ± 14	51 ± 6	79.1 ± 1.2	0.256	0.811	9.4 ± 2.0
1 wt% AGAR	456 ± 47	79 ± 18	86.1 ± 0.9	0.173	0.773	5.0 ± 1.1
30 vol% Methylcellulose	852 ± 89	152 ± 36	89.3 ± 0.5	0.222	0.794	1.6 ± 0.5
35 vol% Methylcellulose	643 ± 69	109 ± 32	83.0 ± 1.1	0.169	0.772	7.5 ± 2.1
Conventional Pressureless Sintering 1700°C, Static N_2						
30 vol% Methylcellulose	773 ± 88	152 ± 30	81.4 ± 0.5	0.183	0.777	8.1 ± 1.0
35 vol% Methylcellulose	544 ± 35	108± 8	72.0 ± 1.0	0.159	0.768	33.5 ± 3.9

[a] Cumulative cell size distribution, d_{50}, measured from SEM images using linear intercept method.

[b] Calculated by assuming that the theoretical density of Si_3N_4 ceramic is 3.2 g·cm^{-3}.

[c] Pore volume fraction, V_P, determined.

Figure 4.9 shows typical permeability curves (pressure drop versus air velocity), tested in argon at room temperature for Si_3N_4 gelcasting foams using egg white albumen or agar. The resistances to flow of the samples slightly differ for different gel formers and exhibit the parabolic trend proposed by Forchheimer's Eq. (4.1), the constants k_1 and k_2 (see Table 4.2) adjust reasonable with experimental pressure drop curves and present correlation coefficient (R^2) greater than 0.988 for albumen curve and 0.999 for agar curve. However, a certain dispersion of $\Delta P/L$ as a function of v_s was observed for gelcasting foams using egg white albumen as gel former. Indeed, agar foams present larger channels than those present in albumen foams. Also, tortuosity that arises from cell-size variation can affect the permeability constants k_1 and k_2 e.g., if the cell sizes of the foam are constant, permeability is well correlated to porosity [39]. Typical fluid velocity in aerosol filtration is lower than 10 $cm \cdot s^{-1}$, here the tested air velocity range from 0 to 0.80 $m \cdot s^{-1}$.

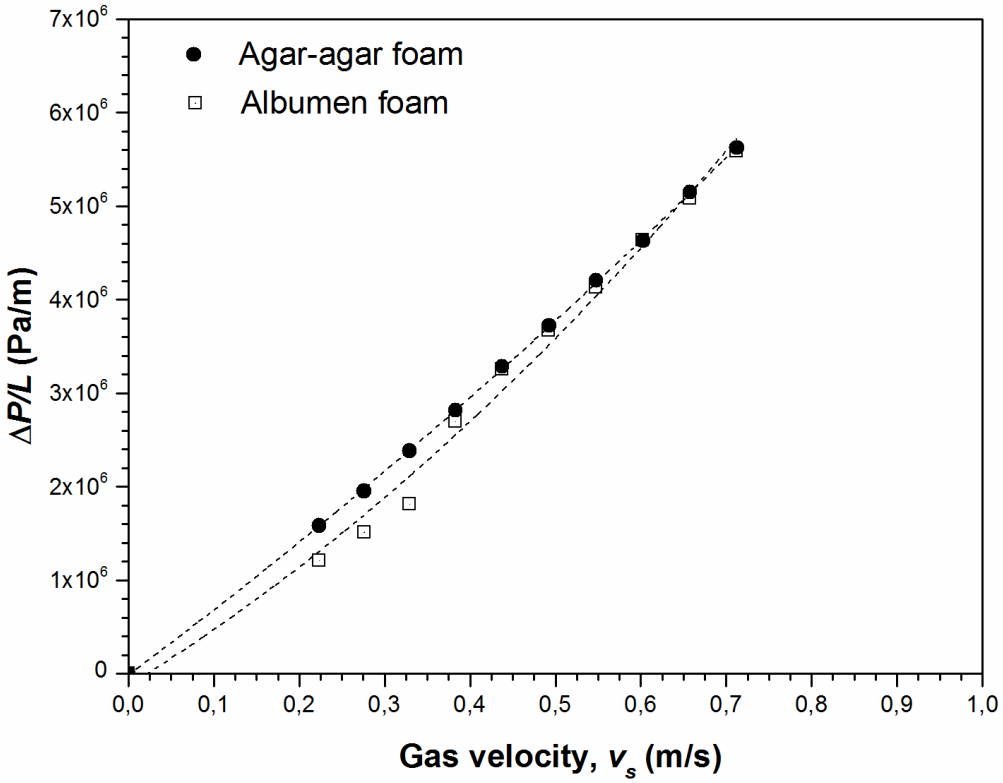

Fig. 4.9. Pressure drop curves obtained at room temperature for Si_3N_4 sintered gelcasting foams.

Table 4.2 Summary of the constants k_1 and k_2 obtained by fitting the pressure drop curves with Forchheimer's Equation for the Si_3N_4 foams from gelcasting process.

Si_3N_4 gelcasting foams			
Egg white albumen 1600 ^oC	***T^oC***	***$k_1(m^2)$***	***$k_2(m)$***
	R.T	4.41E-12	4.01E-07
Agar-agar foam 1700 ^oC	R.T	3.30E-12	1.02E-06

4.4 Conclusions

Gelcasting of biopolymers enable manufacture highly interconnected Si_3N_4 ceramic foams with total porosities in the between of ~79 to 89vol%, as well a wide range of cells and windows sizes. Different biopolymers were used that gave significantly differences in strength values ranged from ~2 to ~9 MPa when sintered at 1600 °C. With the increasing in the sintering temperature up to 1700 °C, we observe the development of elongated β–grains that strongly influence the strength that increased to ~33 MPa, for SN-5YM35 methylcellulose foams. Permeability evaluation shows that Si_3N_4 gelcasting foams using egg white albumen or agar as gel formers are suitable for filtering application.

References

[1] Green DJ, Colombo P. Cellular ceramics: intriguing structures, novel properties, and innovative applications. *Mrs Bull* 2003;**28**(4)296–300.

[2] Scheffler M, Colombo P. Cellular ceramics: structure, manufacturing, properties and application. Weinheim: Wiley-VCH; 2005.

[3] Studart AR, Gonzenbach UT, Tervoort E, Gauckler LJ. Processing routes to macroporous ceramics - A review. *J Am Ceram Soc* 2006;**89**(6):1771–89.

[4] Sepulveda P, Binner JGP. Processing of cellular ceramics by foaming and *in situ* polymerisation of organic monomers. *J Eur Ceram Soc* 1999;**19**(12):2059–66.

[5] Díaz A, Hampshire S. Characterisation of porous silicon nitride materials produced with starch. *J Eur Ceram Soc* 2004;**24**(2):413–19.

[6] Ziegler G, Heinrich J, Wötting G. Relationships between processing, microstructure and properties of dense and reaction-bonded silicon nitride. *J Mater Sci* 1987;**22**(9):3041–86.

[7] Ling G, Yang H. Pressureless sintering of silicon nitride with magnesia and yttria. *Mater Chem Phys* 2005;**90**(1):31–34.

[8] Alper AM. Phase diagrams in advanced ceramics. London: Acad Press Ltd; 1995.

[9] Lange H, Wötting G, Winter G. Silicon nitride-from powder synthesis to ceramic materials. *Angew Chem Int Engl* 1991;**30**(12):1579–97.

[10] Zhu X, Sakka Y. Textured silicon nitride: processing and anisotropic properties. *Sci Technol Adv Mater* 2008;**9**(3):033001.

[11] Moreno R, Salomoni A, Castanho SM. Colloidal filtration of silicon nitride aqueous slips, part I: optimization of the slip parameters. *J Eur Ceram Soc* 1998;**18**(4):405–16.

[12] Nangrejo MR, Bao X, Edirisinghe MJ. Preparation of silicon carbide-silicon nitride composite foams from pre-ceramic polymers. *J Eur Ceram Soc* 2000;**20**(11):1777–85.

[13] Yu J, Yang J, Li H, Xi X, Huang Y. Study of particle-stabilized Si_3N_4 ceramic foams. *Mater Lett* 2011;**65**(12):1801–04.

[14] Moraes EG, Colombo P. Silicon nitride foams from emulsions. *Mat Lett* 2014;**128**:128–31.

[15] Huang Y, Ma L, Tang Q, Yang J, Xie Z, Xu X. Surface oxidation to improve water-based gelcasting of silicon nitride. *J Mater Sci* 2000;**35**(14):3519–24.

[16] Lyckfeldt O, Brandt J, Lesca S. Protein forming—a novel shaping technique for ceramics. *J Eur Ceram Soc* 2000;**20**(14), 2551–59.

[17] Potoczek M. Gelcasting of alumina foams using agarose solutions. *Ceram Int* 2008;**34**(3), 661–67.

[18] Nieto MI, Santacruz I, Moreno R. Shaping of Dense Advanced Ceramics and Coatings by Gelation of Polysaccharides. *Adv Eng Mater* 2014;**16**(6):637–54.

[19] Tuck C, Evans JRG. Porous ceramics prepared from aqueous foams. *J Mater Sci Lett* 1999;**18**(13), 1003–05.

[20] Blanchard CR, Schwab ST. X-ray diffraction analysis of the pyrolytic conversion of perhydropolysilazane into silicon nitride. *J Am Ceram Soc* 1994;**77**(7):1729–39.

[21] Ortega FS, Sepulveda P, Innocentini MDM, Pandolfelli VC. Surfactants: a necessity for producing porous ceramics. *Am Ceram Soc Bull* 2001;**80**(4): 37–42.

[22] Innocentini MDM, Faleiros RK, Pisani JR, Thijs I, Luyten J, Mullens S. Permeability of porous gelcast scaffolds for bone tissue engineering. *J Porous Mater* 2010;**17**(5):615–27.

[23] Biasetto L, Colombo P, Innocentini MDM, Mullens S. Gas permeability of microcellular ceramic foams. *Ind Eng Chem Res* 2007;**46**(10):3366–72.

[24] Innocentini MDM, Rizzi JAC, Nascimento LA, Pandolfelli VC. The pressure-decay technique for air permeability evaluation of dense refractory ceramics. *Cem Concr Res* 2004;**34**(2):293–98.

[25] Hampshire S, Jack KH. Densification and transformation mechanisms in nitrogen ceramics. In: Riley FL, editor. Progress in nitrogen ceramics. Lancaster: Martinus Nijhoff publ;1983. 225–30.

[26] Pyzik A, Beaman D. Microstructure and properties of self-reinforced silicon nitride. *J Am Ceram Soc* 1993;**76**(11):2737–44.

[27] Bae S, Baik S. Critical concentration of MgO for the prevention of abnormal grain growth in alumina. *J Am Ceram Soc* 1994;**77**(10):2499–504.

[28] Tan CY, Yaghoubi A, Ramesh S, Adzila S, Purbolaksono J, Hassan MA, Kutty MG. Sintering and mechanical properties of MgO-doped nanocrystalline hydroxyapatite. *Ceram Int* 2013;**39**(8):8979–83.

[29] Dickinson E. Protein adsorption at liquid interfaces and the relationship to foam stability. In: Wilson AJ, editor. Foams: physics, chemistry and structure. Heidelberg: Springer-Verlag; 1989. 39–53.

[30] Clark DC, Coke M, Smith LJ, Wilson DR.The formation an d stabilisation of protein foams. In: Wilson AJ, editor. Foams: physics, chemistry and structure. Heidelberg: Springer-Verlag; 1989. 55–68.

[31] Dickinson E. Hydrocolloids at interfaces and the influence on the properties of dispersed systems. *Food hydrocoll* 2003;**17**(1):25–39.

[32] Bibette J, Leal Calderon F, Poulin P. Emulsions: basic principles. *Rep Prog Phys* 1999;**62**(6):969.

[33] Park JY, Kim CH. The α–to β–Si_3N_4 transformation in the presence of liquid silicon. *J Mater Sci* 1988;**23**(9):3049–54.

[34] Zou C, Zhang C, Li B, Wang S, Cao F. Microstructure and properties of porous silicon nitride ceramics prepared by gel-casting and gas pressure sintering. *Mater & Des* 2013;**44**(1):114–18.

[35] Peng HX, Fan Z, Evans JRG, Busfield JJC. Microstructure of ceramic foams. *J Eur Ceram Soc* 2000;**20**(7):807–13.

[36] Nettleship I. Applications of porous ceramics. *Key Eng Mater* 1996;**122**:305–24.

[37] Gibson LJ, Ashby MF. Cellular Solids: Structure and Properties. 2nd edition. Cambridge: Cambridge University Press; 1999.

[38] Yang JF, Deng ZY, Ohji T. Fabrication and characterisation of porous silicon nitride ceramics using Yb_2O_3 as sintering additive. *J Eur Ceram Soc* 2003;**23**(2):371–78.

[39] Innocentini MDM, Sepulveda P, Ortega FS. Permeability. In: Scheffler M, Colombo P, editors. Cellular ceramics: structure, manufacturing, properties and applications. Weinheim: Wiley-VCH; 2005.313–41.

5. Ti_2AlC foams produced by gelcasting

M. Potoczek, E. G. de Moraes and P. Colombo, "Ti_2AlC foams produced by gel-casting", manuscript submitted.

5.1 Introduction

MAX phases are nano-layered ceramics with the general formula $M_{n+1}AX_n$ (n = 1-3), where M is an early transition metal, A is an A group element, and X is either carbon and/or nitrogen [1,2].These materials exhibit a unique combination of characteristics typical of both ceramics and metals [3–5]. Like ceramics, they have low density, low thermal expansion coefficient, high modulus and high strength, and good high-temperature oxidation resistance. Like metals, they are good electrical and thermal conductors, readily machinable, tolerant to damage, and resistant to thermal shock. The combination of both metallic and ceramic properties of Ti_2AlC and other MAX phases originates partially from the metallic nature of the bonding, and partially from their layered structure. This feature makes them promising for many applications such as electrical heating elements [6] gas burner nozzles in corrosive environments, high temperature bearings [7], cladding materials in lead-cooled fast-breeder nuclear reactors [8], high temperature electrodes [9], etc.

MAX phases can be produced both in dense and in porous form. In spite of abundant literature on processing, structure and properties of Ti_2AlC and the rest of the MAX phases in dense form, there is few experimental data published on the Ti_2AlC in the porous form [10–17]. Porous MAX phases need systematic studies, because control of the porosity and pore size can be used to tailor their functional properties. For example, Sun at al. [17] fabricated porous Ti_3AlC_2 as a support for CeO_2 nanostructured catalyst for gas exhaust. Moreover porous MAX phases were used as preforms for metal (Mg) melt infiltration in order to produce high-strength MAX phases/Mg composites [18-20]. Ti_2AlC/nanocrystalline Mg–matrix composite exhibited higher strength levels in both tension (350 ± 40 MPa) and compression (700 ± 10 MPa) than other Mg composites, as well as exceptional damping capabilities [18].

The aim of our work was the fabrication of highly porous (~90%) Ti_2AlC foams possessing a high degree of interconnected porosity. We selected Ti_2AlC because it is one of the most studied compounds, possessing the beneficial combination of all properties typical of MAX phases. Cellular structures with optimized morphology based on Ti_2AlC would possess high permeability, high specific/geometric surface area, high refractoriness, chemical resistance and good mechanical

properties. These characteristics would enable these foams to be widely used in several industrial applications such as hot gas filters, solid/liquid separation devices, catalyst supports and thermal insulators [21]. Moreover, Ti_2AlC foams would be able to further expand the range of potential applications in devices where high thermal shock resistance, high permeability and electrical conductivity are required. For instance, the possibility of Joule heating of the MAX phase-based porous components would make them very attractive as catalyst support.

Porous MAX phases reported in the literature so far were manufactured using one of three techniques: (1) incomplete densification during sintering of MAX phase powders or reaction sintering of elemental powders [10,14], (2) pore former method using NaCl as the pore former, which was dissolved after cold pressing but before pressureless sintering at 1400 °C [15,16], and (3) the replica template method from the highly dispersed aqueous suspension using polyurethane sponges as a template [17].The porosity range obtained by the first two methods was below 75 vol% [10,16], while higher porosity (80 vol%) was obtained by the replica template method [17]. However, one of the problems of the replica template method is that the ceramic struts are hollow, due to volatilization of the organic filament used as substrate [22,23]. This internal void and the flaws present on outer surface due to the difficulty in homogeneously coating the polyurethane foam template leads to the very low mechanical strength levels that characterize this type of structure. On the other hand, direct foaming followed by consolidation of the wet foam by gel-casting leads to higher strength than replica foams at the same porosity level, although typically the components possess a somewhat lower permeability [22]. Gel-casting of porous materials was developed as a result of the combination of the gel-casting process and the aeration of ceramic suspensions [24]. Wet foams stabilized by surfactants require a gelling agent to consolidate the foam microstructure before extensive coalescence and disproportionation take place. The in situ polymerization of organic monomers or biopolymers, as gelling agents, leads to fast solidification, resulting in highly porous bodies with homogeneous morphology [24,25]. In this work an environmentally friendly biopolymer (agarose) was used as a gelling agent, as already proposed in the literature for other ceramic compositions using polysaccharides [25–28] or proteins [29–31] as gelling agents.

5.2 Experimental procedure

Preparation of Ti_2AlC foams

Ceramic suspensions of Ti_2AlC powder (Maxthal−211 powder, d_{50} = 5.4 μm, Sandvik Italia S.p.A., Milan, Italy) were prepared with a solid loading of 35 vol% by dispersing them with 1.0 wt% of polyacrylic acid (Aldrich, Cat. No. 323667). Their homogenization was carried out by planetary milling using alumina balls and jar. Agarose solutions (3.0 and 4.0 wt%) were prepared by mixing agarose powder (MEEO Ultra-Qualitat, Roth, Germany) with distilled water followed by heating for 1 hour at 95°C. The 3.0 and 4.0 wt% agarose solutions were added in equal quantities to the 35 vol% Ti_2AlC slurries maintaining the temperature of all constituents at 60-65 °C. The final Ti_2AlC content in the suspensions was always 25.7 vol% (58.7 wt%). The total concentrations of active gelling matter in the final slurries were 0.75 and 1.00 wt% with respect to the dry ceramic powder, corresponding to 1.07 and 1.42 wt% of agarose with respect to water. Foaming was carried out at 60 °C through agitation using a double-blade mixer at velocity of 600 rpm for 5 min. A non-ionic surfactant (Tergitol TMN-10, Aldrich) was added to stabilize the foams at a concentration of 0.34 g/100 ml of slurry in all cases. The foamed suspension containing agarose was then poured into a mould and the mould was cooled down using flowing cold water (15 °C) to gel the wet foam. The green bodies were then de-moulded and left in room conditions to dry. Sintering was performed in flowing argon atmosphere (99.99% Ar) at temperatures ranging from 1300 to 1400 °C with 4 h soaking time using heating rate of 1°C/min to 650 °C and then 2 °C/min up to sintering temperature. In order to limit the decomposition of the Ti_2AlC phase occurring during the high temperature heat treatment (see later), foam samples were placed in an alumina boat on a bed of an Al-containing compound powder (we chose Ti_3AlC_2), as suggested by Lu at al. [32]. Samples were also heated in a wider temperature range (from 1000 to 1600 °C) without the Ti_3AlC_2 powder bed, for comparison.

Characterization of sintered foams

The phase assemblage of the raw powders and sintered ceramics was assessed by X-ray diffraction analysis (Bruker-AXS D8, Karlsruhe, Germany). XRD measurements were performed on finely ground foams using monochromatic Cu $K\alpha$ radiation within 2θ range of 8 - 85° with a step size of 0.05° and step time of 2s. Phase identification was performed using Match software package (Crystal Impact GbR, Bonn, Germany) supported by ICDD PDF-2 Powder Diffraction File. Phase quantification was carried out by the method developed by Wang et al. [33] for quantitative phase

analysis in the Ti-Al-C ternary system. According to the method, non overlapping diffraction peaks were used: the (004) peak at 2θ = 19.25º for Ti_3AlC_2, the (002) peak at 13.0º for Ti_2AlC and the (111) peak at 2θ = 35.9º for TiC.

The mass fractions of Ti_3AlC_2, Ti_2AlC and TiC denoted as W_a, W_b and W_c were determined using the following equations [33].

$$W_a = \frac{I_a}{I_a + 0.22I_b + 0.084I_c} \tag{5.1}$$

$$W_b = \frac{I_b}{4.545I_a + I_b + 0.382I_c} \tag{5.2}$$

$$W_c = \frac{I_c}{11.905I_a + 2.619I_b + I_c} \tag{5.3}$$

where I_a, I_b and I_c is the intensity of following peaks: (004) for Ti_3AlC_2, (002) for Ti_2AlC, and (111) for TiC.

The relative density and open porosity were determined by water immersion method using Archimedes' principle, as specified in ASTM C20-00. The theoretical density of fully densified Ti_2AlC (4.11 g·cm^{-3}) was used as a reference to calculate the total volume fraction of porosity.

The microstructure of the produced foams was observed by scanning electron microscopy (SEM), (FEI Quanta 200, Milan, Italy), and the average cell and cell window size was measured by the linear intercept method (ASTM E112-12) using an image analysis program (Axio Vision LE). When the cells are spherical and uniformly distributed, according to ASTM D3576-98, the relationship between the average measured chord length l and the average sphere diameter D is: $D = 1.623 \cdot l$.

The compressive strength was measured by uniaxial compression (1121 UTM, Instron, Norwood, MA, USA) according to the ASTM C133-97 standard. The crosshead speed was 1.0 mm·min^{-1} and the compressive load was 5 kN. Specimens with a nominal size of 10 mm × 10 mm × 10 mm were cut from larger bodies (disks of 4 cm diameter and 1.5 cm height). In all mechanical determinations results were based on average of five samples for each density.

The permeability of Ti_2AlC foams was performed at ambient temperature in a laboratory device [34] using argon as flowing medium. Permeability constants were fitted from Forchheimer's equation, expressed for the flow of compressible fluids as [34,35]:

$$\frac{P_i^2 - P_o^2}{2P_oL} = \frac{\mu}{k_1}v_S + \frac{\rho}{k_2}v_S^2 \quad (5.4)$$

in which P_i and P_o are, respectively, the absolute gas pressures at the entrance and exit of the sample; v_s is the superficial fluid velocity, determined by $v_s = Q/A$, where Q is the volumetric flow rate and A is the exposed surface area of the porous medium perpendicular to the flow direction; L is the sample's thickness (0.7 - 1.2 cm); μ is the gas viscosity ($2.24 \cdot 10^{-5}$ Pa s); ρ is the gas density (1.652 kg·m^{-3}), evaluated for P_o = 760 mmHg and T = 24 °C. The parameters k_1 and k_2 are usually known as Darcian and non-Darcian constants, in reference to Darcy's law [35,36].

5.3 Results and discussion

After the heat treatment at high temperature, the change in the phase composition of Ti_2AlC powders is predominately caused by the decomposition of Ti_2AlC to Ti_3AlC_2 according to the following reaction (5.5) [37]:

$$2Ti_2AlC\ (s) \rightarrow Ti_3AlC_2\ (s) + TiAl_{1-x} + xAl\ (g\ or\ l) \quad (5.5)$$

where $x \leq 1$. The composition of $TiAl_{1-x}$ in Reaction (5.5) depends on how much Al is lost to the surroundings [37], with the extreme situation being when Al is totally lost as a gaseous or liquid phase and only pure Ti remains. In highly porous foam, decomposition according to Reaction (5.5) must be even more severe when compared to fully dense samples, because the high surface area allows for faster loss of Al. Apart from the heat treatment, another factor that influences the phase composition of Ti_2AlC foam is the presence or not of a Ti_3AlC_2 powder bed during sintering. As an example, the X-ray patterns for the as received Ti_2AlC powder as well as for a Ti_2AlC foam after sintering at 1400 °C with and without a Ti_3AlC_2 powder bed are presented in Figure 5.1. The patterns of both initial powder and the sintered foams showed Ti_2AlC, Ti_3AlC_2 and TiC phases. Additionally, Al_2O_3 was detected in the initial powder as impurity, but it was not considered when carrying out the XRD quantitative analysis. The decrease in the Ti_2AlC phase when the heat treatment was carried out without a Ti_3AlC_2 powder bed is clearly observable.

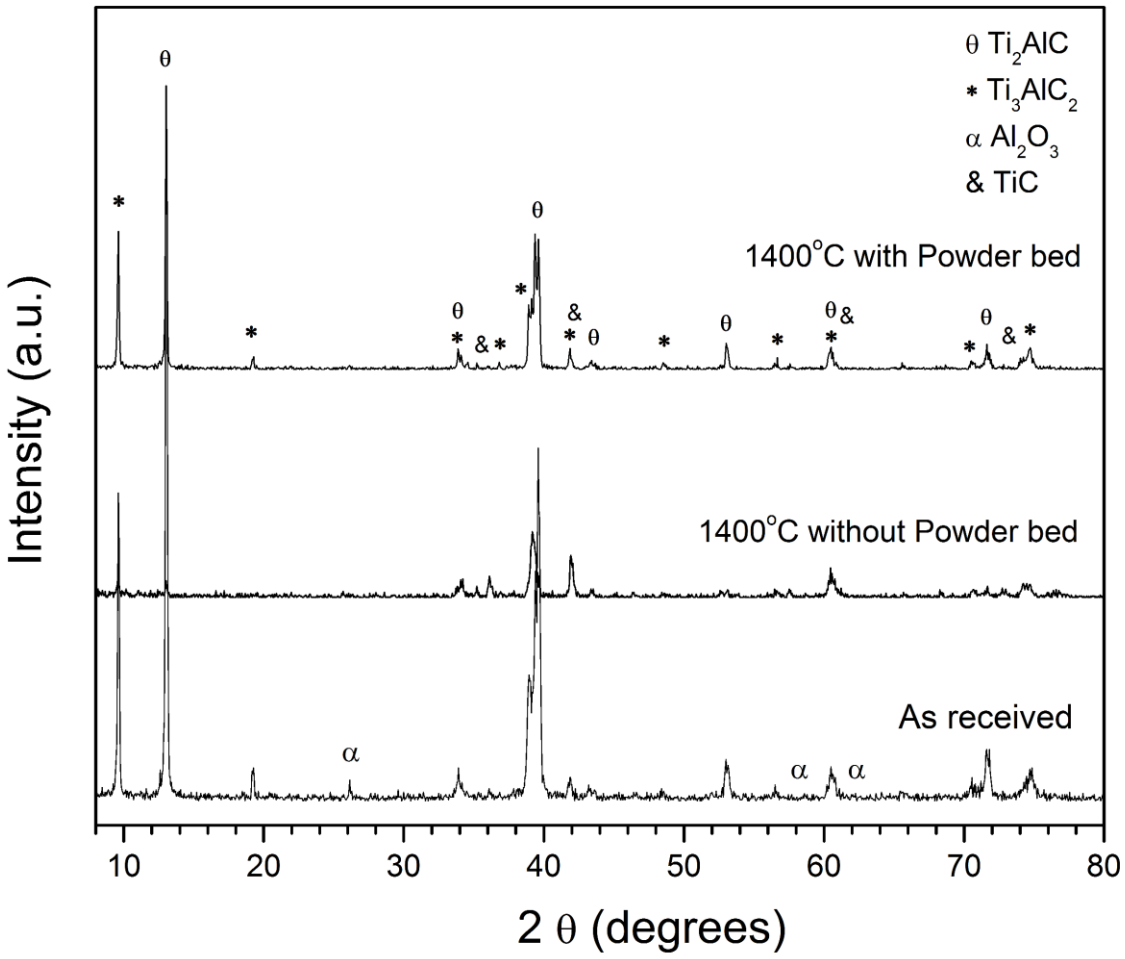

Fig 5.1. XRD diffraction patterns for the as-received Ti_2AlC powder and of a Ti_2AlC foam, sintered at 1400 ºC with or without a Ti_3AlC_2 powder bed. (ICSD collection code: Ti_2AlC # 165460, Ti_3AlC_2 # 153266, TiC # 44494, respectively).

Figure 5.2 shows the effect of heat treatment on the decomposition of the Ti_2AlC phase, according to Reaction (5.5), for foam samples heated without (temperature range 1000-1600 °C) or with Ti_3AlC_2 powder bed (temperature range 1300-1400 °C). We can observe that the initial Ti_2AlC powder already contained some impurities and that the decomposition started at around 1300 °C and proceeded very significantly with increasing temperature when no Ti_3AlC_2 powder bed was present.

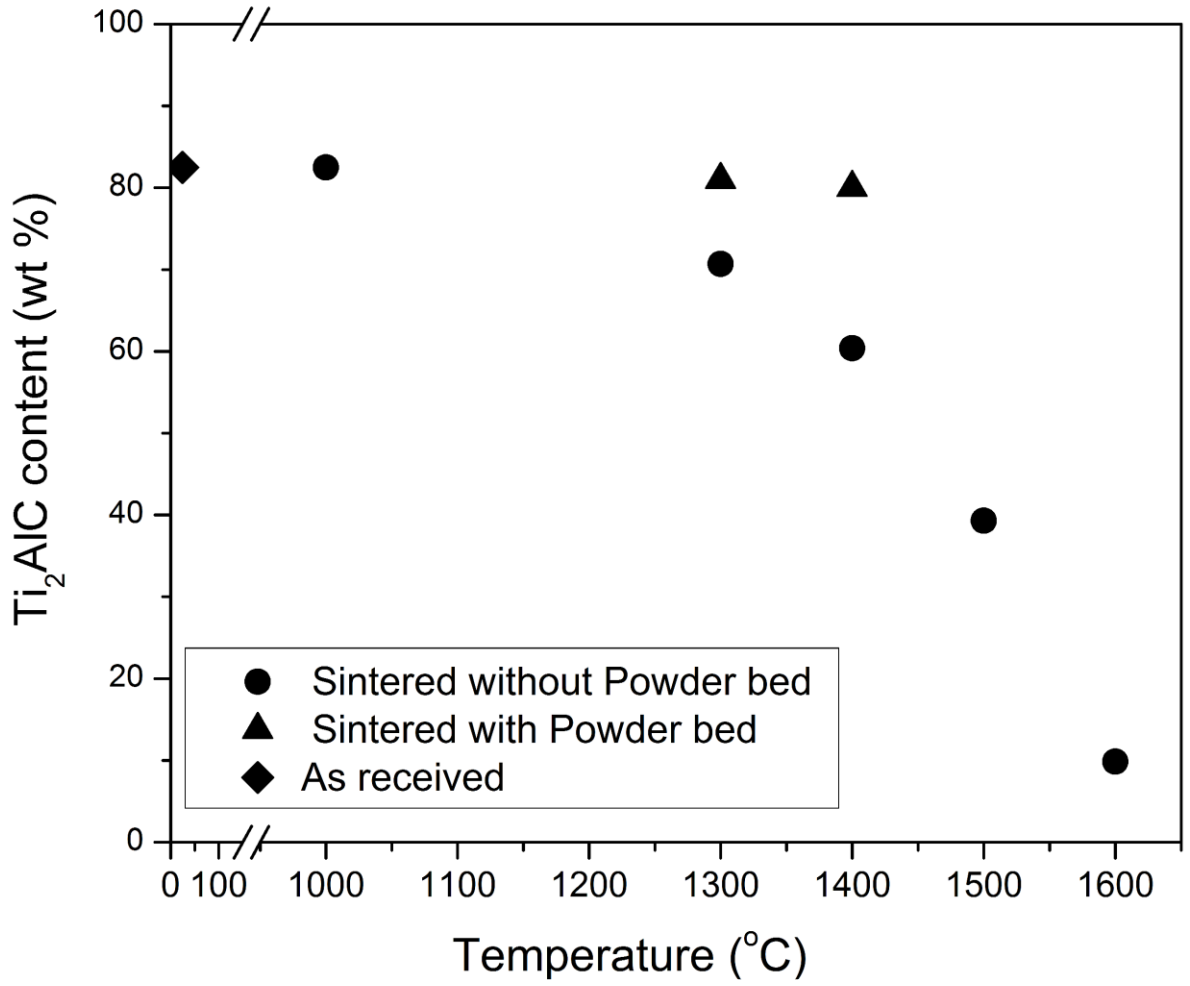

Fig 5.2. Effect of heat treatment on the amount of residual Ti_2AlC phase for foams sintered at different temperatures, with or without a Ti_3AlC_2 powder bed.

Table 5.1 reports the mass fractions of Ti_2AlC, Ti_3AlC_2 and TiC, as computed from Eqs. 5.1-5.3, in the initial powder as well as in the foams after sintering at 1300 and 1400 °C with or without a Ti_3AlC_2 powder bed. The results clearly show the beneficial effect of the presence of a Ti_3AlC_2 powder bed for the retention of the Ti_2AlC phase even when processing highly porous components with a large surface area. Although a high content of Ti_2AlC was found after sintering at 1300 °C using a Ti_3AlC_2 powder bed, the ceramic foam had a poor compression strength (0.76 ± 0.18 MPa for a total porosity of 90 vol% and bulk density of 0.41 $g \cdot cm^{-3}$) due to incomplete densification of the struts. On the other hand, the Ti_2AlC content after sintering at 1400 °C using a

Ti_3AlC_2 powder bed was found to be 80 wt%. Therefore, sintering of foams presented in next sections of this work was performed only at 1400 °C using a Ti_3AlC_2 powder bed.

Table 5.1 XRD quantitative analysis results of the initial powder as well as of Ti_2AlC foams after sintering at 1300 and 1400 °C, using a Ti_3AlC_2 powder bed and without powder bed.

Sample	Phase amount (wt%)		
	Ti_2AlC	Ti_3AlC_2	TiC
As-received Ti_2AlC powder	82.5	17.0	0.5
Foam after sintering at 1300 °C, without powder bed	71.5	16.8	11.7
Foam after sintering at 1300 °C, using powder bed	81.0	16.2	2.8
Foam after sintering at 1400 °C, without powder bed	69.8	17.7	12.5
Foam after sintering at 1400 °C, using powder bed	80.0	15.5	4.5

When discussing the phase assemblage of the heat treated foams, we should also point out that we used an agarose concentration that was not higher than 1 wt%, with respect to the ceramic powder, in order to minimize the reaction of the organic additive with the MAX phase, forming binary carbides during the high temperature heat treatment. Thermogravimetric analysis data for the agarose binder (not shown here for the sake of brevity) indicate that after a high heat temperature treatment in argon there is a 20 wt% residue, e.g. the final content in the ceramic foams after agarose decomposition was not higher than 0.2 wt% with respect to the ceramic powder.

The linear sintering shrinkage of the porous samples was in the 10–12% range. Total porosity, open porosity, water absorption and density of Ti_2AlC foams after sintering at 1400 °C are reported in Table 5.2. The data indicate that the adopted processing conditions led to highly porous foams (87-93 vol%) with an almost complete interconnected porosity (the difference between total and open porosity was only ~1%). The porosity of the bodies decreased with increasing agarose concentration in the starting slurry due to lower foaming capacity of Ti_2AlC suspensions containing more agarose. Agarose, having a high molecular weight (~200.000), increases the viscosity of ceramic suspensions thereby reducing the foaming yield [25].

Table 5.2 Total porosity, open porosity, water absorption and density of Ti_2AlC foams.

Agarose content in Ti_2AlC slurry (wt% with respect to the water in the slurry)	Total porosity (vol %)	Open porosity (vol %)	Water absorption (wt%)	Bulk Density ($g \cdot cm^{-3}$)
1.07	93.0 ± 0.3	92.1 ± 0.4	296 ± 15	0.289 ± 0.013
1.42	87.3 ± 0.7	86.9 ± 0.5	175 ± 12	0.522 ± 0.032

The morphology of the sintered foams is shown in Figure 5.3. The obtained foams were typically composed of approximately spherical cells interconnected by circular windows. Spherical pores were associated with polycrystalline struts still containing some pores. The cell and the cell window size decreased with increasing agarose concentration in the starting slurry. This is illustrated in Figures 5.4 and 5.5 by histograms obtained from the results of image analysis. The foams having porosity of 93% prepared with suspensions containing 1.07 wt% of agarose were characterized by a mean cell size of 615 μm and mean window size of 162 μm. On the other hand, the foams having porosity of 87% prepared with slurry containing 1.42 wt% of agarose had a mean cell and cell window size of 335 and 72 μm, respectively.

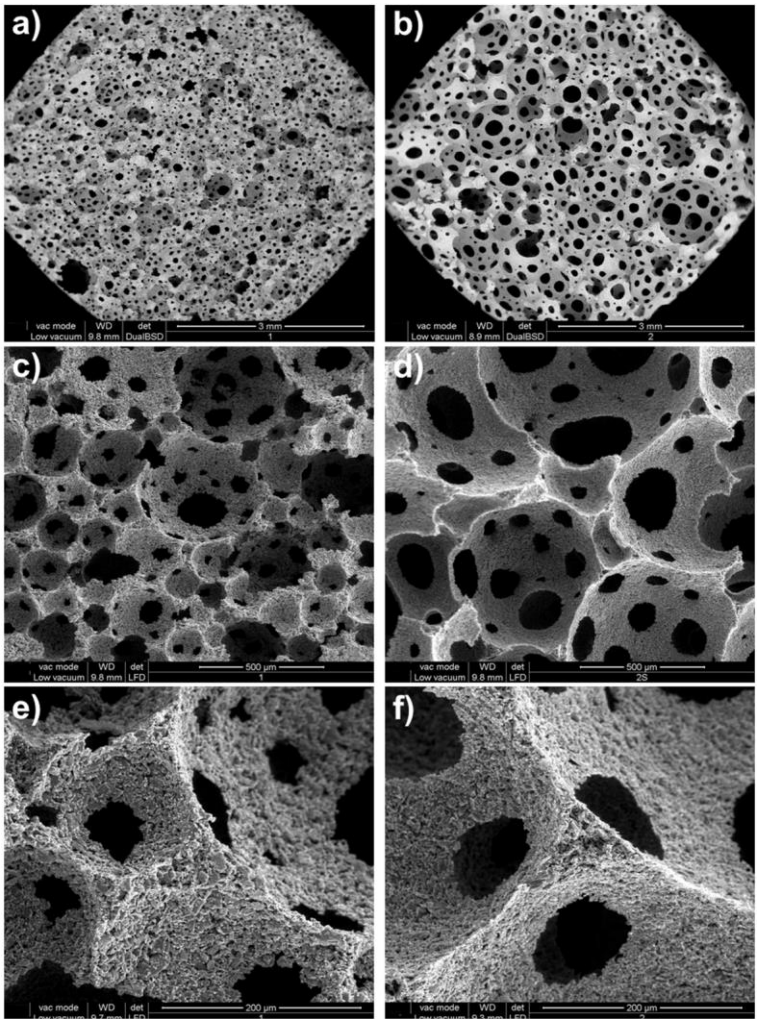

Fig 5.3. Morphology of Ti_2AlC foams: (a) and (b) overall view, (c) and (d) cell and window details, (e) and (f) strut details, ((a), (c), (e): total porosity = 87 vol%, (b), (d) and (f) total porosity = 93 vol%).

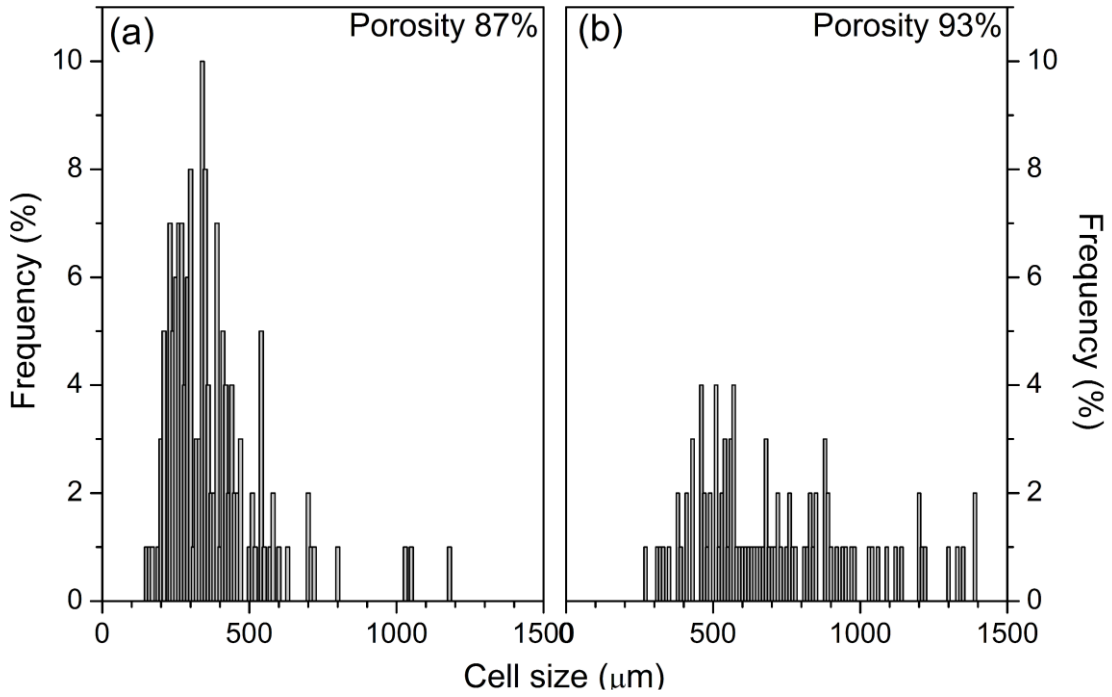

Fig 5.4. Cell size distribution for foams having total porosity: (a) 87 vol% and (b) 93 vol%.

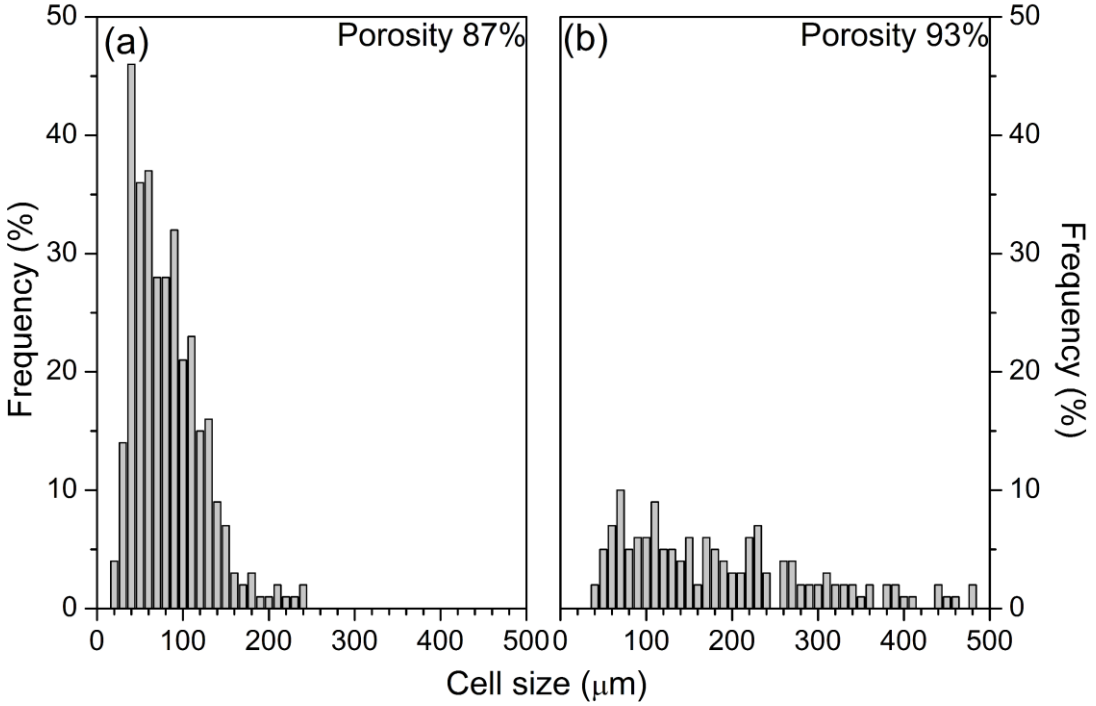

Fig 5.5. Cell window size distribution for foams having total porosity: (a) 87 vol% and (b) 93 vol%.

From Figures 5.4 and 5.5 it can be seen that increasing the agarose concentration in the starting slurry decreased the mean cell size and led to a narrower cell size distribution of the resulted Ti_2AlC foams. This is caused by the higher viscosity of the slurry, and hence higher shear stress generated during mechanical frothing of the suspension containing higher agarose level. According to the Tailor model [38,39], the mechanism of bubble break up into smaller bubbles is connected to the shear stress and the surface tension. If the shear stress overcomes the interfacial stress (surface tension/bubble radius) the bubble will elongate and eventually brake up into smaller bubbles. Hence, the cell size in Ti_2AlC foam made of the suspension containing higher agarose level is smaller.

The main criterion for the applicability of highly porous components possessing open porosity is their permeability and mechanical strength. Figure 5.6 shows a typical pressure drop curve for a Ti_2AlC foam sample with 93 vol% total porosity, from which the permeability constants k_1 and k_2 can be obtained. The parabolic trend of the curve is confirmed by the very good correlation coefficient $R^2 = 0.998$, which validates Forchheimer's equation (5.4), instead of the linear model expressed by Darcy's law. This is typical for gel-cast foams [35,36], and such behaviour was observed for all tested samples. The Darcian and non-Darcian permeability constants of Ti_2AlC foams are given in Table 5.3.

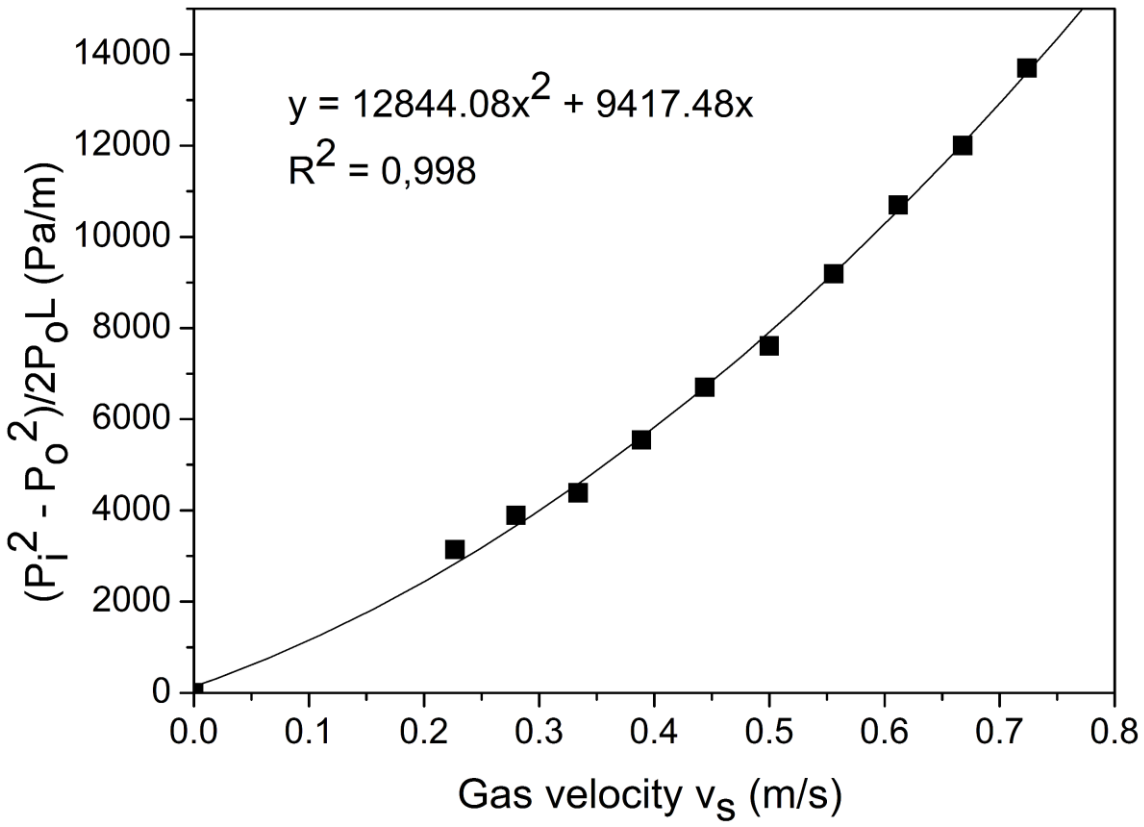

Fig 5.6. Experimental permeability curve for a Ti_2AlC sample having a total porosity of 93%. The solid line represents Forchheimer's equation (5.4).

Table 5.3 Darcian and non-Darcian constants for Ti_2AlC foams.

Total porosity, %	Average cell size (μm)	Average cell window size (μm)	Permeability	
			Darcian constant k_1 ($\cdot 10^{-9}$ m^2)	Non-Darcian constant k_2 ($\cdot 10^{-4}$m)
87	335 ± 19	72 ± 14	2.05 ± 0.16	1.38 ± 0.15
93	615 ± 72	162 ± 18	17.9 ± 1.4	17.5 ± 1.9

The permeability of foams is a result of complex effects of the porosity as well as cell and cell window size. The increase in porosity as well as in cell and cell window size caused an increase in the permeability constants (Table 5.3). The data indicate that these Ti_2AlC cellular structures have a very high permeability, similar to reticulated foams [22], which makes them particularly suitable for instance for solid-fluid separation processes, in which the filtering layer must present

low pressure drop and high particle collection efficiency [35,36]. Moreover, they could also be used to fabricate interpenetrating metal-ceramic composites by infiltration of molten metal [18,40].

Figure 5.7 shows a representative stress-strain plots for the Ti_2AlC foams. These curves indicate that the samples displayed the typical brittle failure of ceramic foams. The maximum stress achieved in the linear elastic region depended on the foam density, and when the stress reached a critical value, the sample started to crack and the stress fell onto the plateau region. A wavy oscillations pattern can be observed in the plateau region for both samples, which can be attributed to the layer by layer fracture of the cell walls. The average compression strength of Ti_2AlC foams having a total porosity of 87 and 93 vol% were 2.79 ± 0.87 and 1.60 ± 0.37 MPa, respectively. Despite the fact that it is not possible to compare these strength data with literature values, as the papers present in the literature discuss MAX phase foams with a much lower amount of total porosity, we can note that the values appear to be at the very high end of those reported for foams of similar relative density fabricated using also different approaches [41]. It is conceivable that by increasing the sintering temperature, in the presence of a Ti_3AlC_2 powder bed, it would be possible to increasing the density of the struts and therefore the strength of the foams, reaching values similar to those reported for Al_2O_3 foams of similar porosity [25].

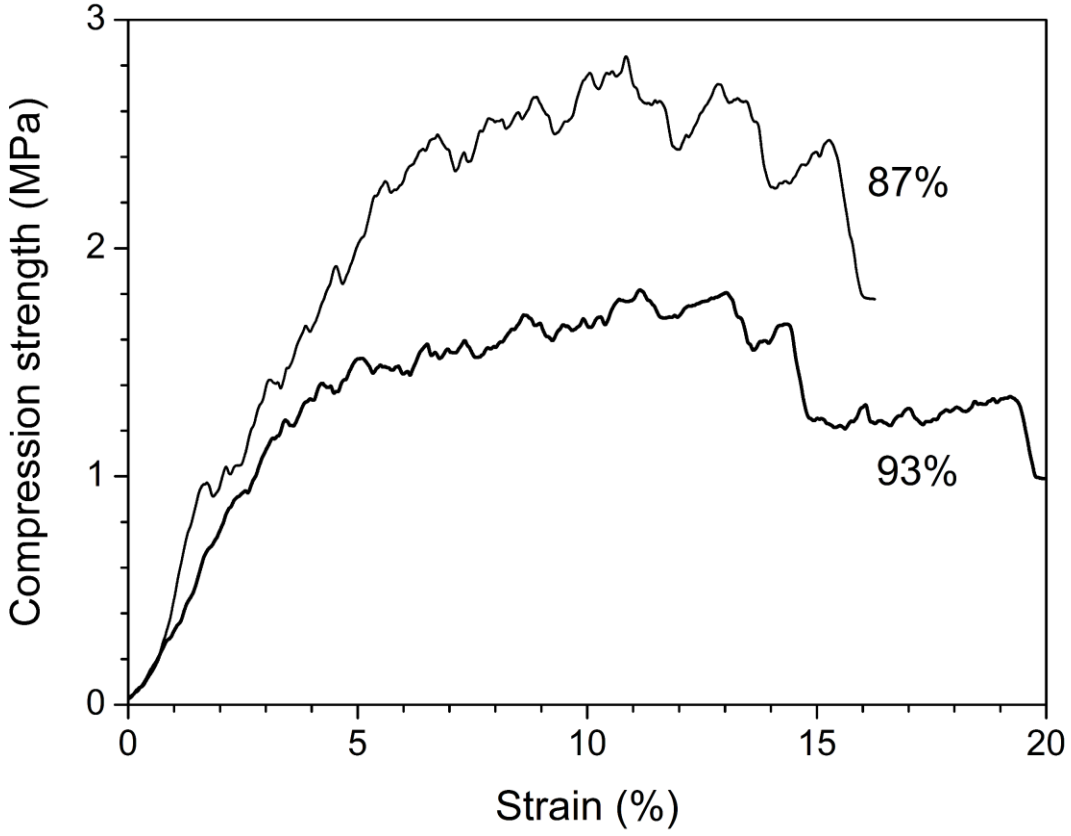

Fig 5.7. Compression stress-strain plots for Ti_2AlC foams having a total porosity of 87 and 93 vol%.

Figure 5.8 shows a SEM image of a fracture surface in a Ti_2AlC foam (total porosity = 87 vol%) after compression test; in the inset is reported a photograph of the sample after testing. The fracture plane is oriented at about 45° with respect to the axis of loading, indicating that the Ti_2AlC foam failed by a shear mechanism along the plane of maximum stress. A close analysis of the fracture path did not allow to observe any signs of delamination in the MAX phase grains, as reported by other researchers [15]. We attribute this discrepancy to the higher amount of microporosity in the struts of our samples, in turn due to the fabrication procedure which did not allow to efficiently compact the ceramic grains in the green body, resulting in a lower degree of bonding between the particles.

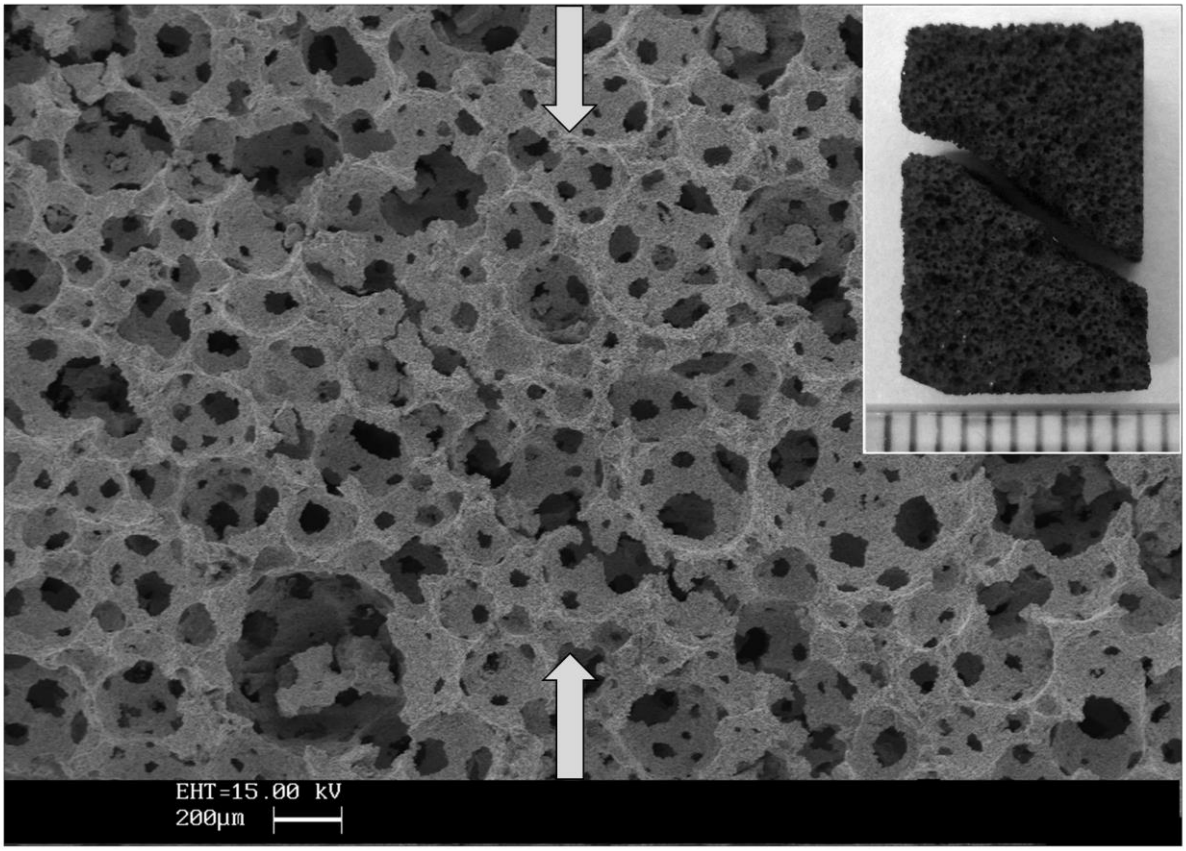

Fig 5.8. SEM image of the fracture surface of a Ti_2AlC foam after compression test: in the inset is shown a photograph of the sample after testing. Arrows indicate the loading direction.

5.4 Conclusions

Highly porous Ti_2AlC open cell foams with a total porosity ranging from 87 to 93 vol% were produced by gel-casting using agarose as a gelling agent. The agarose concentration in the starting slurry affected the amount of porosity as well as the cell and cell window size. Increasing the agarose concentration in the Ti_2AlC slurry, reduced the total porosity and the cell and cell window size, due to an increase in viscosity of the slurry. Foams with a higher amount of total porosity and a larger average cell and cell window size possessed a higher permeability. Depending on the amount porosity and in relation to the mean cell and cell window size, the compressive strength of Ti_2AlC foams ranged from 1.60 to 2.79 MPa. Laying the samples on a Ti_3AlC_2 powder bed during the heat treatment at 1400 °C reduced the thermal decomposition of the Ti_2AlC phase.

References

[1] Barsoum M.W.: MAX phases: Properties of machinable ternary carbides and nitrides, Viley-VCH Verlag GmbH, Weinheim Germany 2013.

[2] Radovic M, Barsoum MW. MAX phases: Bridging the gap between metals and ceramics. *Am Ceram Soc Bull* 2013;**92**(3):20-27.

[3] Sun ZM. Progress and research and development on MAX phases: a family of layered ternary compound. *Int Mater Rev* 2011;**56**(3):143-166.

[4] Sun ZM, Hashimoto H, Zhang ZF, Yang SL, Tada S. Synthesis and characterization of a metallic ceramic material – Ti_3SiC_2. *Mater Trans* 2006;**47**(1):170-174.

[5] Radovic M, Barsoum MW, Ganguly A, Zhen T, Finkel P, Kalidindi SR, Lara-Curzio E. On the elastic properties and mechanical damping of Ti_3SiC_2, Ti_3GeC_2, $Ti_3Si_{0.5}C_2$ and Ti_2AlC in the 300-1573 K temperature range. *Acta Mater* 2006;**54**(10):2757-67.

[6] Sundberg M, Malmqvist G, Magnusson A, El-Raghy T. Alumina forming high temperature silicides and carbides. *Ceram Int* 2004;**30**(7):1899-1904.

[7] Gupta S, Filimonov D, Zaitsev V, Palanisamy T, Barsoum MW. Ambient and 550^{o}C tribological behavior of selected MAX phases against Ni-based superalloys. *Wear* 2008;**264**(3-4):270-278.

[8] Barnes LA, Rago NLD, Leibowitz L. J, Corrosion of ternary carbides by molten lead. *J Nucl Mater* 2008;**373**(1-3):424-428.

[9] Wang XH, Zhou YC. Layered machinable and electrically conductive Ti_2AlC and Ti_3AlC_2 ceramics: A Review. *J Mater Sci Technol* 2010;**26**(5):385-416.

[10] Fraczkiewicz M, Zhou AG, Barsoum MW. Mechanical damping in porous Ti_3SiC_2. *Acta Mater* 2006;**54**(19)5261-70.

[11] Zhou AG, Barsoum MW, Basu S, Kalidindi SR, El-Raghy T. Incipient and regular kink bands in dense and 10 vol% porous Ti_2AlC. *Acta Mater* 2006;**54**(6):1631-39.

[12] Sun ZM, Murugaiah A, Zhen T, Zhou A, Barsoum MW. Microstructure and mechanical properties of porous Ti_3SiC_3. *Acta Mater* 2005;**53**(16):4359-66.

[13] Brodnikovskii NP, Burka MP, Verbilo DG, Demidik AN, Ivanova II, Koval AY, et al. Structure and mechanical properties of porous titanosilicon carbide Ti_3SiC_2. *Powder Metall Met Ceram* 2003;**42**(7-8):424-432.

[14] Firstov SA, Gorban VF, Ivanova II, Pechkovskii EP.: Mechanical properties of porous Ti_3SiC_2/TiC and Ti_4AlN_3/TiN nanolaminates at 20 to 1300ºC. *Powder Metall Met Ceram* 2010;**49**(7-9):414-423.

[15] Hu L, Benitez R, Basu S, Karaman I, Radovic M. Processing and characterization of porous Ti_2AlC with controlled porosity and pore size. *Acta Mater* 2012;**60**(18) 6266-77.

[16] Zhou CI, Ngai TVL, Lu L, Li YY. Fabrication and characterization of pure porous Ti_3SiC_2 with controlled porosity and pore features. *Mater Lett* 2014;**131**:280-283.

[17] Sun Z, Liang Y, Li M, Zhou Y. Preparation of reticulated MAX-phase support with morphology-controllable nanostructured ceria coating for gas exhaust catalyst devices. *J Am Ceram Soc* 2010;**93**(9):2591-97.

[18] Amini S, Ni CY, Barsoum MW. Processing, microstructural characterization and mechanical properties of Ti_2AlC/nanocrystaline Mg-matrix composite. *Compos Sci Technol* 2009;**69**(3-4):414-420.

[19] Amini S, Barsoum MW. On the effect of texture on the mechanical properties of nanocrystalline Mg-matrix composites reinforced with MAX phases. *Mater Sci Eng A* 2010;**527**(16-17):3707-18.

[20] Kontsos A, Loutas T, Kostopoulos V, Hazeli K, Anasori B, Barsoum MW. Nanocrystalline Mg-MAX composites: Mechanical behavior characterization via acoustic emission monitoring. *Acta Mater* 2011;**59**(14):5716-27.

[21] Scheffler M., Colombo P. (Eds.). Cellular ceramics: Structure, Manufacture. Properties and Applications, Wiley-VCH, Weinheim, Germany 2004.

[22] Innocentini MDM, Sepulveda P, Salvini VR, Pandolfelli VC. Permeability and structure of cellular ceramics: A comparison between two preparation techniques. *J Am Ceram Soc* 1998;**81**(12):3349-52.

[23] Brezny R., Green D.J. Fracture behavior of open-cell ceramics. *J Am Ceram Soc*1989; **72**(7):1145-52.

[24] Sepulveda P, Binner JGP. Processing of cellular ceramics by foaming and in situ polymerisation of organic monomers. *J Eur Ceram Soc* 1999;**19**(12):2059- 66.

[25] Potoczek M. Gelcasting of alumina foams using agarose solutions. *Ceram Int* 2008;**34** (3):661-667.

[26] Santacruz I, Moreno R. Preparation of cordierite materials with tailored porosity by gelcasting with polysaccharides. *Int J Appl Ceram Tech* 2008;**5**(1):74-83.

[27] Mouazer R, Thijs I, Mullens S, Luyten J: SiC foams produced by gelcasting: Synthesis and characterization. *Adv Eng Mater* 2004;**6**(5):340-343.

[28] Cosijns A, Vervaet C, Luyten J, Mullens S, Siepmann F, Van Hoorebeke L, Masschaele B, Cnudde V, Remon JP. Porous hydroxyapatite tablets as carriers for low-dosed drugs. *Eur J Pharm Biopharm* 2006;**67**(2):498-506.

[29] Dhara S, Bhargava P. Influence of slurry characteristics on porosity and mechanical properties of alumina foams. *Int J Appl Ceram Technol* 2006;**3**(5):382-392.

[30] Dhara S, Bhargava P. A simple direct casting route to ceramic foams. *J Am Ceram. Soc* 2003;**86**(10):1645-50.

[31] Lemos AF, Ferreira JMF. The valence of egg white for designing smart porous biomaterials: as foaming and consolidation agent. *Key Eng. Mater* 2004;**254-256**: 1045-50.

[32] Lu X, Zhou Y. Pressureless sintering and properties of Ti_3AlC_2. *Int J Appl Ceram Technol* 2010;**7**(6):744-751.

[33] Wang C, Zhou A, Qi L, Huang Y: Quantitative phase analysis in the Ti-Al-C ternary system by X-ray diffraction. *Powder Diffr* 2005;**20**(3):218-223.

[34] Biasetto L, Innocentini MDM, Chacon WS, Corradetti S, Carturan S, Colombo P, Andrighetto A. Gas permeability of lanthanum oxycarbide targets for the SPES project. *J Nucl Mater* 2013 **440**(1-3) 70–80.

[35] Innocentini MDM, Salvini VR, Pandolfelli VC, Coury JR. The permeability of ceramic foams. *Am Ceram Soc Bull* 1999;**9**:78-84.

[36] Moreira EA, Innocentini MDM, Coury JR. Permeability of ceramic foams to compressible and incompressible flow. *J Eur Ceram Soc* 2004;**24**(10-11):3209-18.

[37] Spencer CB, Cordoba JM, Obando N, Sakulich A, Radovic M, Oden M, Hultman L, Barsoum MW. Phase Evaluation in Al_2O_3 fiber-reinforced Ti_2AlC during sintering in the 1300^{o}C – 1500^{o}C temperature range. *J Am Ceram Soc* 2011;**94**(10):3327-34.

[38] Taylor, G. I., The formation of emulsions in definable fields of flow. *Proc. Roy. Soc. Lond Ser A,* 1934;**146**(858):501–523.

[39] Gonzenbach UT, Studart AR, Tervoort E, Gauckler L J. Tailoring the microstructure of particle-stabilized wet foams. *Langmuir* 2007;**23**(3):1025–32.

[40] Binner J, Chang H. Higginson R. Processing of ceramic–metal interpenetrating composites. *J Eur Ceram Soc* 2009;**29**(5):837-842.

[41] Studart AR, Gonzenbach UT, Tervoort E, Gauckler LJ. Processing routes to macroporous ceramics: A Review. *J Am Ceram Soc* 2006;**89**(6):1771–89.

Part III

CONCLUDING REMARKS

III CONCLUDING REMARKS

The research work presented in this thesis regarded the development of highly interconnected Si_3N_4 ceramic foams (open cells) with tailored total porosities in the between of ~74 to 89 vol% and a wide range of cells and windows sizes, which were prepared using different processing routes: emulsion and gelcasting of biopolymers.

Sintering of the Si_3N_4 foams was conducted by different routes: conventional pressureless sintering using N_2 flow at 1600 °C up to 1700°C, generally with prolonged heating time enable the growth of β–Si_3N_4 grains which are in equilibrium with the reactive liquid at sintering temperatures. Additionally, an innovative sintering approach by intense thermal radiation, inside a modified SPS set-up, shows to be effective in promote densification of foams struts decorated with SiC nanowires. Highly porous Si_3N_4 foams with an average cell size of 8~41 μm with total porosity of 80~86 vol% were obtained. The compression strength ranged from 2.0 MPa up to 9.9 MPa.

The combination of Y_2O_3 and MgO as sintering additives, which reacts with the SiO_2 present as oxide layer at Si_3N_4 powder surface enables the formation of β–Si_3N_4 in situ from oxynitride glass. When the sintering temperature reaches 1700°C, almost complete α→β transformation occurred i.e., up to ~98% of β–Si_3N_4. For the conditions investigated here, average aspect ratios of rod-like β–grains ranging from ~4 ± 0.6 up to 11.0 ± 0.5 were obtained with the increased of sintering temperature, which in turns influence the compressive strength that increased from ~13 ± 0.5 up to 28.5 ± 1.4 MPa at total porosities about 74 vol%.

Additionally, gelcasting foams using biopolymers as gelling agents allows microstructures with a strong packing of particles on cell walls and struts, and strength values up to 33MPa at 72% of porosity for methylcellulose gelcasting foams.

Permeability evaluation shows that Si_3N_4 foams are in the range of gelcasting foams (on permeability map) and are suitable for filtering application.

Ti_2AlC foams were successful produced using agar as gel-former. Additionally, the use of powder bed during sintering avoids decomposition of Ti_2AlC phase, which has exceptionally oxidation-resistance.

APPENDICES

A Materials

A.1 Ceramics powders

A.1.1 Si_3N_4

Silicon nitride powder – Si_3N_4 from Yantai Tomley Hi-tech New Materials, Yantai, Shandong, China –purity > 96 wt%, main impurity was trace Fe, oxygen content 7.47 ± 0.08 wt%, average particle size 1.95 μm, BET 9.6 m2/g, containing above 91.5% α–Si_3N_4 phase, see Figure A.1.1.

The special nitridation process of silicon powder to synthesized crystalline Si_3N_4 high quality powders, according to Eq. (A.1) [1], and narrow particle size distribution and characteristics (see Table A.1).

$$3Si + 2N_2 \xrightarrow{1100\text{–}1400^{\circ}C} Si_3N_4 \qquad \text{(A.1)}$$

Table A.1 Si_3N_4 powder particle size and chemical analysis [a]

α– phase	Fe	O_2	N	Al	Ca	Free silicon	d_{50}
> 90%	<100ppm	<1.8%	>38.5%	<100ppm	<40ppm	<0.1%	0.6μm

[a] Chemical analysis from the supplier

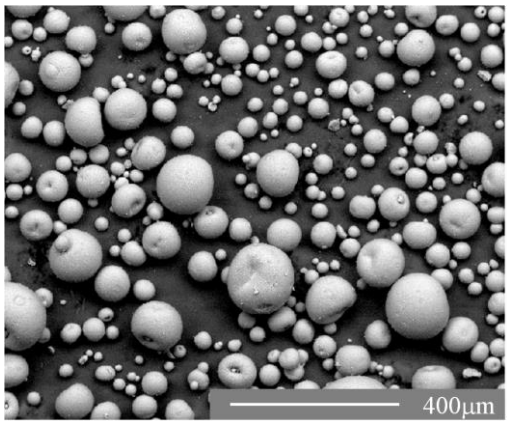

Fig. A.1.1. SEM images of the as received Si_3N_4 powder.

A.1.2 Y_2O_3

Yttrium oxide powder – Y_2O_3 from Inframat Advanced Materials L.L.C., Manchester, New Hampshire, USA – purity ⩾ 99.95 wt%, average particle size d_{50} = 50 nm, see Figure A.1.2.

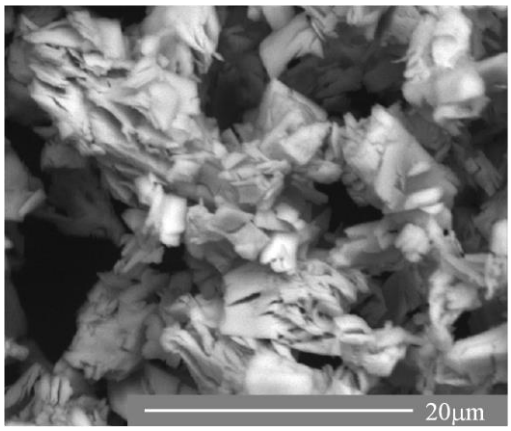

Fig. A.1.2. SEM images of the as received Y_2O_3 powder.

A.1.3 MgO

Magnesium oxide powder – MgO from Bitossi Ceramiche S.R.L., Montelupo Fiorentino, Firenze, Italy – purity ⩾ 99.99 wt%, average particle size d_{50} = 4.6 μm. The MgO was obtained by the calcination of $MgCO_3$ at 650 ºC for 1 hour, see Figure A.1.3.

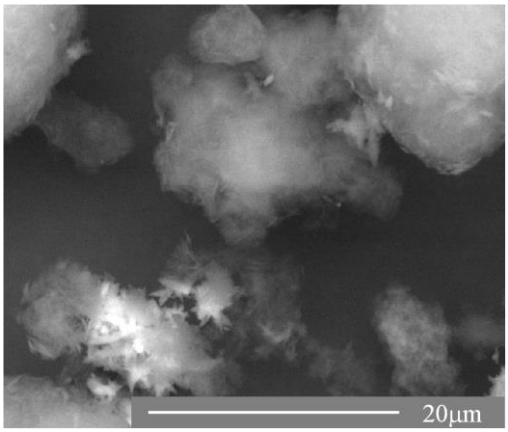

Fig. A.1.3. SEM images of the calcinated MgO powder.

A.1.4 Ti_2AlC

Titanium aluminium carbide powder – Ti_2AlC from Sandvik Heating Technology, Hallstahammar, Sweden – purity ⩾ , average particle size d_{50} = 5.4 μm. Maxthal 211 (Ti_2AlC) ceramic engineering material (Figure A.1.4) is an alumina–forming MAX–phase, which makes it highly suitable for use in air and oxidizing atmospheres up to 1450 ºC.

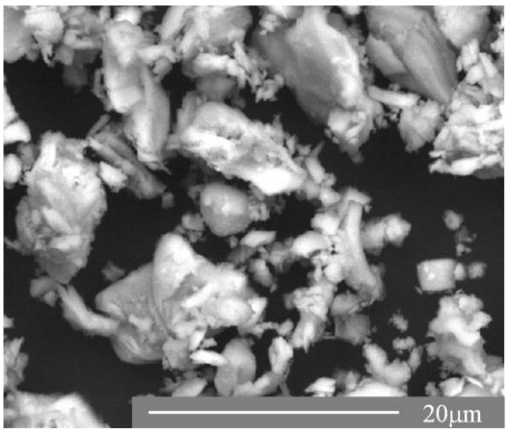

Fig. A.1.4. SEM images of the as received Ti_2AlC powder.

A.2 Surfactants and biopolymers

A.2.1 Poly(acrylic acid) – PAA

(CAS n. 9003-01-4) average molecular weight M_w = ~1,800, density ρ= 1.2 g·cm^{-3} at 25 ºC (Sigma-Aldrich, Italy). See chemical structure from supplier, see Figure A.2.1.

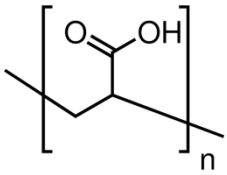

Fig. A.2.1. General simplified formula of poly(acrylic acid).

A.2.2 Poly(ethyleneimine) – PEI

(CAS n. 9002-98-6) average molecular weight M_w = ~750,000, solution 50 wt % in H_2O, density ρ= 1.03 g·mL^{-1} at 25 ºC (Sigma-Aldrich, Italy). See chemical structure from supplier, see Figure A.2.2.

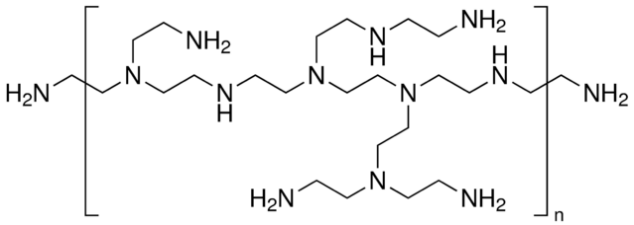

Fig. A.2.2. General simplified formula of poly(ethyleneimine).

A.2.3 Tween® 80

Polyoxyethylenesorbitan monooleate – Polysorbate 80 (CAS n. 9005-65-6) average molecular weight M_w = ~1,320 , HLB value 15, density ρ= 1.076 g· mL $^{-1}$ at 25 ºC (VWR International Ltd – BHD Prolabo, UK). See chemical structure from supplier, see Figure A.2.3.

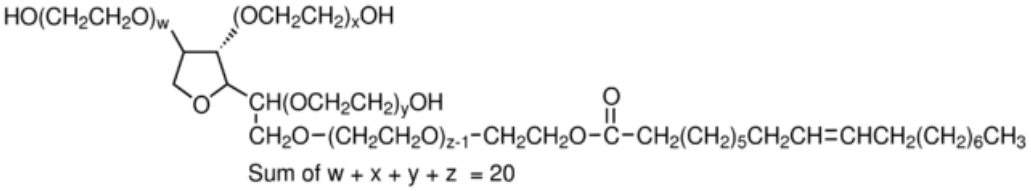

Fig. A.2.3. General simplified formula of polysorbate 80.

A.2.4 Tergitol® TMN 10

Polyethylene glycol trimethylnonyl ether – Tergitol® TMN 10 (CAS n. 60828-78-6) average molecular weight M_w = ~683, HLB value ~14.1, density ρ= 1.04 g·mL^{-1} at 20 ºC (Sigma-Aldrich, Italy). See chemical structure from supplier, see Figure A.2.4.

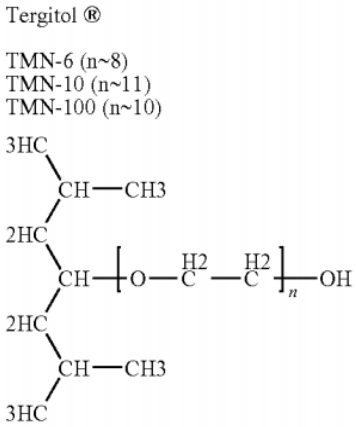

Fig. A.2.4. General simplified formula of Tergitol® TMN 10.

A.2.5 Albumen

Egg white albumen – Ovalbumin (90.5%) (CAS n. 9006-59-1) average molecular weight M_w = ~45,000, density ρ= 1.035 g·cm^{-3} at 20 ºC (AppliChem Gmbh, Darmstadt, Germany)

A.2.6 Agar-agar

Agar (*gelidium sp*.) – Food grade; (ERBAMEA Srl, Perugia, Italy)

A.2.7 Methylcellulose

Methylcellulose ether – METHOCEL^{TM} A4M (CAS n. 9004-67-5) Food grade; average molecular weight M_n = ~88,000, density ρ= 0.7 g·cm^{-3} at 20 ^{o}C (Dow Europe GmbH, Horgen, Switzerland).

B Materials characterization

B.1 X– Ray diffraction

All XRD analysis were made using Bruker AXS D8 Advance diffractometer (Bruker, Karlsruhe, Germany), using a CuKα radiation (1.5418 Å), θ - 2θ configuration 40 kV, 40 mA, 2 s with a 0.05° step size. Phase identification was performed using Match! Software package (Crystal Impact GbR, Bonn, Germany) supported by ICDD PDF-2 Powder Diffraction File (International Center for Diffraction Data, Newtown Square, PA, USA) as the reference database.

To understand the evolution of the crystalline phases during sintering, the relative amounts (weight fraction) of the major phases present, α– and β–Si_3N_4, were calculated using techniques based on the Ref. [2]. In order to minimizing error due to preferred orientation and particle statistics, computed-integrated intensities were used to calculate normalizing factors, L , see Table B.1. Additionally, L was used to correct the experimental peak intensities, Y required for the subsequent calculations. For example, the corrected intensity for the β–Si_3N_4 (210) peak was found to be: $I_{\beta-(210)_c} = 11.21 \cdot Y$

The correct values for peak intensity were used to determine the weight percent of α– and β–Si_3N_4 from the ratio:

$$\frac{I_{\beta(210)_c}}{\left(I_{\beta(210)_c} + I_{\alpha(210)_c} \right)} \tag{B.1}$$

Table B.1 Selected peaks and L values used for quantitative analysis

Phase	*2θ*	*Reflection*	*L*
α–Si_3N_4	35.3	(210)	6.79
β–Si_3N_4	36.1	(210)	11.21

B.2 Density and porosity measurements

Density measurements on bulk samples were performed according to the standard (ASTM–C 373). After the determination of the dry mass D, the saturated mass M and the mass while

suspended in water *S*, all density and porosity values were calculated using the formulas reported in Table B.2.

Table B.2 Calculations description for determination of physical properties of sintered components (ASTM–C 373)[a]

Bulk density	$B = D/M - S$
Open pores volume	$V_{OP} = M - D$
Apparent porosity	$P = [(M - D)/(M - S)] \cdot 100$
Apparent specific gravity	$T = D/(D - S)$

[a] In the calculations, water is considered as the buoyant medium (1 cm^3 of water weights 1g).

The density of ceramic powders was measured by gas pycnometer (AccuPyc 1330, Micromeritics, Norcross, GA) (ASTM B923).

Mercury porosimetry consists of the gradual intrusion of mercury into an evacuated porous medium by capillary rise phenomenon whereby an excess pressure is required to cause a non-wetting liquid to enter a narrow capillary, average diameters of open cells and the apparent porosity of the porous ceramics were measured by this technique (Pascal 140/440 Porosimeter 2000, Germany). Cell size information in terms of an equivalent cylindrical capillar size may be extracted from capillary pressure data using the Young–Laplace equation:

$$r = \frac{2\sigma_{Hg-Air} \cos\theta_{Hg-Air}}{Pc_{Hg-Air}} \quad \text{(B.2)}$$

where r is the pore radius, σ is the surface tension of the mercury–air interface, and θ is the contact angle of mercury on the solid surface of the pore wall. In general, difficulties from pore accessibility limitations can conduct to wrong results because in some cases just smaller pores are intruded by mercury [3].

B.3 SEM - Scanning Electron Microscopy

The microstructure of the foams was characterized using FEI Quanta 200 FEG, Quanta 200 (FEI Company, The Netherlands) microscope. A field emission scanning electron microscope (FE-

SEM, JSM-7000F, JEOL, Tokyo, Japan) was also used. The average cell size and cell windows sizes were measured by the linear intercept method according to ASTM E112-12 (diagonal opposite directions), using an image analysis program (Axio Vision LE). For spherical cells uniformly distributed, according to ASTM D3576-98, the relationship between the average measured chord length t and the average sphere diameter *D* is: $D = t \cdot 1.623$.

B.4 TEM - Transmission Electron Microscopy

A Schottky-type field emission transmission electron microscope (TEM, JEM-2100F, JEOL, Tokyo, Japan) operated at 200 kV, equipped with an energy-dispersive X-ray spectroscopy (EDX mapping in HAADF-STEM mode, for ~30 min) detector. A transmission electron microscope (TEM, JEM-2100, JEOL Ltd, Tokyo, Japan) operated at 200 kV, was used to collect electron diffraction (ED) data were collected with a LaB6 filament. For TEM study, the sample was crushed into powder during ~20 min and ultrasonic dispersed in ethanol for ~10 min. Then it was transferred on a Cu grid coated with carbon film. The average cells and windows sizes; and the aspect ratio of the rod-like β–Si_3N_4 grains were measured by the linear intercept method according to ASTM E112-12, using an image analysis program (Axio Vision LE).

B.5 Mechanical characterization

Compressive strength measurements were performed using a universal testing machine Instron 1121 UTM (Instron, Danvers, MA) with a cross-head speed of 1 mm/min, and the compressive load cell was 5 kN, according to the standard (ASTM C133-94). Before testing, samples were cut down to an approximate cubic shape with length of the edges of ~10mm. Compressive strength σ could be calculated with the relation $\sigma = P \cdot A^{-1}$, where P is the load applied and A the surface area where the load is applied.

B.6 Permeability

The experimental evaluation of permeability parameters was carried out with air/argon flow in temperatures ranging from ~ 25 to ~ 650°C in a laboratory-made hot gas permeameter (see Figure B.1, room temperature device labeled as (R.T), on the left and, high temperature device labeled as (H.T), on the right). The air/gas was forced to flow in stationary regime through the flat disk sample laterally sealed (with Teflon tape or thermal paste depending on the temperature of permeability test), to allow the air/gas flow to occur only in the top-bottom direction. Subsequently, the disk is placed in a sample holder with the flatter surface facing down (to the flow inlet). The

sample holder can be placed inside an electric furnace (7500 W) in order to perform high temperature permeability test. Pressures P_i and P_o were measured by a digital micromanometer and recorded as a function of the resulting air/gas volumetric flow rate (Q), measured with a rotameter and converted to the superficial velocity (v_s). K-type thermocouples were used to monitor the temperatures of the air entering (T_i) and exiting (T_o) the sample. They were also used to monitor the gas temperature near the pressure transducers and prior to entering in the flowmeter devices.

The collected data sets (P_i, P_o and vs) for each temperature level were treated using Microsoft Excel 2010® according to the least-square method using a parabolic model of the type: $y = ax + bx^2$, in which y was $\Delta P/L$ and x was the air/gas velocity *vs*. The permeability parameters of Forchheimer's equation (2.1) were then calculated from the fitted constants a and b respectively by $k_1 = \mu/a$ and $k_2 = \rho/b$.

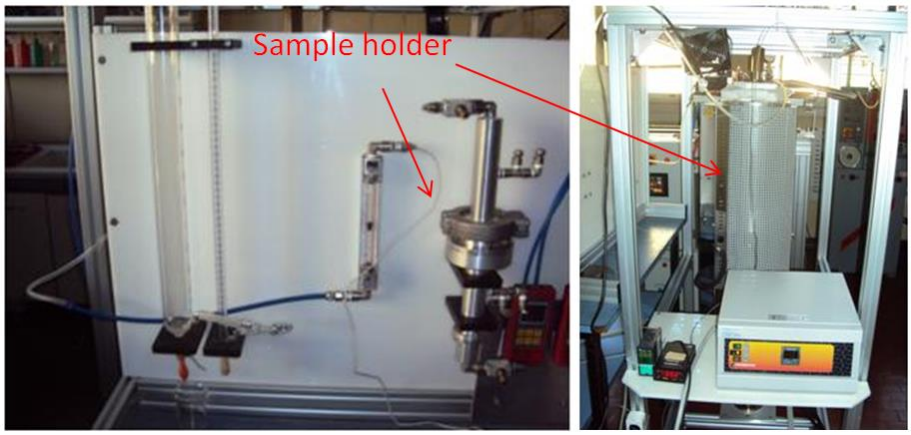

Figure B.1. Illustration of the laboratory-made gas permeameter used for the tests: room temperature (R.T.), on the left; and of the high temperature (H.T.), on the right.

References

[1] Lange H, Wötting G, Winter G. Silicon nitride-from powder synthesis to ceramic materials. *Angew Chem Int Engl* 1991;**30**(12):1579–97.

[2] Blanchard CR, Schwab ST. X-ray diffraction analysis of the pyrolytic conversion of perhydropolysilazane into silicon nitride. *J Am Ceram Soc* 1994;**77**(7):1729–39.

[3] Handbook ASM. Volume 7. Powder Metal Technologies and Applications; 1998. p.435.

C List of publications

- GUZI DE MORAES E, COLOMBO P (2014). Silicon nitride foams from emulsions. MATERIALS LETTERS, ISSN: 0167-577X, doi: 10.1016/j.matlet.2014.04.102.
- LI D, GUZI DE MORAES E, GUO P, ZOU J, ZHANG J, COLOMBO P, SHEN Z (2014). Rapid sintering of silicon nitride foams decorated with one-dimensional nanostructures by intense thermal radiation. SCIENCE AND TECHNOLOGY OF ADVANCED MATERIALS, ISSN: 1468-6996, doi: 10.1088/1468-6996/15/4/045003.
- LI D, GUO P, GUZI DE MORAES E, WAN W, ZOU J, COLOMBO P, SHEN Z (in stampa). Structural study of disordered SiC nanowires by three-dimensional rotation electron diffraction. MATERIALS RESEARCH EXPRESS, ISSN: 2053-1591.
- GUZI DE MORAES E, LI D, COLOMBO P, SHEN Z (2014). Silicon nitride foams from emulsions sintered by rapid intense thermal radiation. JOURNAL OF THE EUROPEAN CERAMIC SOCIETY, ISSN: 0955-2219. (*submitted*)
- LI D, GUZI DE MORAES E, COLOMBO P, SHEN Z (2014). Preparation of nasal cavity-like SiC-Si_3N_4 foams with hierarchical pore architecture. RSC ADVANCES, ISSN: 2046-2069. (*submitted*)
- POTOCZEK M, GUZI DE MORAES E, COLOMBO P (2014). Ti_2AlC foams produced by gel-casting. JOURNAL OF THE EUROPEAN CERAMIC SOCIETY, ISSN: 0955-2219. (*submitted*)

Presentations at Conferences

- Oral presentation on 6th International Workshop on Spinel Nitrides and Related Materials, "Si_3N_4 foams from emulsions". Rüedesheim, Germany (2012).
- Poster presentation on ICACC'13 – 37th International Conference and Expo on Advanced Ceramics and Composites, "Si_3N_4 foams from emulsions". Daytona Beach, USA (2013).
- Poster presentation on Pacrim10 – The 10th Pacific Rim Conference on Ceramic and Glass Technology, "MAX phases foams by direct foaming". San Diego, USA (2013).
- Oral presentations on ECERS – 13th International Conference of the European Ceramic Society, "Si_3N_4 foams from emulsions: processing and microstructure" and "Si_3N_4 foams sintered by Pressureless spark plasma sintering". Limoges, France (2013).

- Poster presentation on Euromat2013 – European Congress and Exhibition on Advanced Materials and Process, "Si_3N_4 foams from emulsions". Sevilla, Spain (2013).
- Poster presentation on ICACC'14 – 38th International Conference and Expo on Advanced Ceramics and Composites, "ZrB_2-SiC-Si foams by direct foaming". Daytona Beach, USA (2014).
- Oral presentation on ICACC'14 – 38th International Conference and Expo on Advanced Ceramics and Composites, "Si_3N_4 Foams Sintered by Pressureless Spark Plasma Sintering". ". Daytona Beach, USA (2014).
- Oral presentation on ISNT 2014 8th International Symposium on Nitrides in conjunction with the 7th International Workshop on Spinel Nitrides and Related Materials, "Si_3N_4 Foams From Direct Foaming Methods". Wildbad Kreuth, Germany (2014).